INTERNATIONAL SYMPOSIUM ON PLASTIC DEFORMATION AND TEXTURE ANALYSIS

ALCOY (ALICANTE) - 2012

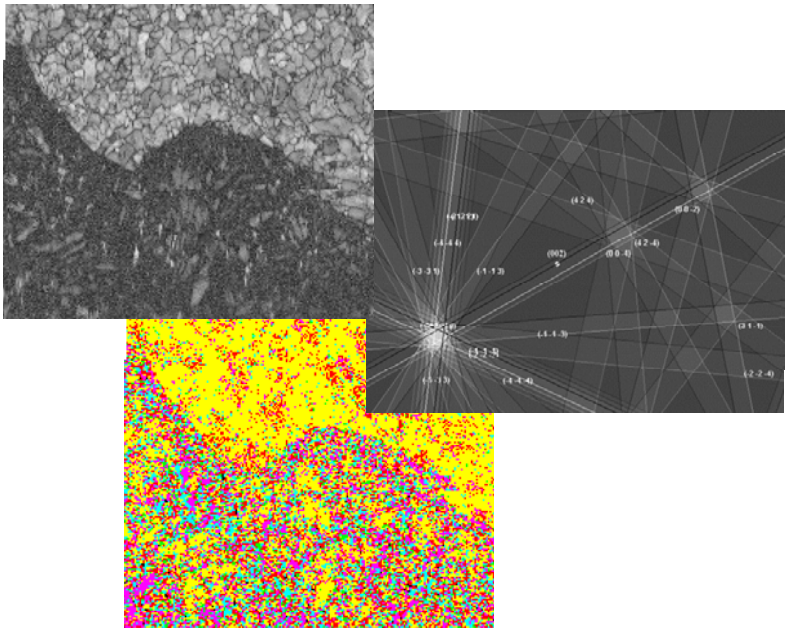

Editor:
Vicente Amigó Borrás

EDITORIAL

UNIVERSITAT POLITÈCNICA DE VALÈNCIA

UNIVERSITAT POLITÈCNICA DE VALÈNCIA

INTERNATIONAL SYMPOSIUM ON PLASTIC DEFORMATION AND TEXTURE ANALYSIS

ALCOY (ALICANTE) - 2012

Editor:
Vicente Amigó Borrás

EDITORIAL UNIVERSITAT POLITÈCNICA DE VALÈNCIA

Firts edition, 2012.

Editor:
Vicente Amigó Borrás

Duplica: Flashbay

ISBN: 978-84-8363-997-9
Referencia Editorial: 6093

Editor's Foreword

The symposium is an international prestigious researchers meeting focused on plastic deformation of materials and microstructural characterization, especially through the microtexture analysis. Therefore, the first day is devoted to plastic deformation (hot and cold) and creep analysis of materials. The second aims to give researchers an overview of EBSD techniques (Electro Back Scattered Diffraction), new advances and applications in the technique are presented, as well as new developments in Diffraction, thus allowing to extend the microstructural analysis to TEM (Transmission Electron Microscopy).

This book includes communications made in the symposium, which we divided into two parts. The first communication including dedicated to plastic deformation of materials, metallic and ceramic. The second, which includes the works devoted to the analysis of textures.

This second part is mainly intended to recent research in Electron Diffraction Backscattered (EBSD) and some of its applications. Finally other developments in the field of diffraction are discussed.

We hope that this document will be of interest and will show the latest developments and applications in texture analysis.

Valencia, September 2012
The editor

Prólogo del editor

El simposio es una reunión de investigadores de prestigio internacional en la deformación plástica de los materiales y los cambios microestructurales, especialmente a través del análisis de microtextura. Por lo tanto, el primer día se dedica a la deformación plástica (caliente y frío) y fluencia de los materiales. El segundo objetivo es dar a los investigadores una visión general de las técnicas de EBSD (Difracción de electrones retrodispersados), los nuevos avances en la técnica y las nuevas aplicaciones, así como los nuevos desarrollos en difracción, lo que permite extender el análisis microestructural a la Microscopía Electrónica de Transmisión.

Este libro recoge las comunicaciones realizadas en el simposio, que hemos dividido en dos partes. La primera que incluye las comunicaciones dedicadas a la deformación plástica de los materiales, metálicos y cerámicos. La segunda, donde se incluyen los trabajos dedicados al análisis de las texturas.

Esta segunda parte se destina principalmente a las recientes investigaciones en Electron Backscatered Diffraction (EBSD) y algunas de sus aplicaciones. Finalmente se analiza otros desarrollos en el campo de la difracción.

Esperamos que este documento resulte de interés y pueda mostrar los últimos avances y aplicaciones en el análisis de texturas.

Valencia, Septiembre 2012
El editor

Organizing Committee

Vicente Amigó Borrás, ITM - Universitat Politècnica de València
Manuel Carsí Cebrián, CENIM - CSIC
Fernando Carreño Gorostiaga, CENIM – CSIC
Patricia Franconetti Rodríguez, ITM - Universitat Politècnica de València

Scientific Committee

Vicente Amigó Borrás, ITM - Universitat Politècnica de València
Oscar Ruano Mariño, CENIM - CSIC
Manuel Carsí Cebrián, CENIM - CSIC
Isabel Gutiérrez Sanz, CEIT, San Sebastián
Carlos Capdevila Montes, CENIM - CSIC
Fernando Carreño Gorostiaga, CENIM - CSIC
Teresa Pérez Prado, IMDEA, Madrid
Paloma Adeva Ramos, CENIM - CSIC

Sponsors

UNIVERSITAT POLITÈCNICA DE VALÈNCIA

ITM
Instituto de Tecnología de los Materiales

GOBIERNO DE ESPAÑA
MINISTERIO DE ECONOMÍA Y COMPETITIVIDAD

NanoMEGAS
Advanced Tools for electron diffraction

Index

Session 3: Plastic deformation and Creep III

Session 5: EBSD Applications I

Session 6: EBSD Applications II

International Symposium on Plastic Deformation and Texture Analysis
Alcoy (Spain) 24-25 September 2012
13-24

Texture and Texture Evolution during Superplastic Deformation of Aluminum Alloys

Sarath K Menon[1,2], Terry R McNelley[1,3]

[1]Department of Mechanical and Aerospace Engineering, Naval Postgraduate School, 700 Dyer Road, Monterey, CA 93943 - USA

Abstract

The constitutive behaviour of superplastic materials may be described in terms of additive contributions from grain boundary sliding and slip creep mechanisms. Grain size refinement enhances superplastic response. Deformation and recrystallization treatments of wrought aluminium alloys are required for this purpose. Collaborative studies on deformation processing and superplasticity in aluminium alloys by the authors and investigators at the CENIM Laboratory, Madrid, are reviewed. Examples of texture and microstructure evolution for discontinuous and continuous recrystallization reactions are presented and the role of alloy constitution for each is described.

Resumen

El comportamiento constitutivo de materiales superplásticas puede ser descrito en términos de las contribuciones aditivas de deslizamiento del límite de grano y deslizar los mecanismos de fluencia. Refinamiento del tamaño de grano mejora la respuesta superplástica. Tratamientos de deformación y recristalización de las aleaciones de aluminio forjado se requieren para este propósito. Los estudios en colaboración sobre el procesamiento de la deformación y superplasticidad en aleaciones de aluminio por parte de los autores e investigadores en el Laboratorio CENIM, Madrid, son revisados. Ejemplos de textura y evolución de la microestructura de las reacciones de recristalización discontinuas y continuas son presentados y el papel de la constitución de cada aleación se describe.

Keywords: Superplasticity, grain boundary sliding, slip creep, discontinuous recrystallization, continuous recrystallization

Palabras clave: Superplasticidad, deslizamiento del límite de grano, se deslizan recristalización lenta y discontinua, recristalización continua

1. Introduction

1.1. Grain size and superplasticity

The elevated temperature mechanical behavior of fine-grained superplastic materials can be described by a constitutive equation for the deformation rate, $\dot{\varepsilon}_{total}$, based on the independent, additive contributions of grain boundary sliding (GBS) and slip creep [1-4]. That is, $\dot{\varepsilon}_{total} = \dot{\varepsilon}_{gbs} + \dot{\varepsilon}_{\perp}$, where $\dot{\varepsilon}_{gbs}$ and $\dot{\varepsilon}_{\perp}$ are the contributions from GBS and slip creep, respectively. GBS takes place on the boundary plane and its accommodation occurs in a mantle-like region nearby the grain boundary so that $\dot{\varepsilon}_{gbs}$ is strongly dependent on grain size. In contrast, slip creep takes place within the core regions of the grains, and so $\dot{\varepsilon}_{\perp}$ is grain size independent. Combining empirical relationships for $\dot{\varepsilon}_{gbs}$ and $\dot{\varepsilon}_{\perp}$ results in the following constitutive equation [3,4]

$$\dot{\varepsilon}_{total} = AD^{*}_{eff}\left(\frac{1}{d}\right)^{2}\left(\frac{\sigma}{E}\right)^{2} + KD\left(\frac{\sigma}{E}\right)^{n} \qquad (1)$$

where A is a material constant for grain boundary sliding, D^{*}_{eff} is a modified effective diffusion coefficient, d is the grain size σ is the applied stress, E is Young's modulus, and D and n are the appropriate diffusion coefficient and stress exponent (3 – 5) for the slip creep mechanism. Equation 1 predicts a grain-size dependent transition from slip creep at high stresses and low temperatures to grain boundary sliding at lower values of stress and higher temperatures. This is illustrated in Fig. 1 for a hypothetical material having $D^{*}_{eff} = D$ (the lattice diffusion coefficient) and $n = 5$ (i.e., slip creep controlled by dislocation climb). Furthermore, grain size refinement leads to the transition to superplastic deformation by grain boundary sliding at higher rates and lower temperatures. The transition is reflected in the change in apparent

stress exponent, n $(\equiv d\log\sigma / d\log\dot{\varepsilon})$ from $n=5$ to $n=2$. Thus, the strain rate sensitivity coefficient m $(\equiv 1/n)$ increases from 0.2 to 0.5, and this latter value is generally recognized as sufficient to support resistance to necking and large, superplastic elongations [1,3]. Clearly, grain size refinement increases the strain rate range for superplasticity and grain size $d \leq 10\mu m$ is generally deemed necessary for useful superplasticity [4].

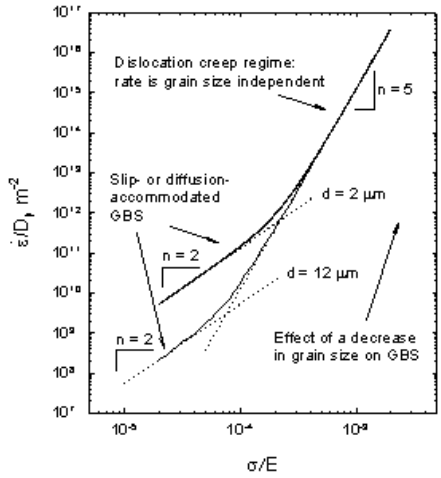

Figure 1. Diffusion compensated rate vs. modulus compensated stress showing the effect of grain refinement on GBS.

Grain refinement for superplasticity in wrought aluminum alloys can only be achieved by deformation and recrystallization treatments. From the kinetic theory of nucleation during phase transformations [5], the strain energy due to dislocations stored during deformation is insufficient to support the formation of recrystallization nuclei by the atom-by-atom growth of embryos. Instead, new grains form from pre-existing nuclei in the form of small cells or subgrains distributed in the deformation microstructure. This can account for the observation that the lattice orientations of new grains in the recrystallized microstructure often have evolved from orientations present in the prior deformation microstructure. The role of alloy constitution is not fully understood. However, fine cells or subgrains developed in the vicinity of non-deforming particles that are on the order of 1.0µm in size may become stable nuclei. This particle-stimulated nucleation results in a grain size that reflects the particle spacing and grain orientations tend to be random due to steep orientation gradients in the vicinity of the constituent particles [6]. In contrast,

very fine particles (on the order of 10nm in size) may retard migration of highly misoriented cell walls and subgrain boundaries. In a continuous process, new boundaries form by dislocation reaction and the new grains may have lattice orientations corresponding directly to those in the deformation microstructure.

1.2. Grain boundaries and superplasticity

For superplasticity, grain boundaries must be able to slide while resisting tensile separation [e.g., 1-4]. Nevertheless, the specific requirements that the grain boundaries must meet are less well understood than the role of grain size. Lattice registry across subgrain boundaries (i.e., boundaries consisting of dislocation arrays) would preclude GBS, so that refined subgrains are not sufficient and high-angle grain boundaries are considered to be necessary for superplasticity. In this context, the angle involved is the minimum among all crystallographically equivalent rotations that will bring the lattice on opposite sides of the boundary into coincidence. A complete description of a grain boundary should include the orientation of the boundary plane as well as the lattice misorientation angle. Few investigations have considered such details of the grain boundaries in GBS and the most recent results appear to be those of Weinberg [7] more than 50 years ago (Fig. 2) for grain boundary pairs in aluminum tri-crystals.

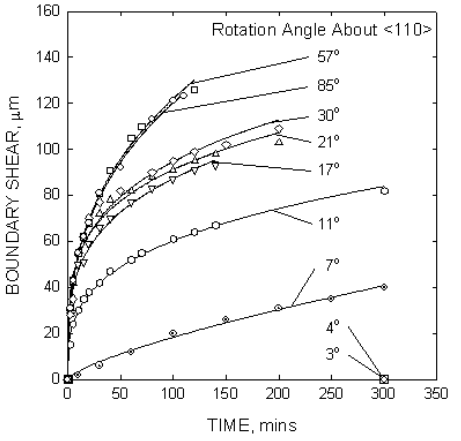

Figure 2. Boundary shear vs. time for Al tri-crystals deformed at 600° [7].

Recent developments in electron backscatter diffraction (EBSD) and orientation imaging (OIM) [8,9] have enabled the acquisition of ample grain-specific orientation data in microstructure analysis. Conventional pole figures and orientation distribution functions may be obtained from such data. Furthermore, grain-to-grain misorientation distributions may also be calculated and such distributions are often represented in histogram form showing the population of boundaries in various misorientation ranges. EBSD is limited to a resolution of about 1° in misorientation for modern scanning electron microscopes.

In the following sections, collaborative research by the authors and investigators at the CENIM Laboratory in Madrid will be described [10-15]. Microstructure and microtexture data for superplastic AA5083 will be used as an example of materials that develop superplastic microstructures by particle-stimulated nucleation of recrystallization. Corresponding data for AA2004 will show that superplastic response may also occur when refined grains form by a continuous reaction.

2. Experimental Methods

2.1. Materials

Al-Mg alloy AA5083 is nominally Al-4.5Mg-0.7Mn (compositions in wt. pct.) and SKY5083 is a low Fe + Si version of this material. The former material has been the subject of a series of reports [e.g.,16,17] while the latter was examined in the earlier work [13]. Ingots of these materials are normally processed for superplasticity by approximately 75% cold reduction of hot band material to produce sheet material normally 1.0 – 2.0mm in thickness. The AA2004 alloy is nominally Al-6Cu-0.4Zr. High cooling rates during casting are necessary to retain Zr in solution during solidification, and a combination of hot working and cold cross rolling is employed to produce sheet material of thickness up to 3.0mm.

2.2. Mechanical testing and microstructure analysis

Elevated temperature mechanical testing was conducted on tensile samples having gage sections 12.7mm in length, 5.0mm in width and of sheet thickness. Testing temperature was maintained constant by use of a five-zone resistance furnace and crosshead speeds were maintained constant to failure.

Conventional mechanical and electropolishing methods were used in sample preparation for microstructure and OIM analysis. The OIM typically involved use of a scanning microscope (TopCon S540) equipped with a LaB_6 filament. Conventional data cleanup procedures were employed in preparation of grain maps and discrete pole figures.

3. Results and discussion

3.1. The as-rolled materials

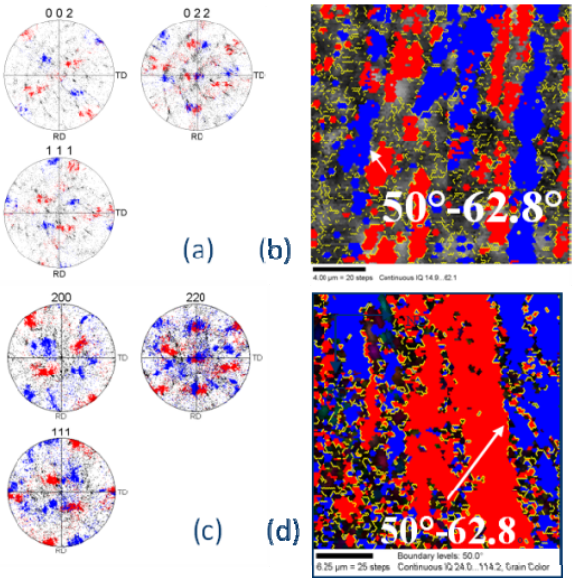

Figure 3. Discrete pole figures (a) and grain map (b) for as-rolled AA2004; pole figures (c) and grain map (d) for AA5083.

Deformation processing of aluminum sheet material for superplastic forming generally concludes with cold rolling, and the deformation-induced microstructures of selected examples have been catalogued in a series of reports [10-17]. Representative microtexture and microstructure data for as-rolled AA2004 and AA5083 materials are included in Fig. 3. Examination of the discrete pole figures reveals that both materials develop a distinct brass-, or B-type texture component ({011}<112>, where the notation refers to {plane parallel to the rolling plane}<direction parallel to the rolling direction>). OIM data include the location of each lattice orientation measurement. Thus, the

spatial distribution of the crystallographically distinct orientation variants of the B texture component, B_1, $(110)[1\bar{1}2]$, and B_2, $(011)[2\bar{1}1]$, may be separately distinguished in both the pole figures and grain maps prepared from the orientation data. Highlighting of all orientations that lie within 15° of either orientation variant reveals that the spatial distribution of these variants involves elongated, band-like regions about 2.5µm in thickness in the normal direction of the rolled sheet for the AA2004 and 4 – 8µm in thickness for the AA5083. The lattice misorientation of the B_1 and B_2 variants is 60°.

3.2. Recrystallization and superplastic response

Superplastic forming may be accomplished by heating and equilibrating of aluminum sheet material at the forming temperature, typically 0.7 – 0.8T_M, where T_M is the melting temperature, before application of differential gas pressure. Heating of the AA5083 material at 450°C resulted in the rapid transformation of the cold-rolled microstructure and formation of equiaxed grains 7 – 8µm in size, as shown in the grain map of Fig. 4a. Only the grain boundaries are highlighted in this map. The B-type cold rolling texture component has been replaced by a nearly random texture (Fig. 4b), accompanied by a near random grain-to-grain misorientation distribution (Fig. 4c).

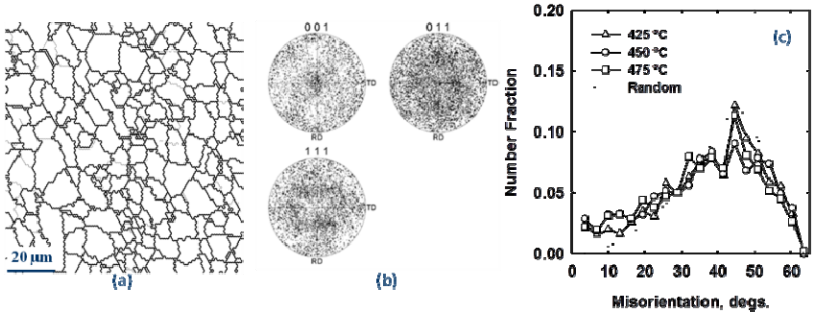

Figure 4. The grain map (a) shows the boundaries of equiaxed grains after heating of AA5083 to 450°C. A near random texture, (b), and misorientation distribution, (c), are evident.

A transition in stress exponent is evident in the elevated temperature tension test data of this AA5083 material, as illustrated in Fig. 5, and corresponding elongation data (not shown) indicated ductility up to 400 pct. elongation in the

GBS regime. The transition in stress exponent is accompanied by distinct transitions in microstructure and microtexture as illustrated in Fig. 6. Grain elongation and subgrain formation reflect generation and accumulation of dislocations, as shown in the grain map and misorientation distribution in Fig. 6a. Also, a two-component fiber texture, <001> + <111>, reflects a predominance of slip processes during deformation. Grains in either of these two orientations have sufficient active slip systems to deform in a compatible manner during uniaxial tensile deformation. A random texture persists in the GBS regime (Fig. 6b).

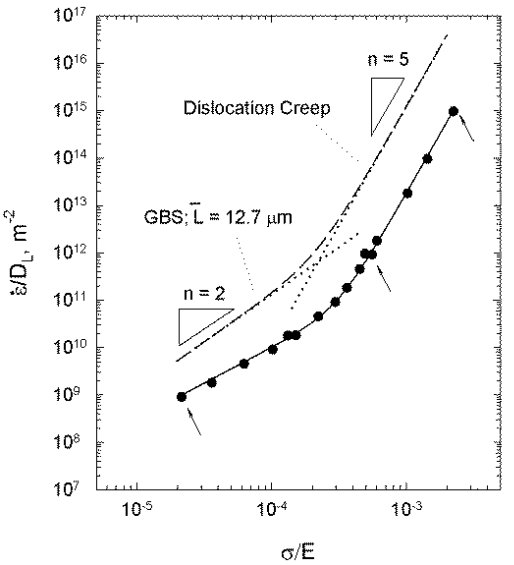

Figure 5. Diffusion compensated strain rate versus modulus compensated stress for fine-grain AA5083. A transition from slip to GBS is seen in the change in slope from n=5 to n=2.

In contrast, the B-type texture of the as-rolled material is retained even after prolonged heating of AA2004 at 450°C, as shown in Fig. 7. Indeed, when compared to the as-rolled condition this texture component has become sharper after six hours of annealing at this temperature (Fig. 7a), and the alternating arrangement of the B_1 and B_2 variants in the grain maps has also become more distinct (Figs. 7b and c). The interface between the two variants appears distinct and transmission microscopy results [14] indicated that the B_1/B_2 interfaces are indeed high-angle grain boundaries.

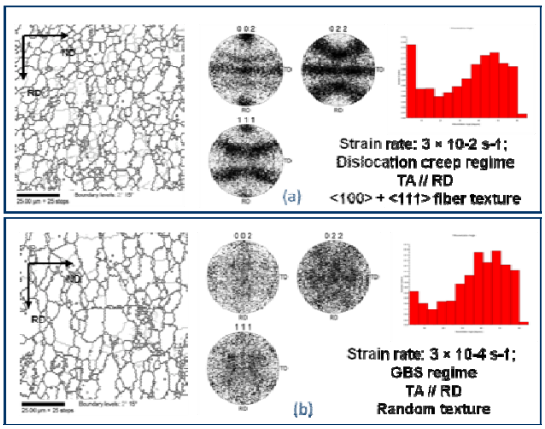

Figure 6. Grain maps, textures and misorientation distributions for AA5083 deformed in (a) the slip creep regime and (b) in the GBS regime.

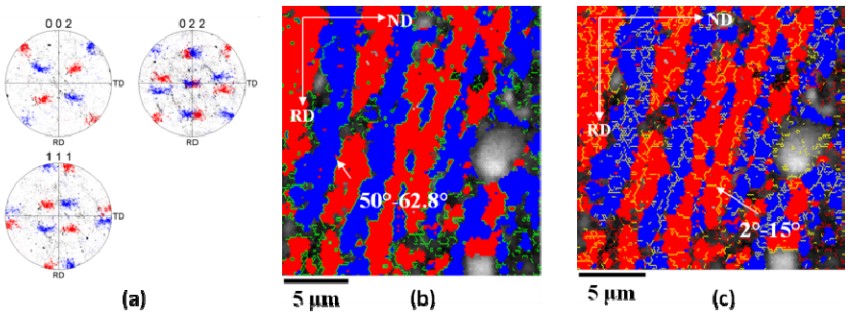

Figure 7. Discrete pole figures, (a) and grain maps (b) and (c) showing the retention and sharpening of the B-texture component after six hours of annealing of AA2004 at 450°C.

Furthermore, the AA2004 material exhibits a strain rate sensitivity coefficient $m \cong 0.5$ when flow stress data were acquired at a true strain $\varepsilon = 0.1$, and ductility >600pct. elongation during tensile deformation at a nominal strain rate $\dot{\varepsilon} = 10^{-2} s^{-1}$ at 450°C (Fig. 8a and b). These mechanical characteristics are accompanied by the progressive development of a random texture component and a corresponding reduction in intensity of the B-texture component, as shown in Figs. 9a and c. Also, the band-like structure that was evident in the annealed material becomes increasingly fragmented as the high-angle interfaces between the bands undergo grain boundary sliding with the resulting grains rotate randomly during deformation (Figs. 9b and d).

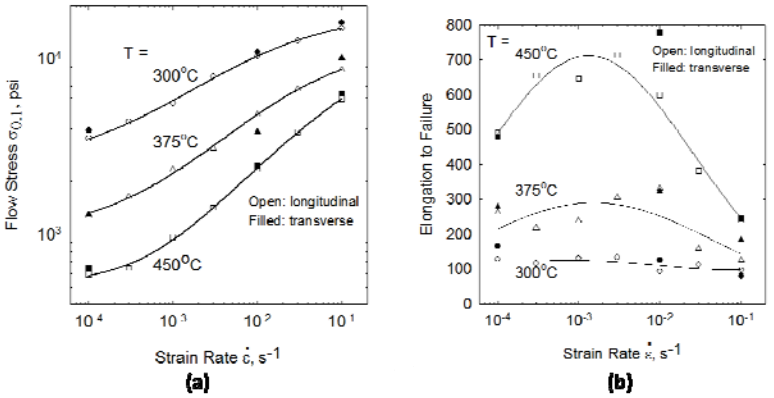

Figure 8. Flow stress (a) and ductility (b) data for elevated temperature tension testing of AA2004 showing peak strain rate sensitivity and ductility at T = 450°C and a strain rate of $10^{-2}s^{-1}$.

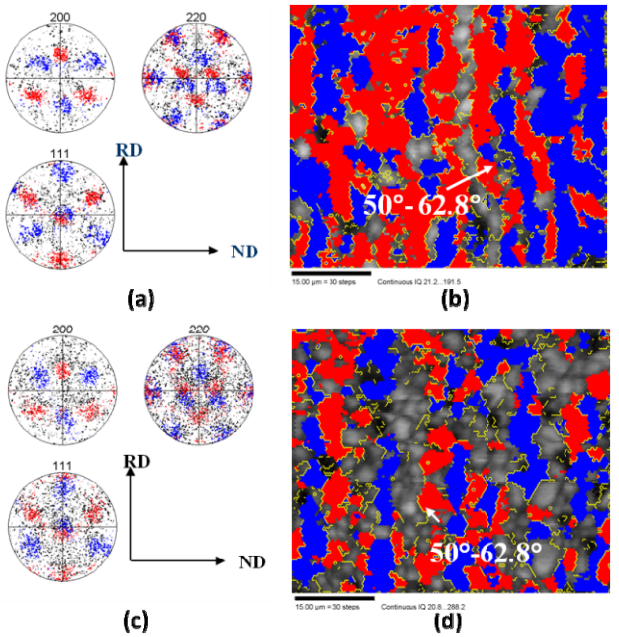

Figure 9. Discrete pole figures (a) and (c), and grain maps (b) and (d) for AA2004 deformed at 450°C and strain rate of $10^{-2}s^{-1}$ to a strain of 110pct. (upper plots; a and b) or 200pct. (lower plots; c and d)

3.3. Mechanisms of recrystallization

Altogether, the foregoing data indicate that there are two distinct recrystallization routes to produce superplastic microstructures in aluminum alloys. The discontinuous mechanism takes place in AA5083 and reflects the presence of a dispersion of constituent particles on the order of 1.0μm in size that are sites for the formation of fine cells or subgrains which, in turn, serve as embryos of new grains. Equiaxed grains 7 - 8μm in size reflect site-saturated nucleation of recrystallization. The presence of the Mg solute in 5083 material may also retard grain coarsening and facilitate superplastic response.

The continuous mechanism in AA2004 reflects the presence of a uniform dispersion of nanometer-sized Al_3Zr particles that retard migration of boundaries during heating and annealing. Thus, the band-like structure developed during prior cold rolling is retained. Dislocation reaction during heating and annealing apparently results in the formation of distinct, high-angle (60°) boundaries that, in turn, are capable of sustaining GBS. It is postulated that slip and GBS contribute to the total strain at the initiation of straining, until sufficient band interfaces re-orient to support grain boundary sliding due to resolved shear from the applied stress. From measurement of the strain rate sensitivity coefficient, it appears that GBS predominates from a strain as small as $\varepsilon = 0.1$.

4. Bibliography

[1] O.D. Sherby and O.A. Ruano, *Superplastic Forming of Structural Alloys,* TMS, Warrendale, PA (1982) 241

[2] T.G. Langdon, *Metall. Trans. A*, 13A (1982) 689

[3] O.D. Sherby and J. Wadsworth, *Deformation Processing and Microstructure*, ASMI, Materials Park, OH (1984) 355

[4] O.A. Ruano and O.D. Sherby, *Rev. Phys. Appl.*, 23 (1988) 808

[5] R.D. Doherty, et al., *Mater. Sci. Engng. A*, A238 (1997) 219

[6] F.J. Humphreys, *Acta Metall.*, 25 (1977) 1323

[7] F. Weinberg, *Trans. AIME*, 212 (1958) 808

[8] B.L. Adams, *Metall. Trans. A*, 17A (1986) 2199

[9] V. Randle and O. Engler, *Intro. Texture Analysis: Macrotexture, Microtexture and Orientation Mapping*, Gordon and Breach (2000)

[10] M. T. Pérez-Prado, et al., *Metall. Mater. Trans. A*, 29A (1998) 485

[11] T. R. McNelley, et al., *Philos. Trans. Roy. Soc. London*, 357 (1999) 1683

[12] M. Eddahbi, et al., *Metall. Mater. Trans. A*, 32A (2001) 1093

[13] M.T. Pérez-Prado, et al., *Acta Mater.*, 49 (2001) 2259

[14] T.R. McNelley, et al., *Metall. Mater. Trans A,* 33A (2002) 279

[15] M.T. Pérez-Prado, et al., *Mater. Sci. Engng. A*, A342 (2003) 216

[16] M.A. Kulas, et al., *Metall. Mater. Trans. A,* 36A (2005) 1249

[17] T.R. McNelley, et al., *Metall. Mater. Trans. A,* 39A (2008) 50

5. Acknowledgements

Financial support from General Motors and the University of Texas – Austin (from 2000 – 2008; Dr Paul Krajewski and Prof Eric Taleff) is acknowledged.

International Symposium on Plastic Deformation and Texture Analysis
Alcoy (Spain) 24-25 September 2012
25-38

On the limits of strain hardening by plastic deformation

J. Gil Sevillano

CEIT and TECNUN, University of Navarra, M. de Lardizabal 15, 20018 San Sebastián, Spain

Abstract

This paper presents a broad picture of the theoretical and experimental limits of strengthening by dislocation accumulation alone (i.e., strengthening from, exclusively, dislocation-dislocation interactions) induced by large plastic strains imparted at temperatures and strain rates where diffusion does not play any significant role. From a practical point of view, this topic connects with the strengthening potential of the so-called "severe plastic deformation processes", SPD processes, so intensively investigated in the last two decades.

Resumen

Se presenta una indagación sobre los límites teóricos y experimentales del endurecimiento por deformación plástica mediada por dislocaciones cuando los mecanismos de endurecimiento se reducen a la interacción entre dislocaciones; es decir, sobre el límite de endurecimiento por deformación para muy grandes deformaciones plásticas en ausencia de procesos difusionales, de mecanismos de confinamiento del deslizamiento entre intercaras y de contribución de segundas fases. La discusión es pertinente para calibrar el potencial de los procesos de "deformación plástica severa" (*severe plastic deformation, SPD processes*: ECAE, HPT, ARB, etc.), hoy de gran actualidad.

Keywords: Strain hardening, plastic deformation, dislocation density, severe plastic deformation, amorphization limit

Palabras clave: Endurecimiento por deformación, deformación plástica, densidad de dislocaciones, deformación plástica severa, límite de amorfización.

1. Introduction

If dislocation density of crystalline matter could be made to increase unabatedly by strain hardening without storage processes being totally cancelled by dynamic recovery or recrystallization mechanisms, the increasing lattice disorder might lead to an amorphization transition of the dislocated crystalline solid when long-range order ceased to exist [1]. Alternatively to such conjectural transition, dynamic processes of local lattice reorganisation in a plastically deforming crystal may leave the average limit configuration of dislocations (or grain boundaries) invariant to further deformation before reaching the hypothetical amorphization limit (a crystalline dynamic steady state). Reaching anyone of these two limits puts an end to the strain hardening ability of a crystal.

Amorphization by severe plastic deformation (SPD) is indeed observed to occur in alloys of high glass-forming-ability (GFA) but not in pure metals or dilute metallic alloys. Alloying for high GFA is meant to weaken the thermodynamic stability of the crystalline phase with chemical and structural disorder contributions to its free energy. Here we try to inquire on the limits to strain-induced dislocation density (and associated strengthening) in pure metals and in the notional or real possibility of their dislocation-mediated amorphization without recourse to any other structural disorder injection (irradiation damage, nano-grain structure, etc.).

2. Some experimental values

Atomistic simulations of plastic deformation of crystals of pure metals in conditions far from equilibrium (very high plastic strain rate) show peak (unrelaxed) dislocation densities up to 10^{18} m^{-2} without amorphization that decrease to 10^{16} m^{-2} upon relaxation(shocked Cu or Ni); maximum experimental values measured after post-shock recovery are 10^{16} m^{-2} too [2, 3]. Thus the figure 10^{18} m^{-2} provides us with a lower bound for the amorphization limit of FCC pure metals.

In Cu single-crystals isothermally deformed at 4.2 K, a dislocation density of 10^{17} m^{-2} has been deduced from electrical resistivity measurements [4]. Estimations of the terminal dislocation density experimentally reached in SPD processes of pure metals or dilute single-phase alloys are of the same order of magnitude, 10^{16} m^{-2} - 10^{17} m^{-2} [5-7], far from the hypothetical amorphization limit, $\rho > 10^{18}$ m^{-2}.

3. The absolute or "natural" dislocation density limit

3.1. Obvious upper bounds

An obvious upper bound for the dislocation density limit is obtained by assuming that a dislocation line passes through every atom:

$$\rho_{\max} < \frac{b}{\Omega} \cong 2 \cdot 10^{19}\,\mathrm{m}^{-2} \tag{1}$$

where an effective dislocation core radius $r_c \approx b \approx 0.25\,\mathrm{nm}$ and an atomic volume $\Omega \approx 1.2 \cdot 10^{-2}\,\mathrm{nm}^3$ have been assumed.

A better upper bound is obtained from the dislocation density derived by assuming that the dislocation cores fill the whole volume. For screw dislocations, the core volume per length b is πb^3. Then

$$\rho_{\max} < \left(\pi b^2\right)^{-1} \cong 5 \cdot 10^{18}\,\mathrm{m}^{-2} \tag{2}$$

For improving this type of upper bound we should know the geometrical percolation threshold for random networks of cylindrical tubes of the dislocation core radius.

3.2. The densest 3D dislocation network

A dislocation network in 3D is mainly constituted of triple junctions of segments, only in lesser proportion of double or quadruple junctions [8,9]. A randomly oriented 3D network of segments of equal size 2*R* meeting at triple nodes can be mapped on a 3D random packing of mono-size tangent spheres of radius *R* and coordination number *Z* = 3. The fractional packing *X* of such stack of spheres is [10]:

$$X = \frac{Z}{Z + 2\sqrt{3}} \tag{3}$$

On account of the segment length per unit volume of a sphere being $9/4\pi R^2$ and assuming 2*b* as lower bound for the length of the segments of a dislocation network, we obtain for the densest possible dislocation network of the assumed configuration,

$$\rho_{\max} \leq \frac{27}{4\left(3+2\sqrt{3}\right)\pi b^2} \cong 1.044\left(\pi b^2\right)^{-1} \cong 5\cdot 10^{18}\ \mathrm{m}^{-2} \qquad (4)$$

i.e., no difference with the previous upper bound value, eq. (2).

3.3. An estimation based on the transition from low-angle to high-angle boundaries

The minimum inter-dislocation distance observed in sub-boundaries, $h_{\min}$, constituted of periodically spaced lattice dislocations ($\Sigma 1$ grain boundaries) before their cores spread on the boundary surface becoming high-angle boundaries provides with a limit to the dislocation density, although strictly valid for 2D dislocation array. For {001} twist boundaries or for symmetrical [001] tilt boundaries in Au, such misorientation limit is $\theta_{\max} \cong 25^{\circ}$ [11, 12]. On the assumption that such minimum distance condition also holds for 3D dislocation arrays,

$$b\sqrt{\rho_{\max}} \approx \frac{b}{h_{\min}} = 2\sin\frac{\theta_{\max}}{2} \cong 0.43 \qquad (5)$$

$$\rho_{\max} \approx 3\cdot 10^{18}\ \mathrm{m}^{-2} \qquad (6)$$

Again we obtain a figure of the same order of magnitude of the previous upper bounds.

3.4. The mechanical threshold proposed by Cotterill [1]

If the screening distance of the stress field of a dislocation line is of the order of the interdislocation distance, we can look each dislocation as an isolated tube of outer radius R and inner radius the radius of the core, r_c, with R

$$R \cong \rho^{-1/2} \qquad (7)$$

The core shear distortion must be supported by the shear resistance of the tube of thickness $\left(R - r_c\right)$ constituted of perfect lattice, i.e., per unit area, by the ideal stress for dislocation-free crystallographic slip, $\tau_i \approx G/10$. The tube would be mechanically stable as far as the total relaxation of the core energy

per unit length, E_c, could occur upon a virtual shear displacement b of the tube wall:

$$\tau_i b(R - r_c) \le E_c \tag{8}$$

The specific core energy is $Gb^2/20 \le E_c \le Gb^2/10$ [13]. We thus arrive to the inequality

$$\rho \le (4b^2)^{-1} \approx 4 \cdot 10^{18}\ \mathrm{m}^{-2} \tag{9}$$

Cotterill [1] used a larger estimation for the specific core energy and consequently proposed a smaller value for the dislocation density limit.

3.5. The thermodynamic limit

In the elastic isotropy approximation, the dislocation line energy per unit length of dislocation line making an angle θ with its Burgers vector is composed of a core term plus an elastic energy term. Assuming again $\rho^{-1/2}$ as screening distance [13]

$$E_d = E_c + AGb^2 \ln\left(\frac{1}{b\sqrt{\rho}}\right),\ A = \frac{1 - \nu\cos^2\theta}{4\pi(1-\nu)} \tag{10}$$

Neglecting entropic contributions (the dislocation entropy per atom length of dislocation line is approximately $0.8k_b$ for FCC or BCC crystals, where k_b is the Boltzmann constant [14]), at a given temperature and pressure, the free energy per unit volume of a crystal containing a dislocation density ρ is

$$G_V(\rho) \cong \rho\left[E_c + AGb^2 \ln\frac{1}{b\sqrt{\rho}}\right] \tag{11}$$

Unbounded spontaneous dislocation multiplication would only occur for $G_V(\rho)$ becoming negative. According to eq. (11) this would require an impossible critical dislocation density $\rho_c = 4 \cdot 10^{19}\ \mathrm{m}^{-2} > \rho_{\text{upper bound}}$. Such a dislocation catastrophe is only conceivable with entropic cooperation at very high temperature, of the order of the melting point (see [15, 16] for recent versions of models of dislocation-mediated melting).

The applied stress does not represent any significant help for a catastrophic dislocation multiplication. A hypothetical increase of the stored dislocation density by homogeneous nucleation and incorporation of a loop into the current dislocation configuration upon a slip increment represents

$$\frac{d\rho}{d\Gamma} \approx \frac{2\sqrt{\rho}}{b} \tag{12}$$

The contribution of a dislocation density ρ to the critical resolved shear flow stress is (disregarding "friction" stress contributions and in the absence of confinement effects to the free dislocation slip) composed of terms arising from long-range ("Taylor"hardening) and short-range (forest hardening) interactions with any mobile dislocation [17-19],

$$\frac{\Delta\tau_c(\rho)}{Gb\sqrt{\rho}} = \alpha = (\alpha_{lr} + \alpha_{sr}) \approx \left[0.1 + 0.03\ln\left(\frac{1}{b\sqrt{\rho}}\right)\right] \tag{13}$$

Precise figures for these terms require MD and DDD simulations. With the numerical values adopted here, the "typical" figure for dislocation strengthening is obtained : $\Delta\tau_c\left(\rho = 10^{12}\, m^{-2}\right) = 0.35Gb\sqrt{\rho}$.

From eqs. (12) and (13), the external work per unit volume upon a dislocation density increase from homogeneous dislocation nucleation is

$$\frac{dW_V}{d\rho} \approx \frac{\alpha G b^2}{2} \tag{14}$$

The corresponding stress-assisted rate of change of free energy would be

$$\frac{1}{Gb^2}\frac{dG_V}{d\rho} = \frac{E_c}{Gb^2} + A\left[\ln\left(\frac{1}{b\sqrt{\rho}}\right) - \frac{1}{2}\right] - \frac{\alpha}{2} \approx 0.010 + 0.065\ln\left(\frac{1}{b\sqrt{\rho}}\right) \tag{15}$$

The contribution of the applied stress to the free energy change would only be relevant for $\rho > \rho_{\,upper\ bound} \cong 5\cdot 10^{18}$ m^{-2}.

4. Beyond the dislocation density limit

From different perspectives, we have arrived to a similar "natural" or absolute dislocation density limit, 10^{18} m$^{-2} < \rho_{\max} \leq 5\cdot 10^{18}$ m^{-2}. Beyond such absolute

limit, Cotterill conjectured that the structure would reorganise to a state of permanent disorder, i.e., a glassy sate if the temperature was below the glass-transition temperature of the material, $T < T_g$ (the crystal would instead melt if $T \geq T_g$).

Remarkably, some early metallic glass models provide quantitative support to such dislocation-mediated amorphization hypothesis: Koizumi and Ninomiya [20] found that the radial distribution of amorphous Ge can be matched by that of a diamond Ge lattice regularly filled with screw lattice dislocations of density $\rho = 0.25b/\Omega = 4.4 \cdot 10^{18}\ \mathrm{m}^{-2}$; similarly, for a model of glassy Fe constituted of randomly packed spheres, Yamamoto and Doyama [21] calculated a density per unit volume $\rho = 3.4 \cdot 10^{18}\ \mathrm{m}^{-2}$ of chains of connected large Bernal's holes, that they assimilated to dislocation cores.

Further support to our figure is provided by its reasonable agreement with the dislocation density needed for increasing the free energy of solid crystals of pure metals at room temperature until the free energy of their respective liquids undercooled to the same temperature (the necessary thermodynamic condition for the crystal to amorphous transition). The values of such free energy increments for Cu, αFe and Nb (calculated with ThermoCalc®) are, respectively, 10, 16 and 25.5 kJ mol^{-1}; using eq. (11) for the free energy per unit volume as a function of dislocation density, the required density values are $2.5 \cdot 10^{18} < \rho \leq 6 \cdot 10^{18}\ \mathrm{m}^{-2}$.

Thus criteria based on structural, mechanical or thermodynamic considerations all converge around the same figure for the "natural" limit of the dislocation density. Another question is how the amorphization would occur from a mechanistic point of view. As stated in a recent publication, despite the enormous amount of literature on melting of superheated crystals or on "cold-melting" of crystals below their thermodynamic melting temperature, "*what happens at the atomic scale as a solid loses crystalline order remains an open question*" [22].

5. Virtual dislocation strengthening limit

For the lower and upper bounds of the dislocation density limit, according to eq. (13)

$$10^{18}\ \mathrm{m}^{-2} < \rho_{\max} \leq 5 \cdot 10^{18}\ \mathrm{m}^{-2}$$

$$0.035 \le \frac{\Delta\tau_c(\rho_{\max})}{G} \le 0.066 \tag{16}$$

Interestingly, this range is of the same order of the range of shear strengths of metallic glasses, spanning from the value for heterogeneous nucleation of the irreversible deformation to that for homogeneous nucleation [23-26]:

$$0.03 \le \frac{(\tau_c)_{MG}}{G_{MG}} \le 0.1 \tag{17}$$

The shear elastic modulus of the metallic glasses, G_{MG}, is about 25% smaller than the modulus of the crystalline material of the same composition. Also notice tat the validity of eq. (13) for the dislocation densities used for calculating the inequality (16) is questionable, as the corresponding mean inter-dislocation distances are only a few times the interatomic distances.

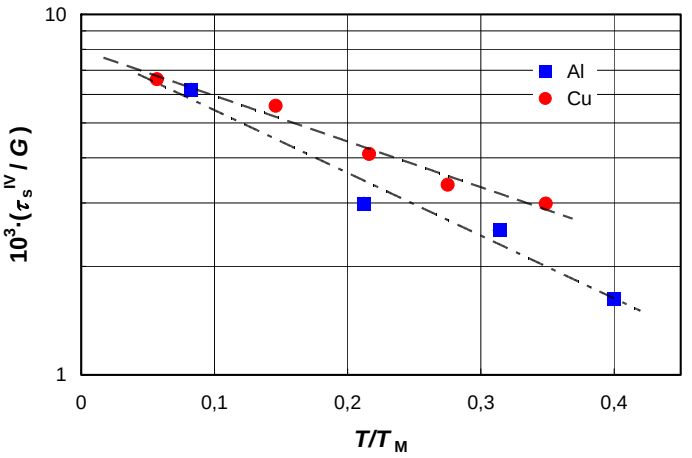

Figure 1. Stage IV saturation stress of copper and aluminium as a function of homologous temperature. Results from torsion tests, Alberdi [28], calculated using an orientation factor M=1.5.

6. Feasible limits by strain hardening

Plastic stress-strain behaviour of crystalline materials is characterized by successive “deformation stages”, I, II, etc., each of them dominated by a different strain hardening process of dislocation storage/annihilation [27]. For

many materials and through most strain paths, the dislocation density limit corresponds to the saturation flow stress that puts an end to Stage IV, the stage of large plastic deformations, $\bar{\varepsilon} > 1$. Despite the intense research activity on SPD processes, there are few systematic studies on the temperature and strain rate dependence of such saturation stress, τ_s^{IV}. For FCC metals, results from Alberdi [27, 28], fig. 1, indicate that its temperature dependence is similar to that of the virtual saturation stress of Stage III; the athermal extrapolation shows

$$\frac{\tau_s^{IV}\Big|_{T=0}}{G} \cong 8 \cdot 10^{-3} \tag{18}$$

From eq. (12)

$$b\sqrt{\rho_s^{IV}} \leq 0.04 \ , \ \rho_s^{IV} \leq 2.6 \cdot 10^{16}\ \mathrm{m}^{-2} \tag{19}$$

This limit is probably also valid for HCP or BCC metals above its transition temperature when largely strained by monotonic rolling or torsion, judging by available values from torsion tests. This saturation stress is reached from a balance between dislocation storage and dynamic recovery processes and it is not due to the exhaustion of the capability of dislocation storage of the lattice.

When extraordinary plastic strain gradients are present during deformation, as it occurs in wire drawing of BCC or HCP metals, the persistent storage of geometrically necessary dislocations, GND, enhances the strength and dislocation density levels well above the values given in eqs. (18) and (19), but still much smaller than the estimated "natural" upper bounds of ineq.(16), see Table 1. Results of strain hardening from SPD processes are typical of Stage IV in the case of ECAP and above them in the case of high pressure torsion, HPT, Fig. 2, although, in general, below the BCC or HCP wire drawing results. The values of Table I do not necessarily correspond to the absolute limits of GND density allowed by the lattice; they are the current maximum values observed and they are (with the exception of Nb) flow stresses measured when strain hardening is still very high; further straining was not performed because of technological reasons. Nevertheless, the gap between the current experimentally observed dislocation strengthening limits and the strength presumed for the amorphization limit can only be filled today by recourse to narrowly confined slip by introducing a high density of difficult-to-penetrate interfaces in the structure or by second-phase strengthening [5, 33].

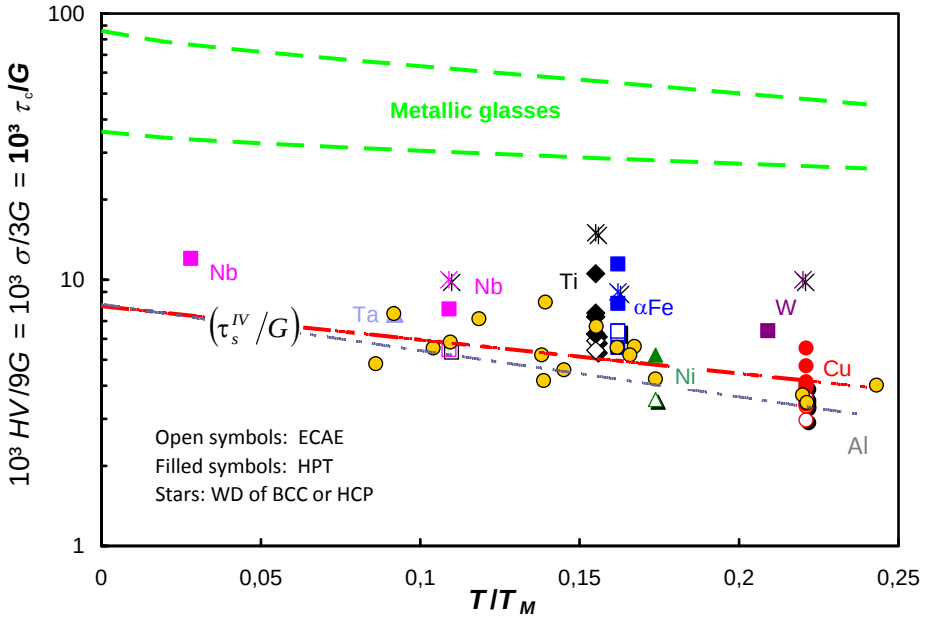

Figure 2. Critical resolved shear stress (estimated from Vickers microhardness, *HV*, or from tensile strength, σ) of different heavily deformed pure metals as a function of the homologous temperature of deformation. Dotted curves: saturation stress of Stage IV of Cu and Al (torsion tests [28]) and strength range for irreversible deformation of metallic glasses [23-26], MG (the lower curve is the strength for heterogeneous nucleation of irreversible deformation of MG, the upper one is the "intrinsic ideal strength" of MG). See Appendix for SPD references.

7. Conclusion

Using several independent assumptions it is concluded that the absolute or "natural" virtual dislocation density limit of crystalline materials lies in the range $10^{18}\ \mathrm{m}^{-2} < \rho_{\max} \leq 5 \cdot 10^{18}\ \mathrm{m}^{-2}$. For pure metals amorphization would occur upon reaching such limit. The predicted strength for the dislocation density limit is of the order of the strength of the corresponding metallic glass. Current maximum quoted dislocation densities and strengths imparted by SPD processes to pure metals are far from the absolute limit.

Table 1. CRSS stresses calculated from maximum quoted tensile flow stress values after large-strain axisymmetric wire drawing of BCC or HCP pure metals (assuming an orientation factor $\bar{\sigma}/\tau_c = 3$). Dislocation densities estimated according to eq. (13). Wire drawing performed at room temperature but for tungsten (started at 800ºC, finished at 550ºC).

Metal	$\tau_{\max}/G$	ρ (10^{16} m^{-2})	Ref.
Nb	0.010	4	[29]
W	0.010	4	[30]
αFe	0.009	3.2	[31]
A70 Ti	0.015	12.4	[32]

8. Bibliography

[1] R.M.J. Cotterill, Phys. Letters **60A** (1977) 61.

[2] E.M. Bringa, K. Rosolankova, R.E. Rudd, B.A. Remington, J.S. Wark, M. Duchaineau, D.H. Kalantar, J. Hawreliak, J. Belak, Nature Mater., **5** (2005) 805.

[3] H.N. Jarmakani, E.M. Bringa, P. Erhart, B.A. Remington, Y.M. Wang, N.Q. Vo, M.A. Meyers, Acta Mater., **56** (2008) 5584.

[4] M. Niwczas, J. D. Embury, "The Integration of Material, Process and Product Design", Zabaras et al. (eds), Balkema, Roterdam (1999).

[5] J. Gil Sevillano, J. Physique III, 1 (1991) 967.

[6] R. Valiev, R.K. Islamgaliev, I.V. Alexandrov, Progr. Mater. Sci., 45 (2000) 103.

[7] A.P. Zhyliaev, T.G. Langdon, Progr. Mater. Sci., 53 (2008) 893

[8] R. Madec, B. Devincre, L. Kubin, T. Hoc, D. Rodney, Science, 301 (2003) 1879.

[9] V. Bulatov, L. Hsiung, M. Tang, A. Arsenlis , M. Bartelt, W. Cai, J. Florando, M. Hiratani, M. Rhee, G. Hommes, T. Pierce, T. Diaz de la Rubia, Nature, 440 (2006) 1174.

[10] C. Song, P. Wang, H.A. Makse, Nature, 453 (2008) 606.

[11] S.E. Babcock, R.W. Baluffi, Philos. Mag., 55 (1987) 643.

[12] E.P. Kvan, R.W. Baluffi, Philos. Mag. A, 56 (1987) 137.

[13] J.P. Hirth, J. Lothe, "Theory of Dislocations", John Wiley and Sons, 2nd ed. , New York (1982).

[14] J. Friedel, Philos Mag. A, 45 (1982) 271.

[15] L. Burakovsky, D.L. Preston, R.R. Silbar, Phys. Rev. B, 61 (2000) 15011.

[16] L. Gómez, A. Dobry, Ch. Geuting, H. T. Diep, L. Burakovsky, Phys. Rev. Letters, 90 (2003) 095701.

[17] A.J.E. Foreman, Philos Mag., 15 (1967) 1011.

[18] D. Gómez-García, B. Devincre, L.P. Kubin, Phys. Rev. Letters, 96 (2006) 125503.

[19] B. Devincre, L.P. Kubin, T. Hoc, Acta Mater., 54 (2006) 741.

[20] H. Koizumi, T. Ninomiya, J. Phys. Soc. Jpn., 44 (1978) 898.

[21] R. Yamamoto, M. Doyama, J. Phys. F, Metal Phys., 9 (1979) 617.

[22] M. Forsblom, G. Grimvall, Nature Mater., 4 (2005) 388.

[23] W.L. Johnson, K. Samwer, Phys. Rev. Lett. 95 (2005) 195501.

[24] C.E. Packard, C.A. Schuh, Acta Mater., 55 (2007) 5348.

[25] Y.Q. Cheng, E. Ma, Acta Mater. 59 (2011) 1800.

[26] L. Tian, Y.-Q. Cheng, Z.-W. Shan, J. Li, C.-C. Wang, X.-D. Han, J. Sun, E. Ma, Nature Comms., 3:609 (2012) 1.

[27] J. Gil Sevillano, in "Materials Science and Technology. A Comprehensive Treatement", vol.6, "Plastic deformation and fracture of materials", H. Mughrabi, editor., ch. 1, p. 19. VCH, Weinheim, Germany (1993).

[28] J.M. Alberdi, doctoral thesis, University of Navarra, San Sebastián (1985).

[29] W.A. Spitzig, P.D. Krotz, Scripta Mater., 21 (1987) 1143.

[30] A. Burwood-Smith, Fibre Sci. Technol., 3 (1970) 105.

[31] G. Langford, P.K. Nagata, R. J. Sober, W.C. Leslie, Metall. Trans., 3 (1972) 1843.

[32] C. P.Biswas, PhD thesis, MIT, Cambridge, Mass., USA, 1973.

[33] J. Gil Sevillano, Mordica Lecture, Milwaukee, USA, 2010 (Wire J. Int., nº 1(2011) 58).

9. Acknowledgements

The author acknowledges J.M. Martínez Esnaola, D. González, J. Alkorta, L.P. Kubin and B. Devincre, for many discussions. T. Gómez-Acebo made the ThermoCalc® calculations. Financial support from the Spanish Ministry of Science and innovation, Project MAT2010-17958, "Insitutests" and the Belgian State, Belgian Science Policy, Interuniversity Attraction Poles Programme, Project P7/21, "INTEMATE" is gratefully acknowledged.

APPENDIX – REFERENCES FOR ECAE AND HPT DATA

Copper

ECAE: Dalla Torre *et al.* (2004), Hellmig *et al.* (2004)**, Shih *et al.* (2001), Valiev (2000)*, Valiev (2004)**.

HPT: Duvravina *et al.* (2004)**, Erbel (1979), Saunders and Nutting (1984), Sturges (1980). Stegelmann (2001) and Duvravina and Valiev (2003), quoted by Zehetbauer (2003).

Stage IV saturation CRSS: Alberdi (1984), Gil Sevillano (1993).

Nickel

ECAE: Hollang *et al.* (2004)**.

HPT: Zhilyaev *et al.* (2001, 2003).

α Iron

ECAE: Sús-Ryszlowska *et al.* (2004), Wang *et al.* (2004)**.

HPT: Ivanishenko *et al.* (2004)**, Valiev *et al.* (1996), Wetscher *et al.* (2004).

Niobium

ECAE and HPT: Popov *et al.* (2011, 2012).

Tantalum

HPT: Schuster et al. (2011), Wei *et al.* (2011).

Tungsten

HPT: Wei *et al.* (2006)

Titanium

ECAE: Stolyarov *et al.* (2000)*, Valiev *et al.* (2000).

HPT: Popov *et al.* (1997), Sergeeva *et al.* (2001), Stolyarov and Valiev (2004)**, Valiev (2000*, 2004**).

(*) In Lowe and Valiev (2000).

(**) In Zehetbauer and Valiev (2004).

Data series of HPT saturation stress at RT of 24 pure metals (FCC, BCC and HCP)

Edalati and Horita (2011).

International Symposium on Plastic Deformation and Texture Analysis
Alcoy (Spain) 24-25 September 2012
39-62

Main achievements on the superplastic behaviour of fine-grained ceramics

Arturo Domínguez-Rodríguez and Diego Gómez-García

Departamento de Física de la Materia Condensada, Universidad de Sevilla, P.O. 1065, 41080 Sevilla (SPAIN)

Abstract

Nowadays it is generally accepted that superplasticity is achieved through grain boundary sliding (GBS). The mechanisms accounting for the relaxation of the stresses created during GBS are commonly known as the accommodation process, which are responsible for the strain rate. The steady-state rate is a function of the stress, grain size and temperature throughout the so-called parameters n, p and Q respectively, which determine the accommodation processes. Another feature characterizing superplasticity is the microstructure stability, i.e., grain size and form factor remain practically unchanged during deformation.

Several accommodation processes have been considered, such as diffusion of point defects along the bulk or the grain boundaries, dislocation activity (mainly in metals but not in ceramics due to the difficulty for dislocations to become activated in these materials) and solution-precipitation in second-phase-added materials to favour sintering such as silicon carbide and silicon nitride mainly.

In free-glassy-phase ceramics or with a low amount of impurities, the main controlling-rate mechanism invoked has been the transport of point defects through the bulk or the grain boundaries. In the case of yttria stabilized zirconia, where aliovalent cations segregate to the grain boundaries (GB) creating a local electric field, it is reported that such field controls superplasticity of this ceramics. This statement will be thoroughly discussed in this talk.

Concerning the stress exponent, a value of 2 has been normally reported; to explain this value the interface reaction controlling mechanism has been put

forward. Nevertheless, such idea is linked to severe drawbacks which will be outlined.

The classical mechanism for GBS accommodated by transport of point defects was published in 1973 by Ashby and Verrall (A-V). However this mechanism justifies a n value equal to 1 instead of 2, although a transition from n=2 to n=1 was found upon increasing the flow stress or the grain size.

In this conference, a new model will be presented based on a mechanism of grain-boundary sliding by pure-shear motion under stationary conditions which is accommodated by lattice or grain-boundary diffusion. The prediction of this model regarding the temperature and grain size dependence of the stress exponent and of the effective activation energy are found in agreement with experimental results and literature data on five ceramic systems where dislocation activity could not be recorded: -SiAlON polycrystals, Al-doped SiC polycrystals, nanocrystalline MgO, yttria tetragonal zirconia polycrystals, and alumina ceramics polycrystals.

Keywords: superplasticity, grain boundary sliding, ceramic policrystals, fine grained ceramics.

1-Introduction

Superplasticity is macroscopically defined as the ability of a polycrystalline material to exhibit large elongations at elevated temperatures and relatively low stresses. It is commonly found in a wide range of materials from metals to ceramics (bioceramics or high temperature superconductors, among others) when the grain size is small enough: few micrometers for metals and less than a micron in ceramics.

When processing the ceramic powders to consolidated the ceramic material and in order to obtain fully dense ceramics and to prevent grain growth, which is catastrophic for superplastic achievement, several strategies have been used. Between them the doping with impurities which can segregate or precipitate at the grain boundaries exerting a solute drag on the grain motion inhibiting the grain growth or the addition of second phases with lower melting temperature which can produce densification al low temperature that normally used avoiding grain growth.

Nowadays it is generally accepted that superplasticity is achieved through grain boundary sliding (GBS). The mechanisms accounting for the relaxation of the stresses created during GBS are commonly known as the accommodation process, which are responsible for the strain rate. The steady-state rate is a function of the stress, grain size and temperature throughout the so-called parameters n, p and Q respectively, which determine the accommodation processes. Another feature characterizing superplasticity is the microstructure stability, i.e., grain size and form factor remain practically unchanged during deformation.

Several accommodation processes have been considered, such as diffusion of point defects along the bulk or the grain boundaries, dislocation activity (mainly in metals but not in ceramics due to the difficulty for dislocations to become activated in these materials) and solution-precipitation in second-phase-added materials to favor sintering such as silicon carbide and silicon nitride mainly.

Although grain boundary sliding is recognized as the primary controlling mechanism in superplasticity, the structure and the nature of the grain boundaries when segregation or glassy phases exist will affect the accommodation processes, which control at their turn the strain rate superplasticity. In the case of presence of secondary phases, superplasticity can be affected in several ways. These phases may act as “lubricant”, so that the viscous movement of the glassy phase constitutes the accommodation mechanism for a possible grain boundary sliding process. The grain boundaries are higher diffusivity pathways in presence of a secondary glassy phase than in the case in which those are “clean”, thus improving the material diffusion. Finally, the secondary phase provides a preferential location for the nucleation and growth of cavities during the deformation processes. Depending on which of these features predominates during the deformation, the accommodation mechanism to consider will be viscous flow, solution–precipitation, or cavitation.

The discrepancy between experimental data and the models in the literature will be explained with a new model which will be presented based on a mechanism of grain-boundary sliding by pure-shear motion under stationary conditions which is accommodated by lattice or grain-boundary diffusion.

In this paper, the macroscopic and microscopic aspects of the superplasticity, the accommodation processes, the new model, the applications and the future trends will be addressed.

2-Macro and microscopic superplastic characteristics

Superplasticity was defined as the ability of a polycrystalline material to exhibit large elongation without necking. It was found for the first time in metal for nominally low stresses and relatively high temperatures. It is not clear if the ancient Damascus sword were made by superplastic deformation, but the first report of a very high tensile deformation prior to failure was in 1912 for a (α+β) brass [1], however it was only in the 1960s when the superplasticity in metals and metal alloys began to be study intensively from scientific and commercial point of view.

Superplasticity was confined mainly to metallic alloys since superplasticity requires a small and stable grain size (less than 10 μm), however when in 1975 Garvie et al [2] published their paper in Nature, "Ceramic steel?", and it was shown that ceramics can be used in structural applications, a great effort was done since then to find new ceramics with high toughness, being the processing and sintering of ceramics the keystones in this investigation. This effort leads to obtain fully dense ceramics with equiaxed grain sizes below 1 μm. As a consequence, Wakai et al [3] published the first observation of superplasticity in a 3 mol% yttria-stabilized tetragonal zirconia polycrystal ceramic (YTZP) with a grain size of 0.4 μm (Figure 1).

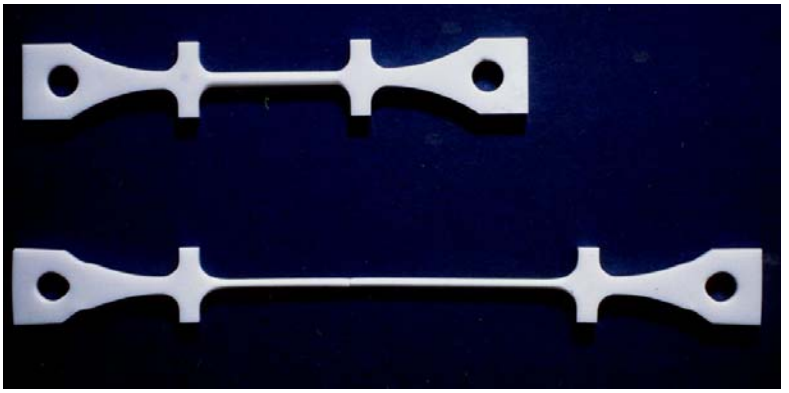

Figure 1. 3YTZP deformed at 1450 ºC and $3x10^{-4}$ s^{-1} (Courtesy to Prof. F. Wakai)

Nowadays, the list of ceramics and ceramics composites with superplastic behaviour is very wide [4-9], and ceramics like high temperature superconductor YBaCuO behave superplastically (cover page of the J. Amer. Ceram. Soc, 97, May 1996 [10]).

Nevertheless, it was only when superplasticity was defined from a microscopic point of view as the deformation due to the grain boundary sliding, when appears new ceramics, intermetallics and metal and ceramic matrix composites materials, and the character of superplastic was enlarged to materials tested in compression, in bending and still in micro-hardness. This lack of definition is at the origin that materials deformed in compression by grain-boundary sliding, which indeed is at the origin of the superplasticity, were not classified as superplastic materials, example can be found [11-13].

From a microscopic point of view, when a polycrystalline material is deformed at high temperatures, grain boundary sliding (GBS) takes place in two different ways:

i) The deformation is due to the flow of point defects, then GBS occurs to maintain grains coherency. This is termed as 'Lifshitz grain boundary sliding' (Figure 2a) and it is called diffusional creep: Nabarro-Herring if the diffusion takes place along the bulk, or Coble if takes place along grain boundaries. In these two cases, each individual grain suffers almost the same deformation as that imposed to the specimen and the grains which are nearest neighbours remain nearest neighbours.

ii) A different situation happens when GBS is responsible for the deformation. In order to release stresses create during GBS, deformation may be accompanied by intergranular slip throughout adjacent grains, by localized slip adjacent to the boundaries or by diffusional process of point defects. Sometimes, formation of triple point fold or the opening up of cracks at the triple points can also accommodate GBS; however, as soon as there is coalescence of voids or cracks, the material fails and that happens at not large deformations. This type of GBS, accommodated by the process described above, is termed as 'Rachinger grain boundary sliding' (Figure 2b). As observed in this figure, the grains retain their shape after deformation in contrast to the variable grain morphology under Lifshitz grain boundary sliding. A detailed analysis of the characteristic of the different type of grain boundary sliding can be found [14].

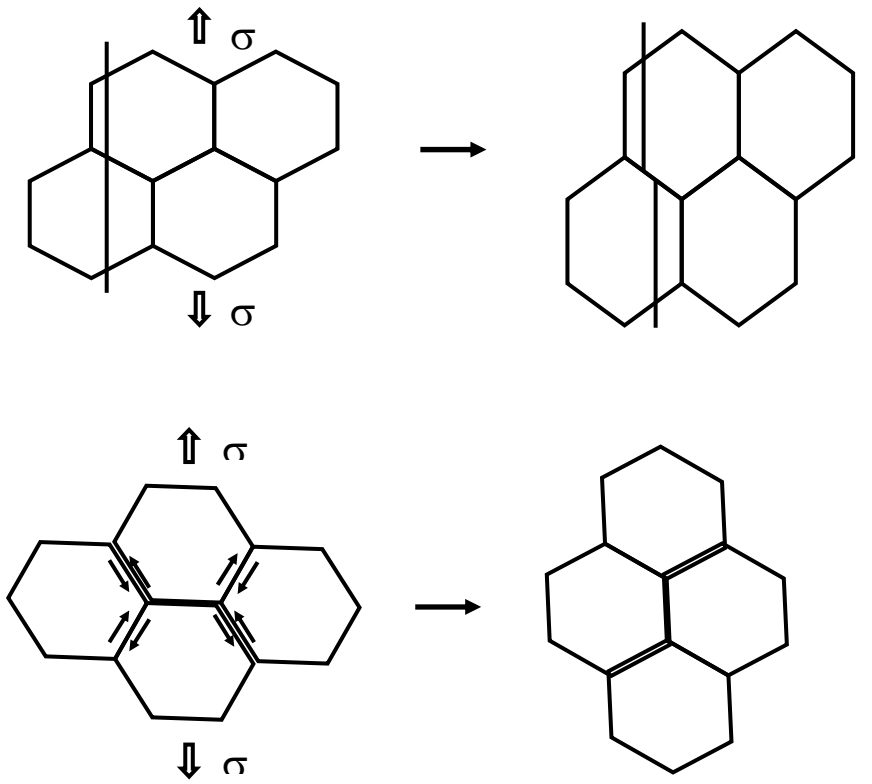

Figure 2. Scheme of grain boundary sliding. a) correspond to Lifshitz grain boundary sliding, b) correspond to Rachinger grain boundary sliding.

The relative motion of two adjoining rigid grains has components parallel and perpendicular to their common grain boundary. The grain boundary sliding is the component parallel to the grain boundary and it is the responsible for 70-80% of the deformation in superplasticity of fine grained ceramics [15-17] as has been shown by measurement of the grain aspect ratio, by SEM and by atomic force microscopy and displayed recently by Duclos [18] in YTZP.

The most visible feature of grain boundary sliding can be observed in Figure 3, which shows the relative motion of grains during superplasticity of Y-TZP [18]. It can observed how two small grains initially separated by two larger grains in contact, become nearer and nearer and finally the larger grains are separated. Several examples of switching events are also shown in the same reference [18].

The perpendicular motion of the two adjoining grains create a stress concentration in the grain boundaries which need to be relaxed in order to proceed the deformation, it is equivalent to a non-conservative motion and it is associated with the diffusional fluxes of the components to/from or along the interfaces or to the dislocation motion, being the main accommodation processes and the rate-controlling process associated with GBS.

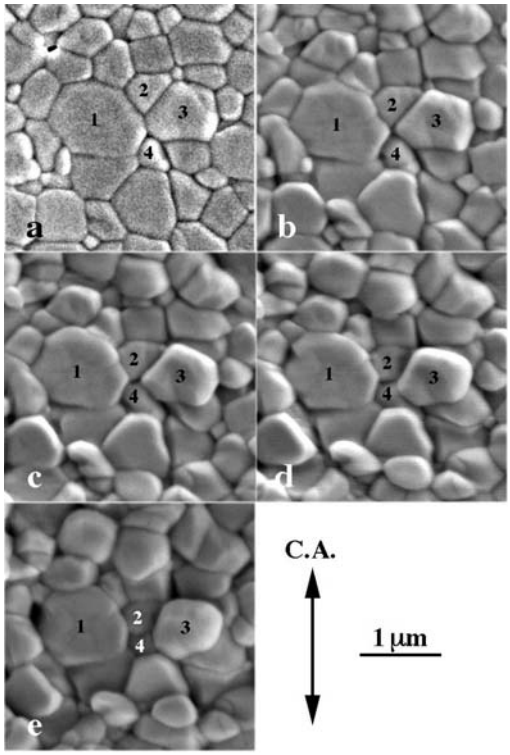

Figure 3. A grain switching event observed during superplastic deformation of Y-TZP. A group of grains exchange their neighbors during deformation. (Courtesy to Prof. R. Duclos)

Recently, the cooperative manner of grain boundary sliding, which reveals itself through sliding of grain groups as an entity, has been demonstrated in some superplastic alloys [19]. Such cooperative grain boundary sliding has been suggested to play an important role for fine-grained ceramics also [20]. However, the direct observation of grain rearrangement during superplasticity of Y-TZP revealed that the influence of cooperative grain boundary sliding was very limited [21].

The strain rate in superplasticity of many metals and ceramics is often expressed by the following semi-empirical equation [8, 22, 23],

$$\dot{\varepsilon} = \frac{AGb}{kT}\left(\frac{b}{d}\right)^{p}\left(\frac{\sigma-\sigma_0}{G}\right)^{n} D \qquad (1)$$

where $\dot{\varepsilon}$ is the strain rate, b is Burgers vector, G is the shear modulus, σ is the stress, σ_0 is the threshold stress, n is the stress exponent, D is the diffusion coefficient [$= D_0 \exp(-Q/kT)$, where D_0 is a frequency factor, Q is the activation energy and k is Boltzmann's constant] , d is the grain size, and p is the grain-size exponent. The value of p is two when the rate controlling process is lattice diffusion, and three when it is grain boundary diffusion. The threshold stress σ_0 is zero in many cases. The threshold stress depends on the nature of the grain boundaries [8, 23].

There are not unique values of creep parameters (p, n and Q) identifying the superplastic behaviour of ceramic-related materials; still not for the same type of materials either. Several factors can affect these parameters, between them the purity of the ceramics including nature of the grain boundaries [6, 8, 23] or the testing conditions, compression or tension when aid-sintering phase are necessary during the processing as in silicon carbide and silicon nitride ones [9].

The different values of the creep parameters are justifying through the accommodation processes controlling superplasticity, which will be analyzed below.

3-Accommodation processes in superplasticity

The accommodation processes are responsible for the rate-controlling superplasticity. There is no a single mechanism to accommodate GBS, even concerning a particular ceramic. As mentioned above, several factors affect the different mechanics, between them it can be mentioned the nature of the impurities present in the grain boundaries, secondary phases, testing conditions. There are three main controlling mechanisms: i) non-conservative movement of dislocations, ii) diffusional flow of point defects and iii) solution-precipitation of matter at the glassy phases. In this section, the different mechanisms for accommodation will be analysed except the non-conservative

movement of dislocations because it is very difficult to activate dislocations in ceramics and it has not been normally considered as a relaxation mechanism. For the sake of clarity, the accommodation process will be described for each type of factor affecting it. In each case, the different situation will be analyzed.

3.1 GBS accommodated by diffusional flow

This type of mechanism is due to a non-uniform flow of point defects: Their fundamental topological features are that the grains in the polycrystals change their neighbors and almost do not change their shape after large deformation. This fact was first observed by Rachinger in polycrystalline metals [25] and modelled by the first time by Ashby and Verrall (thereafter A-V) [26]. The model is a 2-D model; the authors said that a 3-D model may be much more complicated, however only a numerical factor differs both treatment.

In the model, bulk diffusion through the grains and diffusion along grain boundaries are considered. These two processes are always dominant at low stresses because the rates of diffusional flow are usually linear functions of stress whereas those involving dislocation motion are faster than linear.

Ashby and Verrall consider a group of four grains deformed at constant pressure and stress. During this irreversible flow, four irreversible processes take place:

i) Diffuse process by which, grains temporarily change shape.

ii) Grain or phase boundaries are sinks and sources of point defects.

iii) Grain boundary sliding.

iv) Fluctuations of boundary area.

By considering the work done in these four processes, the constitutive equation of the A-V model, when lattice and grain boundary diffusion are taking into account is written:

$$\dot{\varepsilon} = \frac{100\Omega}{kTd^2}\left(\sigma - \frac{0.72\gamma}{d}\right)D_L\left(1 + \frac{3.3\delta D_{gb}}{dD_L}\right) \qquad (2)$$

where Ω is the atomic volume of the diffusion controlling species, $\frac{0.72\gamma}{d}$ is a threshold stress for the grain-switching event and γ is the grain boundary free

energy, δ is the thickness of the boundary and D_L and D_{gb} are the lattice and grain boundary diffusion coefficients, respectively.

The principle of this model for grain rearrangement is shown in figure 2b. This type of grain rearrangement retains the equiaxed grains after large deformation as shown in the typical microstructure features of the polycrystals superplastically deformed [8, 18]. A modified A-V model accounting for a more realistic symmetrical diffusion path has been developed by Spingarn and Nix when diffusional flow occurs only along grain boundaries [27]. Several modifications of the original A-V model have been done by several authors and reviewed in [14]. However, the main features of the original A-V model remain unchanged.

Two main features can be observed from equation 3. First, the strain rate is a linear function of the stress and second, the existence of a threshold stress which is due to the fluctuation of the boundary area during the grain switching. However they conclude that this threshold stress is generally too small. This value has been calculated in the case of NiO for which γ is 1 Jm^{-2} [13] giving a threshold stress according to equation 3 of 0.08 MPa, too small to be measured. Also, in the case of zirconia, where the value of γ is ~0.15 Jm^{-2}, the threshold stress for a grain size of 0.4 μm is around 0.3 MPa, far below the measured values [8, 28, 29]. This suggests us that if a threshold is measured, its origin must be different.

The linear dependence between the strain rate and the stress has been observed in ceramics such NiO with grain sizes between 9 and 21 μm [13]. However, for typical materials with grain size below 1 μm such as many ceramics and ceramic composites, pure and impure metals, solid solution and alloys containing a fine secondary phase dispersed, the dependence between the strain rate and the stress can not be explained by the A-V model [6-8]. In the case YTZP with grain size 0.3-0.5 μm, probably the most widely ceramics studied, values of n between 2 and 5 has been found [8]. A detailed analysis of the n values in YTZP will be done late.

The experimental data show that the stress exponent in superplasticity is 1 for polycrystalline materials with coarse grain size and tend toward 2 when the grain size decreases. A good example can be found in Figure 4 which is a plot of strain rate versus stress at a constant temperature of 1350°C for samples sintered from identical powders but with different grain sizes [30].

This tendency has been found no matter the nature of the grain boundaries and it was point out by Ashby and Verall [26] analysing diffusional creep, for which materials with relatively coarse-grained n is equal to 1 and with fine grain size n is equal to 2. In order to explain this discrepancy, A-V modified their model for an interface-reaction controlled flow [26] and modelled in detail by Artz et al. [31] based on the existence of boundaries dislocations which have been observed by transmission electron microscopy. In these boundary dislocations the Burgers' vector is not a lattice vector and therefore they are constrained to remain in the boundary when they move. The model developed in [31] can justify n equal 2 for solute-drag limited diffusional creep, however the grain size dependence is equal to 1, not observed in many ceramics [6-8].

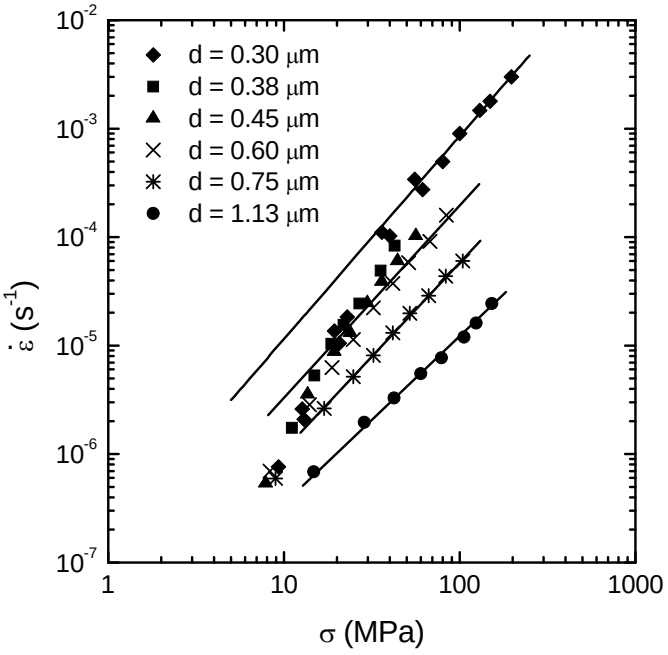

Figure 4. Strain rate vs. the stress at constant temperature for a set of investigated samples deformed at 1625 K. Notice that the samples with the smallest grain sizes exhibit a non-linear dependence due to the threshold stress.

Although this explanation may be adequate for metals, it cannot be applied in ceramics where dislocations at grain boundaries have never been observed, either in the bulk during superplastic deformation. However, the idea that the boundary is not a perfect sink or source for point defects need to be explore in detail, because it may be the key to explain n value different than 1. Another problem comes for the fact that the A-V model is based on the movement of 4 equal hexagonal grains, and it may be changed when a distribution of small grain size exist. A qualitative analysis of the different models to account the geometrical aspect of superplastic flow can be found in [19], however a quantitative analysis need to be done.

This mechanism of GBS accommodated by diffusional flow has been successful used to explain the superplastic behaviour of YTZP. In the case of YTZP, values of p between 1 and 3, of n between 2 and higher than 5 and Q between 450 and 700 kJ/mol have been reported during creep [8].

There are several explanations to justify this scatter in the experimental creep data; a detailed analysis of these mechanisms can be found in [32]. Probably the most plausible explanation for the scatter of the creep parameters is based on a single mechanism involving GBS with a threshold stress (σ_0) [8, 28, 32]. When a threshold stress is introduced into the creep equation, all the creep parameters in YTZP become n=2, p=2 and Q= 460 kJ/mol (the activation energy for cation lattice diffusion in zirconia-yttria system [8]) whatever the stress or temperature of the test is and the data could be fitted to a constitutive equation, which is identical to that found in metals when lattice diffusion is the rate controlling mechanism [33]:

$$\dot{\varepsilon} = 3x10^{10}\frac{(\sigma-\sigma_0)^2}{Td^2}\exp\left(-\frac{460kJmol^{-1}}{RT}\right) = 2x10^{7}\frac{Gb}{kT}\left(\frac{\sigma-\sigma_0}{G}\right)^2\left(\frac{b}{d}\right)^2 D_{lat}^{Zr} \quad (3)$$

The value of this σ_0 was found experimentally [28]:

$$\sigma_0 = 5x10^{-4}\frac{\exp\left(\frac{120kJ/mol}{RT}\right)}{d} \quad (4)$$

with d in μm.

However, the discrepancy comes from the origin of this threshold stress. Two different explanations exist and they will be outlined critically below.

One explanation for the threshold stress has been pointed out in recent papers by Morita & Hiraga [29, 34,35]; they claimed that n values as high as 5 and Q values of 680 kJ/mol, can be linked to the existence of a threshold stress for intragranular dislocation motion, being such motion the accommodation process for GBS. Such hypothesis is based on the observation of dislocation pile-ups as reported in [35].

A dislocation pile-up is not a stable dislocation microstructure, since strong dislocation repulsion of dislocation each other must occur. It remains stable as long as an external applied stress exists. Such stress can be calculated using the equation [63]:

$$\tau = \frac{Gb}{2L} N \tag{5}$$

where τ is the shear stress acting on the pile-up plane, L is the pile-up length and N is the number of pile-up dislocations. Morita & Hiraga reported values of τ for the different pile-ups observed from 351 to 1260 MPa for nominal applied stresses from 15 to 50 MPa, table 1 in [35]. These values for the stress needed for pile-up stability are in full agreement with the values reported of 400 MPa require for dislocation motion in yttria-tetragonal zirconia single crystals deformed at 1400 ºC [36].

Taking into account that for polycrystals the applied stress is 1/3 of the shear stress acting on the pile-up plane, the relationship between the shear stress concentration (τ) and the applied stress σ (τ/σ), lies in the range from 40 to 75, too big to be explained by the stress concentration induced at multiple-grain junction during GBS. Clearly, the dislocations reported by Morita & Hiraga are an artefact, they are not an intrinsic mechanism and they are created during cooling the system after finishing the creep experiment.

Recently, another model has been developed on the basis of the segregation of the yttrium atoms at the grain boundaries to account for σ_0. The model is able to explain quantitatively the dependence of σ_0 with both temperature and grain size [24].

Nowadays it is accepted that yttrium segregates at grain boundaries or at the dislocation cores in YTZP. The origin of this segregation is the relaxation of the elastic energy around yttrium atom as a consequence of the difference between the ionic radius of Y^{3+} and the Zr^{4+}, being around 20 % bigger the Y^{3+}

than Zr^{4+} and has been proved experimentally by means of different techniques [37-42]. The yttrium segregation, it will depend of temperature and bulk concentration (c_b) [43] and it was shown recently that it depends also on the grain size [42]. The space charge potential (V) due to the segregation has been measured by impedance spectroscopy technique as a function of the grain size in a 3 mol% YTZP and it was found that V increases from 0.18 V to 0.25 V when the grain size increases from few tenth of nanometers to more than 1000 nm [42]. Segregation of the cations to the grain boundaries changes the chemical composition as well as the electric space charge at the boundaries, creating a local electric field (E), consequently affecting the deformation mechanisms such as grain boundary sliding; this, in turn, may affect the mechanical behaviour of the zirconia alloy as shown recently in several papers. Details how the segregation can influence the superplasticity in YTZP can be found in references [44,45].

If we assume that the interfacial region between two grains is very narrow and in electrostatic equilibrium, this electric field can be determined as a function of the yttrium bulk concentration, the thickness of the segregation layer (Debye length λ) and of the reduction in energy per atom of dopant when one of them segregates to the grain boundaries (the absorption free energy ΔG). For details, see references [44,45].

During deformation, one grain displaces respect to each other and the work done during this displacement can be written [44, 45]:

$$\delta W = C\frac{1}{2}\varepsilon E^2 \delta V \tag{6}$$

with C a geometrical constant and δV the infinitesimal change of the volume between two grains upon sliding an infinitesimal distance $\delta\xi$. With δ the thickness of the intermediate region between grains and d the grain size, $\delta V = \delta d\,\delta\xi$.

Because the work during the displacement is also equal to the net force F per unit area multiply by $\delta\xi$, and this force can be considered as the force needed to be exercise in order to grain boundary start to slide, it can be considered as the threshold stress (σ_0), which by substituting the different expression can be written as:

$$\sigma_0 = 2\frac{c_b^2\lambda^2}{\varepsilon}\left[\exp\left(-\frac{\Delta G}{kT}\right)-1\right]^2\frac{\delta}{d}\propto\frac{1}{d}\exp\left(-\frac{2\Delta G}{kT}\right) \quad (7)$$

In order to analyse equation (8), it is necessary to know the absorption free energy in YTZP. However, although no experimental data are available for this magnitude, as far as we know, in the case of the solid solution of antimony in cooper, this energy is -0.68 eV $atom^{-1}$ [46]. In this system, the difference between the atomic radius of Sb (r_1 = 1.53 Å) and that of cooper (r = 1.23 Å); the misfit between the two atoms is +0.194, very close to that found in yttia-zirconia solid solution [45]. On the other hand, the shear modulus of both systems, 41 GPa for Sb-Cu [43] and 45 GPa for YTZP [47]. On the other hand, for Y_2O_3-TiO_2, the Ti^{4+} cations have an ionic radius equal to 0.68 Å , whereas that for Y^{3+} is 1.015 Å. That makes an elastic energy equal to 0.60 eV at room temperature [45]. These values are fully consistent with the YTZP system, in which ionic radius are very close to those for Y_2O_3-TiO_2. In consequence, it is logically-accepted that the experimental value in equation (4) is a reasonable value.

As it can be observed in this equation (7), the impurities segregation at the grain boundaries can not only justifies the existence of the threshold stress but also give the grain size and temperature dependence found experimentally.

For second glassy phase ceramics, the accommodation processes are governed by these phases in spite of the diffusional processes occurred during creep. At high temperatures the glassy phase may become less viscous and even liquid and in consequence may account for the plastic deformation. However, viscous flow creep is not regarded as a viable creep mechanism for superplasticity due to its limited deformation, which corresponds to the redistribution of the glassy phase and therefore to the squeeze of these secondary phase from grain boundaries subjected to compression [9].

In the next section, we will analyze the two mechanisms considered to be controlled by secondary phase in ceramics superplasticity.

3.2-Solution-precipitation creep model.

For ceramics with secondary glassy phases, the accommodation processes are governed by these phases in different ways:

- These glassy phases may act as a lubricant for GBS

- Can improve the diffusivity pathways along GB
- Can provide a preferential location for the nucleation and growth of cavities

In this case, the secondary phases melt at temperature lower than the matrix and provided that the crystals are at least partially soluble in the glassy phase, creep may take place by:

- solution of the crystal in the liquid phase at grain boundaries under compression
- diffusion along the liquid phase
- precipitation of the crystalline material at grain boundaries under traction.

The figure 5 represents a schema of this model.

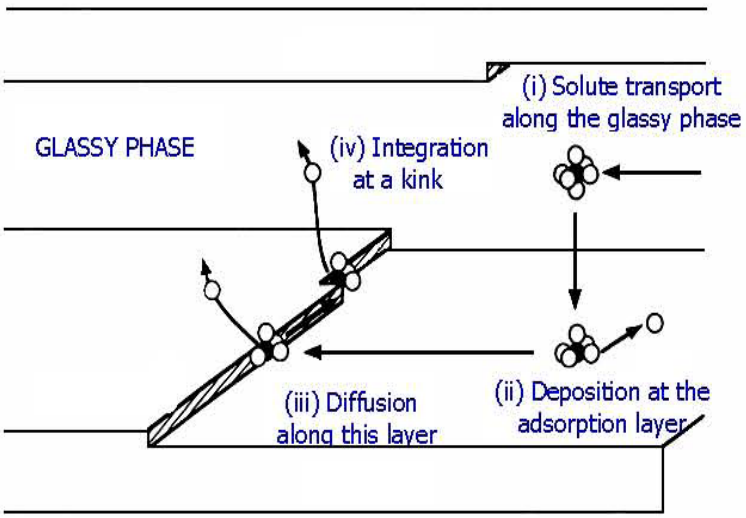

Figure 5. Scheme of the solution-precipitation step model

An important modification of the classical Raj & Chyung [46] model was performed by Wakai [48], assuming that the solution and precipitation take place at steps (kinks) formed at the grain boundaries. The solution-precipitation process involves the movement of these steps, and the strain rate is therefore related to the step velocity and density, with an expression analogous to Orowan's equation for dislocation movement.

Three different cases were analysed by Wakai for the density of steps:

a) The constant density of surface steps is independent on the applied stress.

b) If the initial density of steps is very low, two-dimensional nucleation of the surface steps occurs.

c) If the continuous source of steps is a screw dislocation, then a spiral step is generated.

The combination between the rate controlling process and the density of steps give the different equations of the Wakai's model [48] have been analyzed in detail in [49] and the different equations for these mechanisms are summarized in table I.

Table I. Creep laws as predicted in the solution-precipitation model, according to the kink density and the controlling mechanism [49].

Controlling mechanism	**Density of steps**		
	Constant	**2D-nucleation**	**Spiral step**
Diffusion in the liquid film	$\dot{\varepsilon} \propto \frac{\sigma}{kTd^3} D_L$ (1)		
Diffusion in the adsorption layer	$\dot{\varepsilon} \propto \frac{\sigma}{kTd} D_S$ (1)	$\dot{\varepsilon} \propto \frac{\sigma^n}{kTd} D_S$	$\dot{\varepsilon} \propto \frac{\sigma^2}{kTd} D_S$
Reaction at kink	$\dot{\varepsilon} \propto \frac{\sigma}{kTd} \frac{1}{\tau_K}$ (2)	$\dot{\varepsilon} \propto \frac{\sigma^n}{kTd} \frac{1}{\tau_K}$	$\dot{\varepsilon} \propto \frac{\sigma^2}{kTd} \frac{1}{\tau_K}$

(1) D_L and D_S are the diffusion coefficients in the liquid phase and the adsorption layer

(2) τ_K is a characteristic relaxation time for the integration of solute at kinks.

$\tau_K \propto \exp \frac{\Delta G_K}{kT}$ where ΔG_K is the free enthalpy for the reaction at the kink

4-New model

Quite recently, a new model has been developed to account for the non-correlated motion of grains [50]. It has been proved that sliding motion is not time correlated to the diffusional normal motion. As a consequence of this, the steady-state creep equation must be modified accordingly. Theoretical thoroughly analysis allows proving that the creep equation should follow a law as shown:

$$\dot{\varepsilon} = \frac{\dot{S}}{S} = \frac{2\beta}{(1+\beta)^2}\frac{1}{\delta\tau_D} = \frac{2\delta\tau_S}{(\delta\tau_S + \delta\tau_D)^2} \tag{8}$$

where S is the area of the transversal section of the specimen, $\beta = \delta\tau_S / \delta\tau_D$ is the ratio of the sliding and diffusional times, respectively indicated in that ratio.

The characteristic time for diffusion is straightforwardly obtained from diffusion theory (Fick's law):

$$\delta\tau_D = \frac{d}{\sigma\Omega D_{eff} / kTd} = \frac{d^2}{\sigma\Omega D_{eff}} kT \tag{9}$$

where σ is an effective stress equal to the applied stress minus the threshold stress if that exists, Ω is the atomic volume of the diffusing species controlling accommodation, and D_{eff} is the effective diffusion coefficient.

To evaluate $\delta\tau_S$ we need to know its dependence on temperature and stress and two cases will be considered:

a) Pure single-phase materials in which grain boundary mobility is not limited

b) Systems in which grain boundary mobility is limited by solute drag or grain boundary pinning due to second-phase particles

In the first situation, $\delta\tau_S$ can be written as:

$$\delta\tau_S = \frac{3d^2}{8\mu\gamma} \tag{10}$$

and in this case β is written:

$$\beta = \frac{3\pi}{4}\frac{\sigma\delta}{\gamma}\frac{D_{eff}}{D_{gb}} \tag{11}$$

In the second situation, $\delta\tau_S$ can be written as:

$$\delta\tau_S = \frac{7d^3}{48\gamma\delta\mu} \tag{12}$$

and β as:

$$\beta = \frac{7\pi}{24}\frac{\sigma d}{\gamma}\frac{D_{eff}}{D_{gb}} \tag{13}$$

and depending if β is close to 1 or much smaller several equations can be deduced as shown in table II.

Table II: Different creep equation deduced from the new model as a function of β.

	β <<1	**β≅1**
Non-limited mobility	$\dot{\varepsilon} \cong 2\beta\frac{\sigma\Omega}{kTd^2}D_{eff} \cong 1.5\frac{\pi\delta}{\gamma d^2}\frac{\sigma^2\Omega}{kT}\frac{D_{eff}^2}{D_{gb}}$	$\dot{\varepsilon} \cong \frac{1}{2}\frac{\sigma\Omega}{kTd^2}D_{eff}$
Limited mobility	$\dot{\varepsilon} \cong 2\beta\frac{\sigma\Omega}{kTd^2}D_{eff} \cong \frac{7\pi}{12}\frac{\sigma^2}{\gamma kT}\frac{\Omega}{d}\frac{D_{eff}^2}{D_{gb}}$	$\dot{\varepsilon} \cong \frac{1}{2}\frac{\sigma\Omega}{kTd^2}D_{eff}$

The new model works and more details can be found in [50].

5-How to improve superplasticity

The increasing applications of advanced ceramics in technical areas including aerospace, automobile, sanitary, energy, electronics, biology, etc, often require complex shape manufactured at low prices. The extensive potential applications, together with the possibility of processing of dense ceramics and to form complex structures by superplasticity, have been the synergy for the appearance and fast development of large number of ceramic systems with

superplastic capabilities. Several industrial processes in metal and polymer industries have already made use of these high ductile ceramics. The processing of dense ceramics includes sheet forming, blowing, stamping, forging and joining.

In order to be more close to metals two strategies have been used to enhance superplasticity: a) refinement of the microstructure and improvement of the accommodation process.

The refinement of the microstructure has been verified in nanomagnesia ceramics with a grain size of 37 nm, which could be deformed at temperatures as low as 700 ºC [51]. However, decreasing grain size is not always a good deal. In the case of YTZP, where there is segregation of Y atoms at the grain size and this grain size becomes few screening lengths (d≤ 100 nm, nanoscale length), the electric field can influence the diffusional processes and the creep Eq.(1) will be multiplied by a factor α [44]:

$$\alpha = \frac{1}{1+4\frac{\lambda}{d}\left[\exp\left(\frac{-z_D eV(R)}{3\varepsilon_r kT}\frac{\lambda}{d}\right)-1\right]} \quad (14)$$

with λ the Debye attenuation length, z_D the valence of yttrium, V(R) the electrical potential and ε_r the relative dielectric constant. Figure 6 represents α as a function of the grain size.

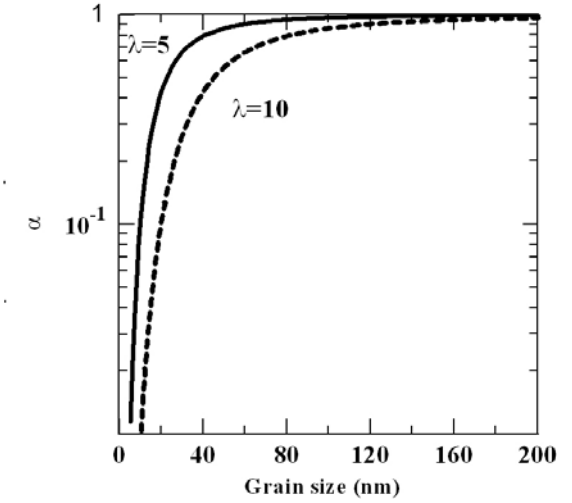

Figure 6: Plot of α versus grain size for two values of λ

The value of α can influence the mechanical behaviour of YTZP as shown in Figure 7, which represents the normalized stress as a function of grain size. It can be observed the nano-YTZP is harder than the sub-micrometer grain size ceramics [52].

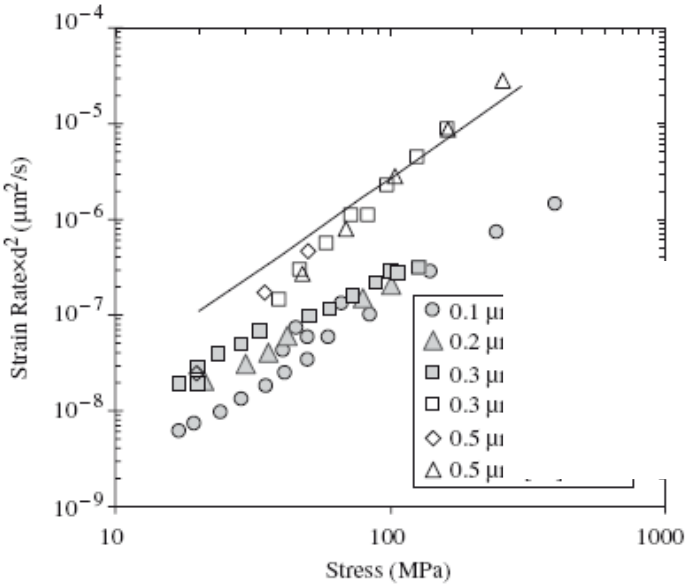

Figure 7: Normalized strain rate ($\dot{\varepsilon}d^2$) versus stress for different YTZP deformed at 1150 ºC. This figure has been taken from ref. 52

6-Future trends in the field.

Superplasticity is still a challenging field in which several regions are still partially explored or fully ignored. Several guidelines can be pointed out:

1- A systematic analysis of the role played by segregation to grain boundaries and the effect on electronic structure should be certainly performed.

2- The stress exponents and activation energies are not constant over the full range of stresses and temperatures in which superplasticity is found to occur. That dependence is the result of the complex topology of grain boundaries under grain boundary sliding. A more thorough analysis of the details of grain switiching should be taken into account.

3- In a near future, the main objective in ceramic superplasticity will be the search of the right conditions to reach "high strain rate superplasticity" (HSRS) ($\dot{\varepsilon} \geq 10^{-2} s^{-1}$) and superplasticity at low temperatures. At this point, a good control of the mechanisms for diffusion is mandatory, as displayed for the outstanding superplastic response of a extremely brittle material such as magnesium oxide.

4- The improvement of ceramic powder processing technology, the high purity ceramics of nano-meter scale routinely prepared and the new techniques for the processing of these powders such as hot isostatic processing, spark plasma sintering, microwave-assisted heating and so on will be the driving force for a very active study on nanoceramics in the next future, opening up probably new phenomena and new applications.

7-References

[1] G.D. Bengough, J. Inst. Metals, **7** (1912), 123

[2] R.C. Garvie, R.C. Hannink and R.T. Pascoe., Nature, 258, (1975), 703

[3] F. Wakai, S. Sakaguchi and Y. Matsuno, , Adv. Ceram. Mater.,1986, 1, 259-63.

[4] I-Wei Chen and L.A. Xue., J. Am. Ceram. Soc; 1990, 73, 2585-609.

[5] T.G. Nieh, J. Wadsworth and F. Wakai, Int. Mater. Rev.,1991, 36, 146-61.

[6] A.H. Chokshi", Mater. Sci. Eng.1993, A166, 119-33.

[7] T.G. Nieh, J. Wadsworth and O.D. Sherby, in "Superplasticity in metals and ceramics", Cambridge University Press (UK), 1997.

[8] M. Jimenez-Melendo, A. Dominguez-Rodriguez and A. Bravo-Leon, J. Am. Ceram. Soc;1998, 81, 2761-76 (1998).

[9] J.J. Melendez-Martinez and A. Domínguez-Rodríguez., Progress Mat. Sc; 2004, 49, 19-107.

[10] J.M. Albuquerque, M.P. Harmer and Y.T. Chou., Acta Mater. 49 (2001), 2277.

[11] A.M. Boullier and Y. Gueguen., Contrib. Mineral. Petrol. 50 (1975), 93-104

[12] S. Schmid, J.N. Boland and M.S. Peterson., Tectonophysics, 43, (1977), 257

[13] M. Jiménez-Melendo, A. Domínguez-Rodríguez, R. Marquez and J. Castaing., Phil. Mag. A 56, (1987), 767.

[14] T.G. Langdon., Metals Forum, 4 (1981), 14

[15] S. Ishihara, T. Tanizawa, K. Akashiro, N. Furushiro and S. Hori., Mater, Trans. JIM, 1999, 40, 1158. 1158-65.

[16] R. Duclos, J. Crampon and C. Carry, Phil. Mag. Letter, 2002, 82, 529-33.

[17] K. Morita and K. Hiraga, Scripta mater; 2003, 48, 1403-07.

[18] Duclos, R. J. Euro. Ceram. Soc. 24 (2004), 3103.

[19] Zelin, M. G. & Mukherjee, A. K. Mater. Sci. Eng. A208, 210-225 (1996).

[20] Muto, H. & Sakai, M. Acta Mater. 48, 4161-4167 (2000).

[21] Yasuda K, Okamoto T, Shiota T, Matsuo Y. Mat. Sc. Eng. A. 2006; 418: 115.

[22] Mukherjee, A. K. Mater. Sci. Eng. A322, 1-22 (2002).

[23] T.G. Nieh, J. Wadsworth and O.D. Sherby., "Superplasticity in Metals and Ceramics", Cambridge Univ. Press, 1997.

[24] Gómez-García, D., Lorenzo-Martín, C., Muñoz, A. & Domínguez-Rodríguez, A. Phil. Mag. 83, 93-108 (2003).

[25] W.A. Rachinger., J. Inst. Metals, 81, 33 (1952)

[26] M.F. Ahsby and R.A. Verrall., Acta metal; 1973, 21, 149-63.

[27] J.R. Spingarn and W.D. Nix, Acta metal; 1978, 26, 1389-98.

[28] A. Dominguez-Rodriguez, A. Bravo-Leon, J.D. Ye and M. Jiménez-Melendo., Mater. Sci. Eng; 1998, A247, 97-101

[29] Morita, K. and Hiraga, K., Scrip. Mater. 48, (2003), 1403

[30] Zapata-Solvas E, Gomez-Garcıa D, Garcıa-Gañan C, Domınguez-Rodrıguez A. J. Europ. Ceram. Soc. 2007; 27: 3325.

[31] E. Arzt, M.F. Ashby and R.A. Verrall., Acta metal. 31, 1977 (1983).

[32] M. Jimenez-Melendo and A. Dominguez-Rodriguez.,, Acta mater; 2000, 48, 3201-10.

[33] M. Jimenez-Melendo and A. Dominguez-Rodriguez., Phil. Mag; 1999, A 79, 1591-608.

[34] K. Morita and K. Hiraga, Acta mater; 2002, 50, 1075-85.

[35] Morita, K. and Hiraga, K., Phil. Mag. Lett., 81, (2001), 311-319.

[36] A. Muñoz, D. Gomez-Garcia, A. Domínguez-Rodriguez and F. Wakai., J. Europ. Ceram. Soc., 2002, 22, 2609-13.

[37] Theunissen, G.S.A.M., Winnubst, A.J.A. and Burggraaaf, A.J., J. Mater. Sci. 27, (1992), 5057.

[38] C. Xu, Ceram. Int. 31 (2005) 537-542.

[39] Stemmer, S.., Vleugels, J. and Van der Biest, O., J. Europ. Ceram. Soc. 18, (1998), 1565.

[40] J. Hines, Y. Ikuhara, A. Chokshi and T. Sakuma: Acta mater. 46 (1998) p. 5557

[41] P. Flewit and R. Wild: Grain boundaries: Their microstructure and chemistry (John Wiley&Sons Ltd. Chichester, UK, 2001), p. 137.

[42] X. Guo and Z. Zhang., Acta Mater. 51, (2003), 2539-47

[43] R.W. Cahn abd P. Haasen., "Physical Metallurgy, Part I (Amsterdam: North-Holland), (1983), pp. 875-880.

[44] D. Gómez-García, C. Lorenzo-Martín, A. Muñoz-Bernabé, and A. Domíguez-Rodríguez, Phys. Rev. B. 67 [14], 144101 (2003).

[45] A. Domínguez-Rodríguez, D. Gómez-García, C. Lorenzo-Martín, and A. Muñoz-Bernabé, J. Eur. Ceram. Soc., 23, (2003) 2969-2973.

[46] R. Raj and C.K. Chung, Acta metal; 1981, 29, 159-66.

[47] A. Domínguez-Ridríguez, K.P.D. Lagerlof and A.H. Heuer., J. Amer. Ceram. Soc., 69, (1986), 281.

[48] F. Wakai, Acta mater. 1994, 42, 1163-72.

[49] J. J. Meléndez-Martínez, D. Gómez-García and A. Domínguez-Rodríguez, Phil. Mag. Vol. 84, nº22, 2305-16 (2004).

[50] D. Gómez-García, E.Zapata-Solvas, A. Domínguez-Rodríguez and L. P. Kubin, Phys. Rev. B 80, 214107 (2009).

[51] A. Domínguez-Rodríguez, D. Gómez-García, E. Zapata-Solvas, J. Z. Chen and R. Chaim, Scripta mater. 56 nº2, 89-91 (2007).

[52] Gutierrez-Mora F, Gómez-García D, Jimenez-Melendo M, Domínguez-Rodriguez A, Chaim R. J.Amer. Ceram. Soc. 2005; 88: 1529.

International Symposium on Plastic Deformation and Texture Analysis
Alcoy (Spain) 24-25 September 2012
63-71

Plastic deformation and low temperature degradation of 3Y-TZP

J.A. Muñoz Tabares[1], E. Jiménez-Piqué[1], J. Reyes Gasca[2] and M. Anglada[1]

[1]Departament de Ciència dels Materials i Enginyeria Metal·lúrgica, Universitat Politècnica de Catalunya, Avda. Diagonal 647 (ETSEIB), 08028 Barcelona, Spain
[2]Instituto de Física, Universidad Nacional Autónoma de México, Circuito de la Investigación Científica s/n, Cd Universitaria, 04510 México DF, México,

Abstract

It is shown that grinding increases hydrothermal degradation resistance of tetragonal polycrystalline zirconia doped with 3 mol% yttria (3Y-TZP). This is explained in terms of the formation of a very thin layer of recrystallised and textured nano-size grains, which prevents the formation of monoclinic variants. In addition, by annealing at 1200 °C during 1 hour after grinding, the usual microstructure of as-sintered material is recovered, but the material is still resistance to degradation. This increased resistance to hydrothermal degradation of ground plus annealed 3Y-TZP with respect to the as sintered condition is related to the crystallographic texture developed after grinding, as measured by the $I_t^{(002)}/I_t^{(200)}$ ratio.

Resumen

Se pone de manifiesto que el desbaste plano aumenta la resistencia a la degradación hidrotérmica de la circona tetragonal dopada con 3% molar de itria (3Y-TZP). Esto se explica en términos de la formación de una capa superficial muy delgada formada por nanogranos con textura, lo cual impide la nucleación de variantes monoclínicas. Además mediante el recocido a 1200 °C durante una hora después del desbaste, se recupera la microestructura usual del material sinterizado pero el material es todavía resistente a la degradación lo cual está relacionado a la textura cristalográfica formada, la cual se cuantifica mediante el cociente $I_t^{(002)}/I_t^{(200)}$.

Keywords: Hydrothermal degradation, tetragonal polycrystalline zirconia doped with 3 mol% yttria, grinding, surface damage, annealing and recrystalisation.

Palabras clave: Degradación hidrotérmica, circona policristalina dopada con 3% molar de itria, desbaste, daño superficial, recocido y recristalización.

1. Introduction

The good combination of strength and toughness of yttria stabilized tetragonal polycrystalline zirconia (3Y-TZP), as well as its biocompatibility and wear resistance, have allowed its implementation in a wide range of structural applications. Its relatively high fracture toughness is related to the stress-induced transformation of the metastable tetragonal phase to monoclinic phase (referred as t–m transformation).[1]

During final shaping and surface finishing of ceramic devices, different types of machining processes (cutting, grinding, polishing, diamond drilling, sandblasting, CAD/CAM machining, etc.) are required. All these processes induce different types of damage, as phase transformation, plastic deformation or cracks that may also affect the structural integrity of these devices.[2,3]

In addition 3Y-TZP also suffers a spontaneous t–m phase transformation at the surface when it is exposed to humid environments. This phenomenon, referred to as hydrothermal degradation or low temperature degradation, results in the loss of mechanical properties of the surface because of the formation of intergranular microcracks as a result of t-m transformation.[4,5]

In particular, the damage induced by machining during grinding and by hydrothermal degradation in service is critical for the manufacture and long term reliability of pieces and components made of 3Y-TZP. There is an increase on the resistance to hydrothermal degradation of 3Y-TZP by grinding which is usually attributed to the appearance of grinding compressive residual stresses in the surface. [6–9]

It is obvious than the exact microstructure induced by grinding on the surface should play an important role on the resistance to hydrothermal degradation. Recently we have studied separately the changes in microstructure that takes place in 3Y-TZP during hydrothermal degradation[10] and grinding[11] by using transmission electron microscopy (TEM) on thin foils extracted from the

surface by focus ion beam (FIB). Our aim in the present paper is to explore the idea that the resistance to hydrothermal degradation of ground specimens could be also explained in terms of the plastic deformation, recrytallisation and texture induced during grinding. The reader is referred to [12] for a more extensive account of the present study.

2. Experimental Method

2.1. Material processing

Samples were produced from zirconia powder stabilized with 3% molar of yttria (TZ-3YSB-E, Tosoh, Tokyo, Japan) by cold isostatic pressing and sintering, as described previously [10]. An annealing treatment was performed at 1200 ºC for 2h in order to relax the residual stress caused by surface preparation. The resulting samples denoted "AS" (as sintered) had a grain size of 0.34 ± 0.02 μm and a density of 6.03 ± 0.01 g/cm^3.

2.2 Surface treatments

The samples were ground using a diamond grinding disc (MD-Piano 220 Struers) under a pressure of 0.9 MPa with a constant grinding speed of 3.6 m/s and water cooling. These samples were divided into two sets, the first one corresponds to samples ground as previously described and are denoted as ASgr (AS ground). The second set will be denoted as ASgr/ann (AS ground and annealed) and was composed of specimens annealed at 1200 ºC after grinding, during different periods of time, with the aim of removing the changes of microstructure during grinding.

Finally, the two sets of samples were hydrothermally degraded in an autoclave in the presence of water steam at 131ºC and 0.2 MPa of pressure during 96 hours. This long time was chosen with the aim of comparing with AS specimen, which we had studied before under these hydrothermal degradation conditions [10].

2.3 Surface microstructure

The crystallographic phases were identified by X-ray diffraction (XRD) and μ-Raman spectroscopy as explained in more detail in [12]. The topography of the samples was observed in contact mode in an Atomic Force Microscope (AFM)

of Digital Instruments. The images were treated using WSxM software. To observe the in depth microstructure by Scanning Electron Microscopy (SEM), a sample of ASgr/ann was milled by FIB in a Dual BeamTM Workstation model FEI Strata DB 235.

3. Results and discussion

The XRD spectrum obtained from ASgr degraded during 96 hours was similar to that before exposure to water vapour, (see Fig. 5 from reference [10]). This spectrum shows the changes previously reported: asymmetric broadening of the (111) tetragonal peak at ~30º (2θ), inversion of the peaks intensity at 34.64° and 35.22° (2θ) corresponding, respectively, to the planes (002) and (200) of the tetragonal phase and, finally, the presence of a small volume fraction of monoclinic phase (~10%), which is equal to that already present in the ground specimens. It is therefore quite clear that the conditions used here for hydrothermal degradation do not produce any additional increase in monoclinic volume fraction besides that present in the ground material.

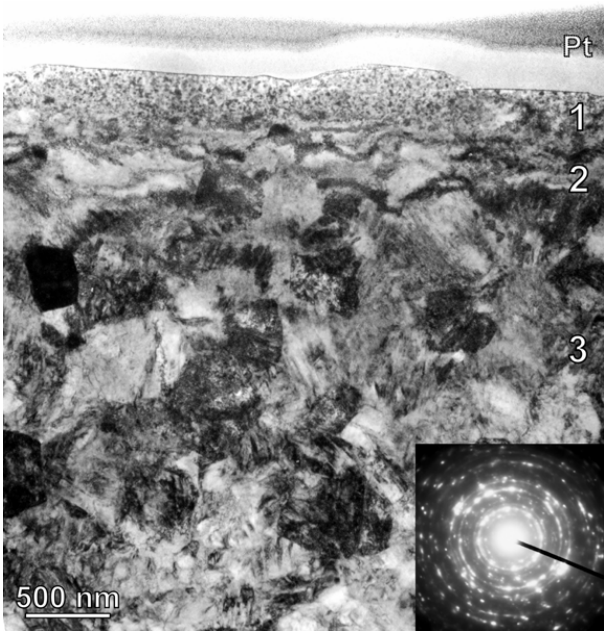

Figure 1. Subsurface microstructure of ground sample: 1) fine microstructure with grains of ≈20 nm diameter; 2) microstructure with deformed grains; 3) equiaxed grains with martensite plates.

This was confirmed by obtaining the monoclinic profile by μ-Raman spectroscopy on the cross section of an ASgr degraded sample and compared with the profile obtained from an ASgr sample without degradation (see reference [12] for more details). Therefore, the lack of hydrothermal degradation in ground 3Y-TZP should be related to the severe microstructural changes induced in the surface: phase transformation, plastic deformation, recrystallisation, as well as the presence of significant compressive residual stresses (see Figure 1).

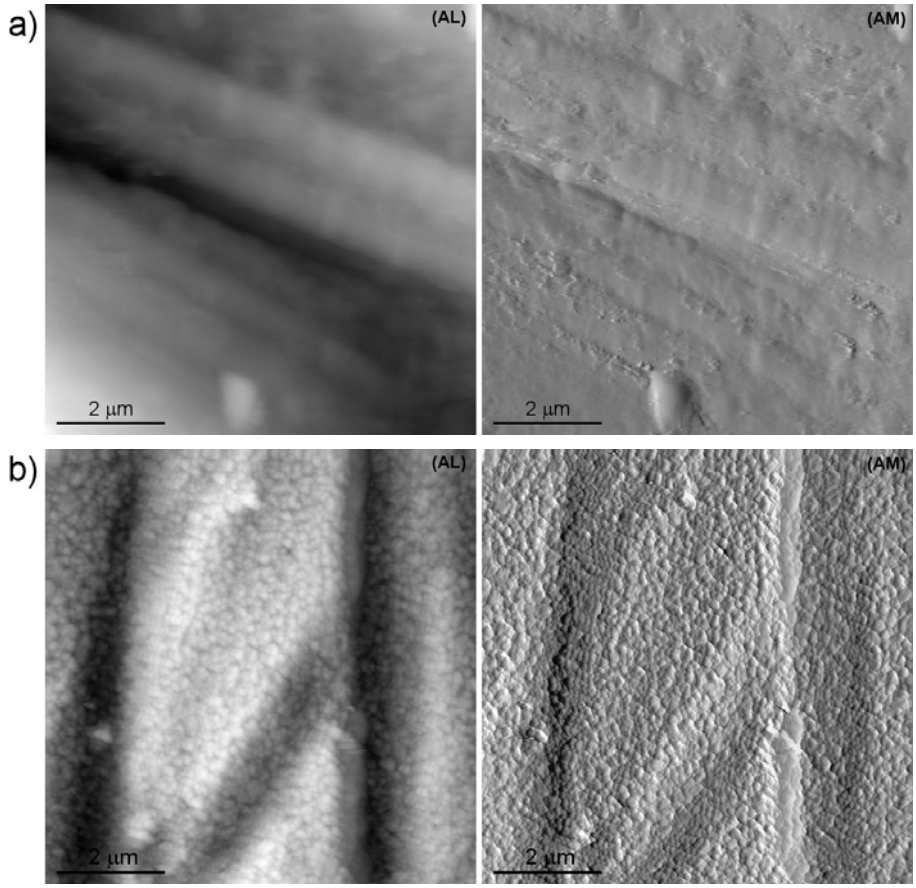

Figure 2. AFM images (8x8 □m) in height (AL) and in amplitude modes (AM) of: a) Ground AS specimen; b) AS ground specimen annealed at 1200ºC for 1 hour.

Fig. 2 shows 1x1 μm AFM images from the surface of samples subjected to grinding and annealing. In these images the labels (HE) and (AM) refer to

height (topography) and amplitude channels, respectively. In figure 2a, the topography of the ASgr sample is characteristic of machined surfaces with grinding grooves and irregular edges. In this case the specimen was not heat treated to reveal the grain size, since the aim was to show the as ground microstructure avoiding changes that could be induced by heat treatment.

This specimen was observed by TEM and it was shown[11] that there is a very thin surface layer of recrystallised grains of about 10-20 nm in diameter, which grow after 1 minute at 1200 ºC into equiaxed grains with an average grain size of 30 $\pm$ 9 nm. Finally after 1 hour annealing, a size of 284 $\pm$ 30 nm is reached which is close to the grain size of the AS material.

A cross-section prepared by FIB in ASgr /ann (1h) was analysed with the objective to find out the near surface in-depth microstructure. It could be appreciated that the different layers observed in the ground sample [12] have all disappeared leaving behind a homogeneous microstructure with equiaxed grains of ~300 nm, just below the surface.

In the XRD spectrum of ASgr/annealed for 1 hour, the monoclinic phase produced by grinding has completely disappeared, as evidenced by the absence of the monoclinic peak at 28.2º (2θ) (see Fig 6b in [12]). Residual stresses are also removed by annealing, as can be appreciated the changes in mechanical properties. Thus, the strength, which increased after grinding with respect to as-sintered material, recovers in Asgr/ann (1 hour) the original strength of AS (see Fig. 2 in Ref. [11]). In addition, when a 150 N Vickers indentation is made on this sample the indentation cracks lengths, which are shorter in ASgr with respect to AS, become of similar length as in AS [11].

The asymmetric broadening of the tetragonal peak at 30° (2θ) also disappears during annealing. However, it is interesting to notice that the inversion of the intensity of the peaks at 34.64° and 35.22° (2θ), which correspond to the planes (002) and (200) of the tetragonal phase, persists after annealing. The $I_t^{(002)}/I_t^{(200)}$ intensity ratio for AS is 0.77 and it changes to 1.72 for ASgr. But, in Asgr/ann specimens (1 hour annealing) the inversion of the intensity of the peaks remains. This indicates that this crystallographic texture in Asgr/ann is stronger close to the surface, that is, in the region in which strong microstructural changes take place during grinding and annealing.

The degradation test (96 hours at 131ºC) was performed in a ground sample after annealing for 1hour, since after this time the microstructure had been

largely recovered. No t-m transformation took place during hydrothermal degradation despite the prolonged duration of the hydrothermal treatment (96 hours). In addition, measurements were made by μ-Raman spectroscopy did not detect any monoclinic phase [12].

Since microstructural changes, as well as the residual stresses were removed by annealing for 1 hour at 1200 °C, the only difference left was the above mentioned inversion of the intensity, that is, the increase in the intensity of the (002) tetragonal peak with respect to (200). Therefore, the different hydrothermal degradation resistance of the ASgr/ann samples could be related to the presence of crystallographic texture in a layer close to the surface.

For ASgr, the resistance to hydrothermal degradation is possibly related to the existence of a very thin layer of tetragonal recrystallised nano-grains (10-20 nm) whose size are smaller than the critical size for transformation in humid environment [13,14]. Another possible reason for the high degradation resistance of ASgr is the contribution of residual grinding compressive stresses, which will act making more difficult the nucleation of the monoclinic phase because of the expansion associated to the t-m transformation. Although the surface residual compressive stresses are contributing to the higher resistance to degradation, the only presence of recrystallised nano-grains on the surface of ASgr is capable of explaining this effect. Even if water species may diffuse in the nanograin layer, their small size prevents the formation of a martensite nucleous. At higher depth, in the highly deformed layer and in the partly transformed layer by grinding, t-m transformation activated by water species did not take place either, because the sequence transformation/ microcracking/transformation that begins at the surface [10], is inhibited by this layer of nano-grains.

On the other hand, one important effect of annealing on the microstructure of the ground sample is to reverse the ground microstructure to the tetragonal phase free from plastic deformation and residual stresses. In particular, the small amount of monoclinic volume fraction is removed by the m-t phase transformation, which begins at ~600 °C for 3Y-TZP.[15,16] This reverse transformation, together with the relaxation of compressive residual stress is manifested by the recovery of the surface mechanical properties (Fig. 2 in Ref [11] and Fig. 7). In addition, during annealing there is tetragonal surface grain growth because of the extremely small size of the grain in the recrystallised surface layer after grinding. In the case of ASgr/ann during 1 and 10 minutes, the grain growth is limited and the microstructure obtained has nano-grains

whose sizes are still smaller than the critical size for transformation in humid environment. So the resistance to hydrothermal degradation in these samples at the surface can still be explained in terms of the surface layer of tetragonal recrystallised nano-grains.

4. Conclusions

1) Ground 3Y-TZP does not suffer hydrothermal degradation in autoclave after 96 hours at 131°C, even if the specimens are annealed for short times at 1200 °C. The mechanism responsible for that is the formation by recrystallisation of a very thin surface layer of tetragonal nano-grains from the highly deformed surface. This layer is already present after grinding and its grain size increases during annealing.

2) An annealing treatment at 1200°C during 1 hour after grinding recovers the typical microstructure (phase and grain size) of the as sintered zirconia. However, the texture of the tetragonal phase that appears during grinding is still present and it is also resistant to hydrothermal degradation (131 °C/96h), which is attributed to the level of texture represented by the $I_t^{(002)} / I_t^{(200)}$ ratio.

5. Bibliography

[1] R.C.Garvie, R.H. Hannink, and R.T. Pascoe, *Nature*, 258 (1975) 703.

[2] H. Kao, F. Ho, C. Yang, W. Wei, *J Eur Ceram Soc*, 20 (2000) 2447.

[3] A. Juy, M. Anglada, *Eng Fail Anal*, 16 (2009) 2586.

[4] K. Kobayashi, H. Kuwajima, T. Masaki, *Solid State Ion,* 3-4 (1980) 489.

[5] S. Lawson, *J Eur Ceram Soc*, 15 (1995) 485.

[6] T. Sato, T. Besshi, Y. Tada, *Wear* 1194 (1996) 204–11.

[7] S. Wada, K. Yokoyama, *J Ceram Soc Jpn*, 107 (1999) 92–5.

[8] T. Kosmac, C. Oblak, L. Marion, *J Eur Ceram Soc* 28 (2008) 1085–90.

[9] S. Deville, J. Chevalier, L. Gremillard, *Biomaterials*, 27 (2006) 2186–92.

[10] J. A. Muñoz-Tabares, E. Jiménez-Piqué, M. Anglada, *Acta Mater,* 59 (2011)473–84.

[11] J.A. Muñoz-Tabares, E. Jiménez-Piqué, J. Reyes-Gasga, M. Anglada, , *Acta Mater*, 59 (2011) 6670-83.

[12] J.A. Muñoz-Tabares, M. Anglada, J Eur Ceram Soc, 32 (2012), 325-33.

[13] A. G. Evans, N. Burlingame, M. Drory, W. M. Kriven, *Acta Metall*, 29 (1981)447–56.

[14] F.F. Lange, *J Mater Sci*, 17 (1982) 225–34.

[15] S. Shukla, S. Seal, *Int Mater Rev*, 50(2005) 45–64.

[16] O. Fabrichnaya, F. Aldinger, *Int J Mater Res*, 95 (2004) 27–39.

6. Acknowledgments

This work was supported by Ministerio de Ciencia e Innovación of Spain through Project MAT2008-03398 and by the Generalitat de Catalunya (2009SGR01285). The authors are grateful to F. Marro and C. Botero for their assistance during AFM images acquire.

International Symposium on Plastic Deformation and Texture Analysis
Alcoy (Spain) 24-25 September 2012
73-81

High temperature deformation and damage of magnesium alloys

P. Lhuissier[1], L. Salvo[1], E. Boller[2], J.J. Blandin[1]

[1]Université de Grenoble / CNRS, SIMAP laboratory, Grenoble INP, UJF, 38402 Saint-Martin d'Hères, France

[2]European Synchrotron Facility (ESRF), Grenoble France

Abstract

A way to overcome the poor deformability of magnesium alloys at room temperature is to increase the temperature of forming. When temperature is increased the stress exponent n decreases and in some cases superplastic properties can be developed. The n value is known to be a key parameter in the control of plastic stability but low n values are not enough to ensure large capacity of deformation since fracture can also result from strain induced cavitation. Damage data can also give information on the deformation mechanisms, in particular when 3D imaging is performed. X-ray micro tomography provides 3D information and thanks to particularly short acquisition times, strain induced damage can now be investigated in *in situ* conditions providing unique opportunities for investigating nucleation, growth and coalescence of cavities. In the present work, the deformability of wrought magnesium alloys has been investigated with a particular attention given to both high temperature deformation and damage mechanisms.

Resumen

Una manera de mejorar la mala deformabilidad de las aleaciones de magnesio a temperatura ambiente es aumentar la temperatura de la conformación. Cuando la temperatura aumenta, el exponente n de la tensión disminuye y, en algunos casos, se desarrollan propiedades superplásticas. El valor de n es conocido por ser un parámetro clave en el control de la estabilidad plástica, pero bajos valores de n no son suficientes para garantizar una gran capacidad de deformación a fractura que también puede resultar en cavitación inducida

por deformación. Los datos del daño también puede proporcionar información sobre los mecanismos de deformación, en particular cuando se obtienen imágenes en 3D. La microtomografía de rayos X proporciona información 3D y, gracias a tiempos de adquisición especialmente más cortos, del daño inducido por deformación por lo que ahora se puede investigar en condiciones in situ ofreciendo oportunidades únicas para la investigación de la nucleación, crecimiento y coalescencia de cavidades. En el presente trabajo, se ha investigado la deformabilidad de las aleaciones de magnesio forjado con especial atención a la deformación a elevadas temperaturas y a los mecanismos de daño.

Keywords: magnesium alloys, high temperature deformation, damage, microtomography.

Palabras clave: Aleaciones de magnesio, deformación a elevada temperatura, daño, microtomografía.

1. Introduction

Magnesium alloys have limited formability at room temperature due to their hexagonal close packed structure and a way to overcome this difficulty is to deform them at high temperature for which the difference between critical resolved shear stresses for pyramidal or prismatic slips and the basal one is strongly reduced.

High temperature deformation of metallic alloys can generally be described by:

$$\dot{\varepsilon} = KD_{eff}\left(\frac{b}{d}\right)^{p}\left(\frac{\sigma}{G}\right)^{n} \quad (1)$$

with $\dot{\varepsilon}$ the strain rate, σ the flow stress, D_{eff} an effective diffusion coefficient, b the Burgers vector, G the shear modulus, d the grain size, n the stress exponent and p the grain size exponent. It is well known that the n value gives information about the predominant mechanism of deformation. For diffusion creep n = 1.0 whereas n is frequently close to 2 for grain boundary sliding (i.e. superplastic regime), both mechanisms being promoted by grain refinement, the value of p varying from 2 when lattice diffusion is controlling or 3 when grain boundary diffusion is controlling. When dislocation movement is dominant, n is generally between 3 and 5 and the sensitivity to grain size is

very limited ($p << 1$). Dislocation movement involves both glide and climb of dislocations and the slowest between these two mechanisms is expected to control deformation. Climb is controlling and values of n close to 5 are generally measured in pure metals whereas in the case of alloys, dislocation glide can also be the controlling mechanism, for instance due a solute drag effect and in this case, $n \approx 3$ [1]. Such rhelogies have been reported for instance in the case of Al-Mg alloys and attributed to the strong interaction between solutes and dislocations [2,3].

Knowing that plastic stability (i.e. necking resistance) is promoted by low values of the stress exponent, the capacity to get a n value close to 3 instead of 5 (viscous glide as the controlling mechanism vs. dislocation climb) is interesting in terms of forming capacity. Nevertheless, even if a low n value is a required condition to promote plastic stability, it is not a sufficient to assure large deformability since strain may induce damage. It has been established that magnesium alloys can be sensitive to strain induced damage when they are deformed at high temperature, fracture occurring by a combination of necking effect and coalescence of cavities or cracks through the sample. A change in deformation mechanisms can also result in variations of the shapes of the cavities: in the case of intragranular deformation of the grains, cavities elongated along the stress direction are usually observed whereas cavities with complex shapes frequently develop when grain boundary sliding predominates. This means that data about the damage behaviour can also give interesting information concerning the activated mechanisms of deformation.

In the recent past, X-ray micro-tomography providing 3D images of the bulk of materials has demonstrated its efficiency to study damage at high temperature [4, 5]. From reconstructed 3D volumes, many parameters can be quantified like the cavity volume fraction, the volume of each cavity, the number of cavities in a given volume or the sphericity of the cavities. Tomography analyses are usually performed in *post mortem* conditions meaning that samples are deformed, possibly at high temperature and then are characterised at room temperature after deformation at a given strain. However, such *post mortem* characterization can induce artifacts linked for instance to the cooling procedure and result also in a difficulty to follow a given population of cavities with increasing strain. To overcome such difficulties, *in situ* X-ray micro tomography can be used (i.e. analysis carried out directly during the mechanical test) but it requires acquisition times for getting an image compatible with the kinetics of the studied phenomena. In the case

of strain induced cavitation associated with strain rates typically larger than 10^{-4} s^{-1} as it is the case in this work, acquisition time must be significantly lower than 1 minute. Such acquisition times are now achievable in the European Synchrotron Radiation Facility (ESRF, Grenoble).

In the present study dedicated to magnesium alloys, the effect of grain size on the high temperature mechanical behaviour is investigated and strain induced damage is characterised thanks to X-ray micro tomography used in *in situ* conditions.

2. Experiments

Two alloys are considered: a WE43 alloy (Mg-4Y-2Nd-1RE, wt. %) with an initial grain size close to 50 microns and an AZ31 alloy (Mg-3Al-1Zn, wt. %) with a mean grain size of about 12 microns [6,7]. For studying the effect of grain size on the mechanical response at high temperature, the WE43 alloy was heat treated for 48h at 450°C, 8h at 500°C and 18h at 500°C. The resulting grain sizes were measured after treatment and values respectively close to 50, 80 and 150 microns were obtained. Optical micrographs of the microstructures after 48h @ 450°C and 18h @ 500°C are shown in figure 1.

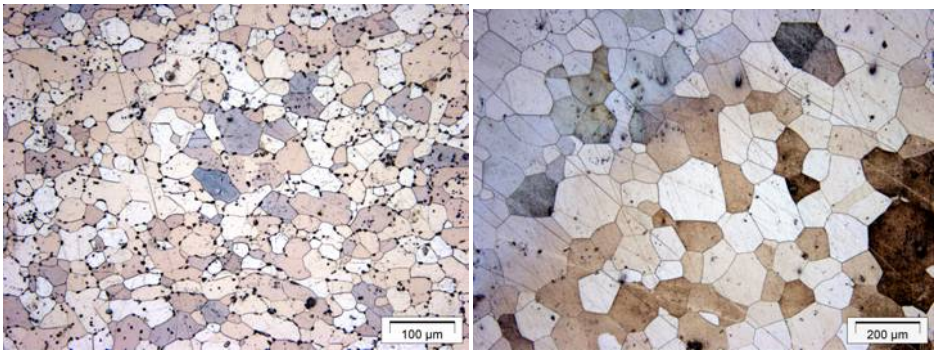

Figure 1, Optical micrographs of the microstructure of the WE43 alloy after thermal treatments, a. 48 h @ 450°C, b. 18 h @ 500°C (sheet plane)

High temperature deformation was preferentially investigated at 400°C and both strain rate jump tests and tests at constant strain rates were performed. Strain induced damage was investigated thanks to X-ray micro tomography analyses performed at the ESRF allowing a resolution of about 1 µm and time needed to get a complete acquisition typically less than 15 seconds.

3. High temperature mechanical behavior

From strain rate jump tests, the sensitivity at 400°C of the flow stress with the applied strain rate was evaluated for the three heat treated WE43 microstructures. In the investigated strain rate interval, very limited strain softening or hardening were detected for a given strain rate, leading to the capacity of drawing directly (σ, $\dot{\varepsilon}$) curves. Figure 2 displays these curves. Two main conclusions can be drawn from this figure: firstly, a stress exponent close to 3 is measured in the whole studied strain rate interval whatever the grain size; secondly, for a given strain rate, the sensitivity of the flow stress to the grain size appears very limited. As already mentioned, a value of n close to 3 in such a relatively large strain rate interval supports the idea of a deformation controlled by a solute drag effect. In the case of the WE43, solute drag can be reasonably considered due to the important amount of solutes diffusing slowly. When viscous glide controls deformation, significant strains to fracture (i.e. elongations to fracture typically larger than 200 %) can be often achieved, which has been for instance the case in the present investigation for microstructure displaying the grain size of 150 microns when deformed at $6x10^{-4}$ s^{-1}.

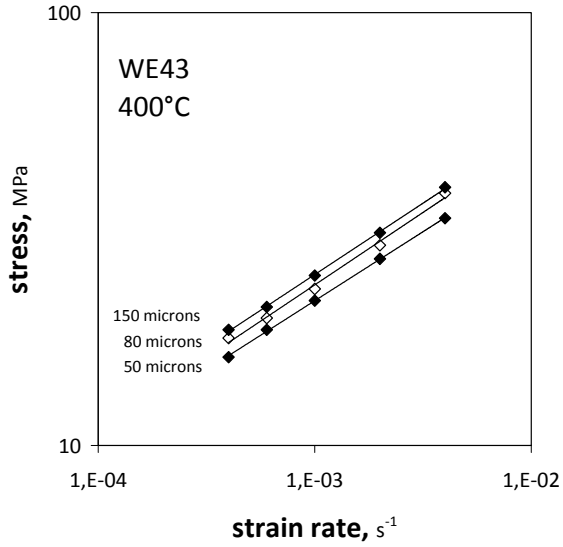

Figure 2. Effect of grain size on the ((σ, $\dot{\varepsilon}$) curves for the WE43 alloy deformed at 400°C

Considering a constant value of the stress exponent n in the studied strain rate interval, the grain size exponent p can be deduced from equation (1) according to $p = n \ln(\sigma_2/\sigma_1)/\ln(d_2/d_1)$. From figure 2, values of p less than 0.5 are measured, confirming that mechanisms of deformation sensitive to grain size like grain boundary sliding or diffusion creep, if present, play only a very marginal role in the deformation of this alloy.

4. Damage behavior

Figure 3 displays X-ray micro tomography observations obtained in conventional *post mortem* conditions of the cavities formed in the two investigated alloys (i.e. AZ31 and WE43) deformed up to fracture at 400°C. In this case, the WE43 alloy was deformed in as-provided conditions. For this alloy, elongated cavities are observed confirming that intragranular deformation is controlling deformation. For the studied AZ31 alloy the conditions of deformation correspond to the superplastic regime [6] and complex shapes of cavities are observed, pointing out the dominant role played by grain boundary sliding in this domain and suggesting that fracture results at least partially from cavity coalescence.

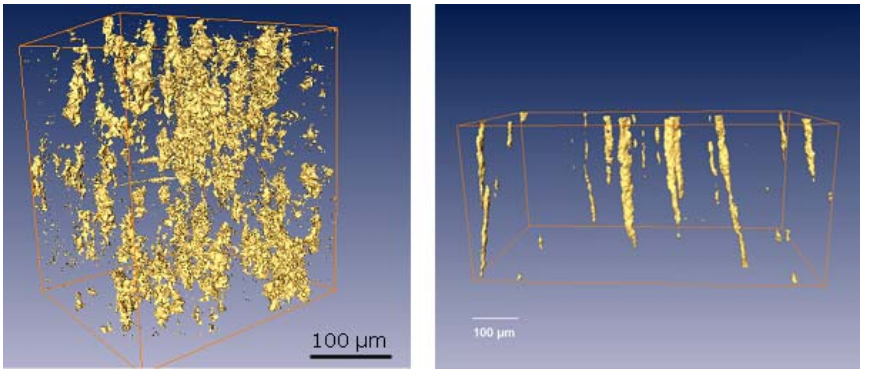

(a) (b)

Figure 3. 3D imaging of the population of cavities after deformation at 400°C and 6x10-4 s-1 (stress axis is vertical) , a) AZ31 deformed up to $\varepsilon \approx 1.3$, b) WE43 deformed up to $\varepsilon \approx 1.0$.

Figure 4 displays *in situ* 3D imaging of a given volume as far as strain is increased. Four macroscopic strains have been selected, respectively equal to 0.00, 0.44, 0.75 and 1.10. These images suggest that continuous nucleation

occurs with increasing strains. It also shows that after significant strain, necking can develop. Finally, it also supports the idea that coalescence between cavities can be also play an important role in damage development. For ε = 1.10, cavities with sizes larger than 100 microns can be detected, associated with complex shapes even if a preferential elongation along the stress axis can be observed.

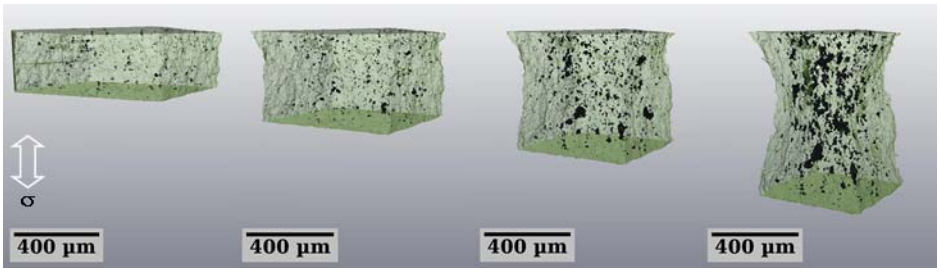

Figure 4. 3D imaging of damage growth during deformation of the alloy (strains are respectively 0.00, 0.44, 0.75 and 1.10)

Figure 5 shows 3D observations of the population of cavities for two strains: $\varepsilon \approx 0.13$ and $\varepsilon \approx 0.35$. An increase of the number of cavities is clearly detected and such increase was detected in the whole strain interval. Nevertheless, the interpretation of this variation is not straightforward since it can result from both strain induced nucleation of cavities and the first steps of cavity growth since only cavities of which the volume is larger than about 10 μm^3 were considered here.

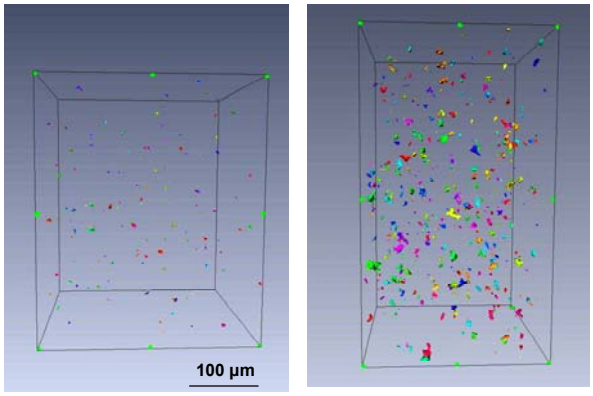

Figure 5. 3D views of the population of cavities after strains of 0.13 and 0.35 (AZ31, 400°C, $5x10^{-4}$ s^{-1}, *in situ* X ray micro tomography experiments, only cavities with volumes larger than about 10 μm^3 are considered)

Figure 6 displays 3D imaging of the growth of cavities between macroscopic strains of 0.16 and 1.03. Coalescence events are clearly detected between 0.44 and 0.52 and between 0.74 and 0.89 respectively. A third small coalescence event can even be observed between 0.89 and 1.03.

Additional work is under progress to study the effects of such coalescence events on the damage kinetics. The criterion for cavity coalescence (e.g. the critical distance between two cavities under which coalescence occurs) is also under investigation.

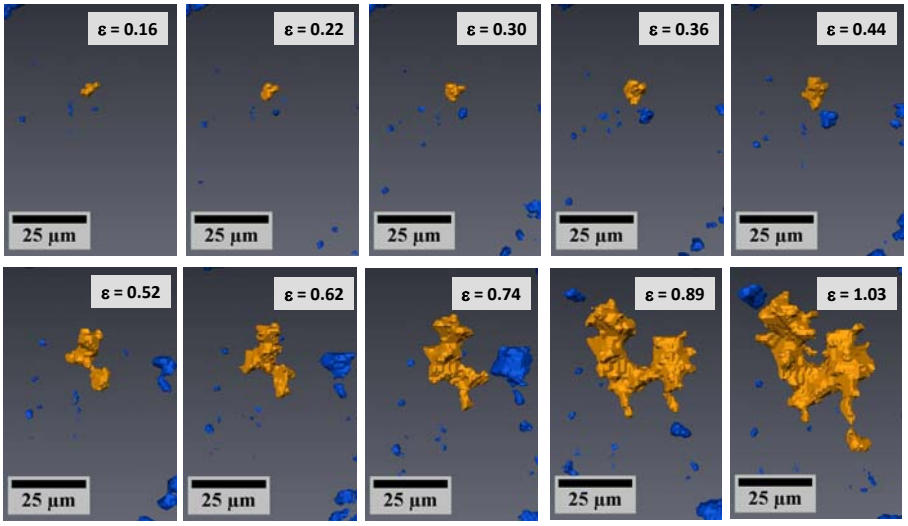

Figure 6. 3D imaging of a cavity growth involving coalescence steps (stress axis is vertical)

5. Conclusions

The deformability at 400°C of two wrought magnesium alloys has been investigated. In the case of the studied WE43 alloy, microstructures with various grain sizes (from 50 µm to 150 µm) were produced and both stress exponent and grain size exponent were measured. These exponents ($n \approx 3$ and $p << 1$) support the idea of a deformation controlled by viscous glide of dislocations. Strain induced damage during high temperature tensile deformation of an AZ31 alloy was studied by *in situ* X ray micro tomography. Despite significant values of the applied strain rate ($> 10^{-4}$ s^{-1}), it was possible to obtain good images of the cavities thanks to particularly low acquisition times. In the investigated conditions, strain induces cavity nucleation and

thanks to such conditions of analyses which provides the capacity to follow each cavity during deformation, cavity growth with or without coalescence events can be clearly distinguished.

6. References

[1] E.M. TALEFF, W.P. GREEN, M.A. KULAS, T.R. MCNELLEY, P.E. KRAJEWSKI, *Mater. Sc. Eng.*, A410-411 (2005) 32.

[2] M.A. KULAS, W.P. GREEN, E.M. TALEFF, P.E. KRAJEWSKI, T.R. MCNELLEY, *Metall. Mater. Trans*., 37A (2006) 645.

[3] T.R. MCNELLEY, K. OH-ISHI, A.P. ZHILYAEV, S. SWAMINATHAN, P.E. KRAJEWSKI, E.M. TALEFF., *Metall. Mater. Trans*., 39A (2008) 50.

[4] C.F. MARTIN, C. JOSSEROND, L. SALVO, J.J. BLANDIN, P. CLOETENS, E. BOLLER, *Scripta Mater*., 42 (2000) 375.

[5] L. SALVO, P. CLOETENS, E. MAIRE, S. ZABLER, J.J. BLANDIN, J.Y. BUFFIÈRE, W. LUDWIG, E. BOLLER, D. BELLET, C. JOSSEROND, *Nuclear Inst. Meth. Phys. Res. B*, 200 (2003) 273.

[6] R. BOISSIÈRE, J.J. BLANDIN, *7th International Conference on Magnesium Alloys and their Applications* (6-9 Nov. 2006, Dresden), 6-9 Nov. 2006 (Dresden, D), Ed. K.U. Kainer, Wiley Publisher, DGM, 393.

[7] J.J. BLANDIN, *Mater. Sc. Forum*, 551-552 (2007) 211.

International Symposium on Plastic Deformation and Texture Analysis
Alcoy (Spain) 24-25 September 2012
83-103

Microstructural evolution and mechanical properties of Al 7075 alloy processed by severe plastic deformation

F. Carreño, P. Hidalgo-Manrique, J.M. García-Infanta, C.M. Cepeda-Jiménez, A. Orozco-Caballero, O.A. Ruano

Department of Physical Metallurgy, CENIM-CSIC, Av. Gregorio del Amo 8, Madrid 28040, Spain

Abstract

This research work considers different aspects influencing the progressive refining and misorientation increase of the aerospace aluminium alloy 7075 (Al-Zn-Mg-Cu) processed by severe plastic deformation methods, such as ECAP, ARB, HPT and FSP, as well as the effect on the mechanical properties, especially at intermediate to high temperatures. ECAP processing shows that the final (sub)grain size is best predicted by applied stress than by accumulated strain. ARB processing shows that progressive refining with increasing misorientation is obtained in conditions prevailing recovery rather than discontinuous recrystallization processes. FSP and HPT, which attain very high accumulated strains, and thus, very high average misorientations, achieve excellent superplastic properties ($e_f \geq 550\%$) at high strain rates ($\approx 10^{-2} s^{-1}$) and intermediate temperatures (≈300°C), with higher elongations than for ECAP and ARB processed samples. Although stress exponent values are not as low as 2, especially for the latter samples, grain boundary sliding is the operative deformation mechanism. The alloy is microstructurally stable up to 300°C due to the Zener pinning effect of precipitates on grain boundaries hindering discontinuous recrystallization and excessive grain growth.

Resumen

Este trabajo de investigación considera diferentes aspectos que influyen en el refinado y el aumento progresivo de desorientación de la aleación de aluminio aeroespacial 7075 (Al-Zn-Mg-Cu) procesada por métodos de deformación

plástica severa, tales como ECAP, ARB, HPT y FSP, así como el efecto sobre las propiedades mecánicas, especialmente a temperaturas de intermedias a altas. El proceso ECAP muestra que el tamaño del (sub)grano final se predice mejor por la tensión aplicada que por la deformación acumulada. El proceso ARB muestra que el refino progresivo con el aumento de la desorientación se obtiene en condiciones en las que prevalece más bien la recuperación en vez de procesos discontinuos de recristalización. FSP y HPT, que alcanzan tensiones acumuladas muy altas y, por tanto, desorientaciones medias y muy altas, logran excelentes propiedades superplásticas (FE ≥ 550%) a altas velocidades de deformación (≈ $10^{-2}s^{-1}$) y temperaturas intermedias (≈ 300 °C), con mayores elongaciones que en las muestras procesadas por ECAP y ARB. Aunque los valores del exponente de tensión no son tan bajos como 2, especialmente para estas últimas muestras, es el deslizamiento en límite de grano el mecanismo de deformación operativo. La aleación es microestructuralmente estable hasta 300 °C debido al efecto Zener que fija los precipitados en los límites de grano impidiendo la recristalización discontinua y el crecimiento del grano excesivo.

Keywords: Severe plastic deformation, refining of Al 7075, processing stress, recovery/recrystallization, low temperature high strain rate superplasticity

Palabras clave: Deformación plástica severa, afino de Al 7075, Tensión de procesado, recuperación/recristalización, tasa de superplasticidad a baja temperatura y elevada deformación.

1. Introduction

The aerospace Al 7075 alloy and, in general, the 7XXX family, presents excellent mechanical properties at room temperature, with high yield and ultimate tensile strength together with sufficient ductility [1-3]. These are the reasons why its use in airplanes is much extended. However, its conformability at high temperatures presents some restrictions which limit the final form of parts and require extensive use of rivets [4]. This could be in great extent avoided, saving costs in machining operations and riveting, and thus saving additional weight and difficulties, by superplastic forming at high temperature. Superplastic forming usually requires fine (<10μm), equiaxic and highly misoriented grains so that the operative deformation mechanism is grain boundary sliding (GBS) [5-6]. In this way, very high deformations at low stresses can be achieved making possible the forming of complex forms.

However, till recently, the superplastic forming strain rates have been very low ($\leq 10^{-4}$ s^{-1}) and temperatures very high not being cost effective but for expensive parts of high responsibility, as for some aerospace Titanium parts [7]. Recently, the progress of severe plastic deformation (SPD) has allowed the attainment of very fine submicrometric grain sizes with high average misorientations in a vast range of alloys, including the 7075 alloy [8-18], which develops superplasticity at higher strain rates and lower temperatures.

There are a variety of SPD techniques, being the most representative equal channel angular pressing (ECAP) [8, 12, 16-17, 19-21], accumulative roll bonding (ARB) [13-14, 18, 22-25], high pressure torsion (HPT) [9, 11, 26-31] and friction stir processing (FSP) [32-39]. Figure 1 presents schematics of the four processing methods. They differ in the different conditions of strain, strain path, strain rate, stress and temperature under which the material deforms. In this work, the objectives are to maximize the refining of the 7075 alloy to maximize superplastic properties, and to determine the decisive parameters and the underlining physical metallurgy phenomena to optimize processing. Recent achievements by our group at CENIM-CSIC, Madrid (Spain) regarding these four SPD processing methods on the Al 7075 alloy will be shown and discussed in terms of grain refining processes and superplastic properties at intermediate to high temperatures [10-11, 13-18, 29, 31, 38-39].

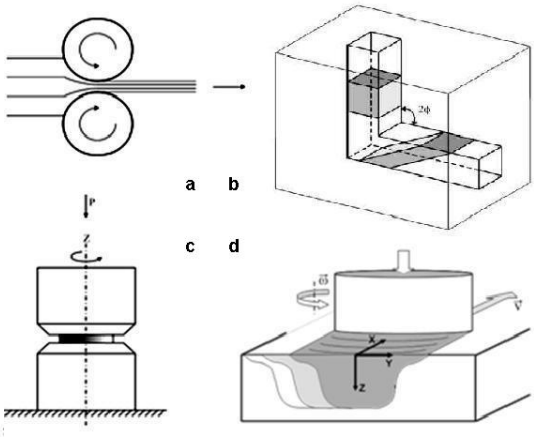

Figure 1. Schematics of processing methods a) ARB, b) ECAP, c) HPT and d) FSP.

2. Experimental Method

The as-received aluminum alloy used in the present study was a rolled Al 7075-T651 plate of 12 mm in thickness for the ECAP and HPT processed samples, and rolled 2 and 3 mm Al 7075-T6 sheets for the ARB and FSP processed samples, respectively. The composition in weight percentage of the alloy is 5.68 Zn, 2.51 Mg, 1.59 Cu, 0.19 Cr, 0.19 Fe, 0.052 Si, 0.025 Ti, 0.007 Mn and balance Al.

The Al 7075-T651 samples were subjected to an overaging heat treatment at 280 °C during 5 h prior to the ECAP and HPT processing to obtain a stable initial microstructure, denominated in the following Al 7075-O.

ECAP processing was performed using a sharp-cornered 90° ECAP die [16-17, 51]. Samples with dimensions 70 mm × 10 mm × 10 mm were ECAP processed by route B_C. Each sample was initially pressed once at room temperature (N=1), and then pressed repetitively through a total of 8 passes at 130 °C, equivalent to a imposed strain of $\varepsilon_t \approx 8$. In addition, samples were ECAP processed through 3 passes at different temperatures, 80, 130 and 180 °C, to evaluate the influence of processing temperature (T_p). The load-displacement (F-d) curves for ECAP processing were recorded by a universal testing machine coupled to the ECAP equipment. F_{max} is a representative value of the force needed to push the sample through the channel. This value divided by the section of the sample, 1 cm^2, is related to the stress withstood by the sample during processing (σ_{Proc}), i.e. the "processing severity".

HPT samples of 10 mm diameter (r = 5 mm) and 1 mm in initial thickness, t, were sliced from the overaged alloy and processed by HPT in unconstrained conditions [11, 29, 31]. A pressure of 6 GPa was applied to the samples and then were subjected to five complete revolutions to a final thickness of about 0.7 and diameter of 10 mm, in 5 minutes. The shear deformation introduced by turn is an increasing function of disk radius up to $\gamma = 2\pi r/t = 45$ at the periphery of the disk. For 5 turns $\gamma = 225$, equivalent to $\varepsilon_t \approx 130$ [40].

ARB processing of the 2 mm Al 7075-T6 sheet was performed in non lubricated conditions using a two-high mill with a roll diameter of 131 mm and a peripheral roll speed of 346 mm/s [13-14, 18]. Initially, two pieces with dimensions 2 x 30 x 180 mm^3 were cut, cleaned with methyl ethyl ketone, put one on top of the other and fastened by steel wires. The resulting 4 mm-thick

specimen was held for 5 minutes at 300 or 350°C in a preheated electric furnace and straight afterwards undergone a thickness reduction of 3:1, equivalent to a true strain of 1.1, by a single rolling pass. Immediately after rolling the resulting 1.33 mm-thick specimen was water quenched. Afterwards, it was divided in three identical pieces that were supplied to the next ARB pass. From that moment on the procedure described above was executed up to 5 more times maintaining the rolling direction (RD). The microstructures of the ARBed samples were characterized on the rolling plane in a section located at a depth of 40% from the surface [13-14, 18].

FSP of the 3 mm 7075-T6 sheet was performed in one pass using a 3 mm-diameter threaded pin with a 9.5 mm shoulder. The processing conditions were 1000 rpm and advance sped of 500 mm/min. The sheet was supported at a liquid nitrogen refrigerated copper plate. Total deformation per pass varies as a function of tool pin and processing parameters, and it could be estimated as $\varepsilon \approx 20\text{-}90$ [41].

The samples were characterized by transmission and scanning electron microscopy (TEM and SEM) including automated crystal orientation mapping (ACOM-TEM) and electron backscatter diffraction (EBSD) in the SEM for the measurement of grain orientations [13, 16, 51]. The ACOM-TEM consists of analyzing spot diffraction patterns [42-44] rather than Kikuchi lines, which are considered in the EBSD technique. For studies involving large strains, the spot patterns are preferred, because they are less sensitive to the internal stresses resulting from severe plastic deformation. This technique is successful in the characterization of deformed structures and it discriminates (sub)grain structures down to 100 nm and misorientations ≥1°. Because of the limited angular resolution of the EBSD system, misorientations below 2° were neglected. Boundaries with misorientations from 2° to 15° were defined as low angle boundaries (LABs), while those with misorientations greater than 15° were defined as high angle boundaries (HABs). The mean boundary misorientation angle (θ) and the fraction of high-angle boundaries (f_{HAB}) was calculated from the misorientation data obtained.

A set of tensile tests to failure was performed from 250 to 400°C at a constant crosshead speed corresponding to initial strain rates of 10^{-2} s^{-1} or 10^{-3} s^{-1}. Another set of tensile tests was performed using the strain rate change (SRC) method. From these tests the apparent stress exponent (n_{ap}) was determined. After the tests the gauge sections were examined in the SEM.

The maximum deformation applied by the different SPD methods are: ε_t = 5.5 for 5 passes ARB 3:1 at 300°C and ε_t = 6.6 for 6 passes ARB 3:1 at 350°C, ε_t = 8 for 8 passes ECAP 90° at 130°C by route B_c, ε_t > 20 for 1 pass N_2 refrigerated FSP at 1000rpm-500mm/min, $\varepsilon_t \approx 130$ for 5 HPT turns at 6 GPa. The temperatures the material withstands during processing are about 130°C for ECAP and HPT (due to adiabatic heating [29]), 300-350°C for ARB and ≥400°C for FSP [45]. Unfortunately, the stresses withstood by the samples under SPD are not well known since it is difficult to measure the shear stresses involved during the different processing methods. For FSP it is also difficult to determine the peak temperature [45]. For ARB very rough estimates considering energy consumption can be performed, and for HPT a function of hydrostatic pressure and torque should be taken into account. However, the simplicity of ECAP design, together with a set of equal dimensions samples, processed at the same conditions of strain rate and temperature, giving consistent results, including those related to the applied force, permit to relate the applied stresses during ECAP processing to the microstructures obtained. These valuable data will be presented in the results section.

3. Results

Microstructural examinations of the Al 7075 T6 alloy showed a fully-recrystallized microstructure composed of pancake-shaped grains of dimensions 60 x 47 x 4 μm^3 [13]. As expected, the overaged Al 7075-O alloy microstructure was coarser, about 350 x 200 x 15 μm^3 [16-17].

As a result of SPD fine microstructures are obtained. Figure 2 shows the important grain refinement obtained for the different processing conditions. All microstructures present (sub)grain sizes well below 1 µm, being about 100 nm (HPT), 150 nm (ECAP), 280 nm (FSP) and 350 nm (ARB). This large refinement will be associated to the "severity" of the processing, related to the "processing stress" and argued in the discussion section.

Table 1 shows (sub)grain data for a set of ECAPed samples in different processing conditions as obtained by TEM observations. As it is clearly observed in the table, the (sub)grain size decrease both with decreasing temperature and with increasing the number of passes, as expected.

Figure 3 presents the maximum applied forces (F_{max}, in kN) during ECAP processing as a function of the number of passes for three processing

temperatures (80, 130 and 180°C). All the N=1 passes were performed at room temperature so they are not considered in future analyses. In this graph it is clearly observed that the "processing stress" (F_{max}/S, being S the ECAP section equal to 1 cm^2) increases with both decreasing temperature and increasing the number of passes. As it will be shown in the discussion, there is an inverse relationship between the processing stress and the (sub)grain size, at any temperature.

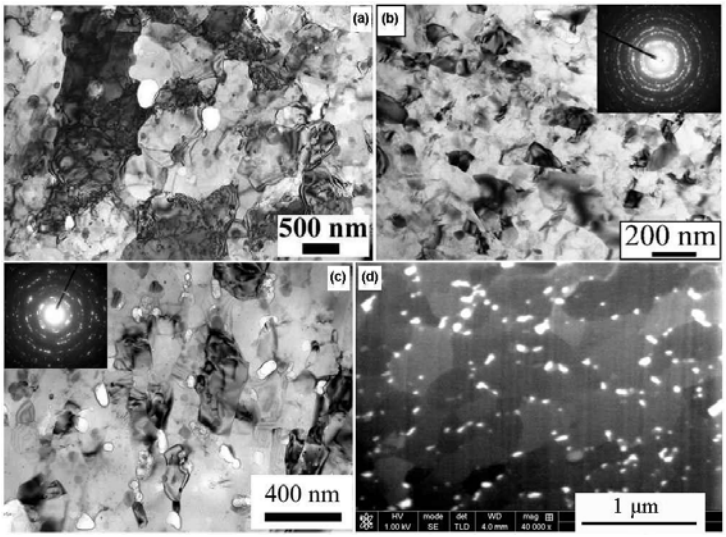

Figure 2. a-c) TEM micrographs of samples ARB 3:1 a 300°C 4 passes, HPT 6 GPa 5 revolutions and ECAP 3:1 at 130°C 8 passes, respectively, and d) FIB-SEM micrograph of sample FSP 1000rpm at 500 mm/s N_2 refrigerated.

Table1. (Sub)grain size (nm) for samples subjected to ECAP 90˚ at various temperatures and number of passes.

d, nm	**Temperature**		
N passes	**80˚C**	**130˚C**	**180˚C**
1p		>400	
3p	153 ± 5	200 ± 5	318 ± 17
5p		175 ± 6	
8p		163 ± 5	

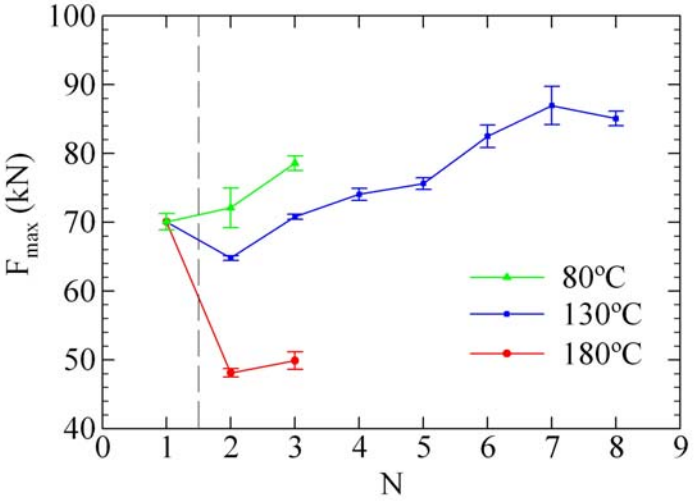

Figure 3. Maximum measured force during ECAP, F_{max}, as a function of the number of passes for three processing temperatures.

Figure 4 shows (sub)grain data from TEM observations corresponding to ARBed samples with a 3:1 thickness reduction at processing temperatures of 300 and 350˚C. It is clear from the figure that at a processing temperature of 300°C (sub)grains decrease in size with number of passes similarly to other severe plastic deformation methods operating at low-intermediate temperature. At low-intermediate temperature discontinuous recrystallization processes are less probable unless an extreme work hardening is obtained, and recovery processes are most likely, especially at intermediate temperature. On the contrary, at 350°C (high temperature), no additional refining is obtained after the first pass, being (sub)grain size about the same or even higher for higher number of passes. This unexpected phenomenon will be attributed to discontinuous recrystallization during interpass heating which destroys partially the previous fine microstructure.

Regarding misorientations, as it is expected, they increase with increasing the total deformation imposed for all the processing methods (except for too high temperature processing such as ARB at 350°C). Misorientations have been measured by EBSD-SEM (ARB, FSP) or by ACOM-TEM (ECAP). It must be pointed out that ACOM-TEM possesses higher accuracy that EBSD and, therefore, a higher amount of low angle boundaries and little misorientations are resolved, as it is the case for the ECAPed 130°C 8p sample. For the ARB 3:1

5p sample θ = 32.5° and f_{HAB} = 76% are measured. For the ECAP 130°C 8p sample θ = 17,6˚ and f_{HAB} = 56% have been measured, which should be higher if measured with EBSD. The sample processed by FSP presents θ = 41°, with 90% f_{HABs}. These values for FSP are very high. We should bear in mind that the MacKenzie random distribution implies values of misorientation approximately 41° and 97% f_{HAB}. HPTed sample could not be characterized by EBSD due to its fine grain. However, values of misorientation and fraction of high angle boundaries higher than those for the FSPed sample are expected.

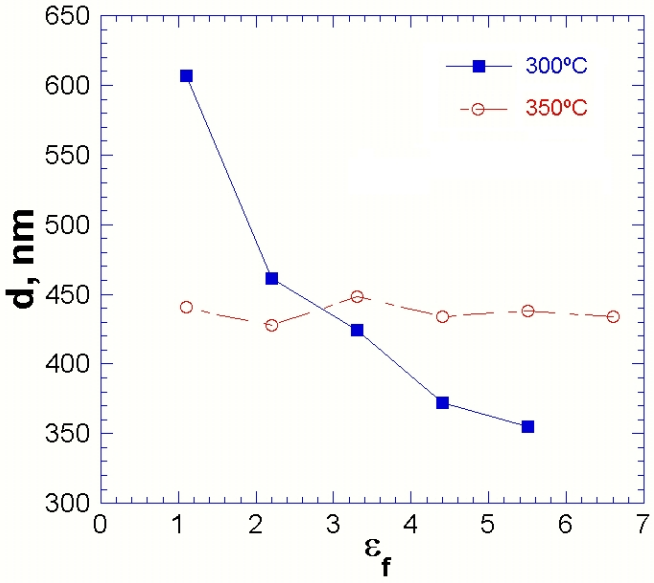

Figure 4. (Sub)grain size, d, vs. accumulated deformation, ε_t, for ARB 3:1 processing at 300 and 350°C.

As a consequence of the large grain refinement, superplasticity operates in certain stress-strain rate-temperature conditions. Tensile tests were performed for all the samples but for the HPTed ones, for which small punch tests (SPT) were carried out, at intermediate to high temperatures to determine the superplastic window. After the tests, topographies of tested surfaces (polished before testing) were observed to confirm grain boundary sliding as the operative deformation mechanism. Figure 5 shows that equiaxed fine grains have emerged and slide each other separately, with a grain aspect ratio (GAR) close to one and high elongations that cannot be explained by slip creep mechanisms. Additionally, some fibers coming from the intense

accommodation at triple junctions can be observed. Clearly these features cannot be explained by any dislocation slip dominant operative mechanism, neither climb nor glide controlled, but for a GBS operative deformation mechanism.

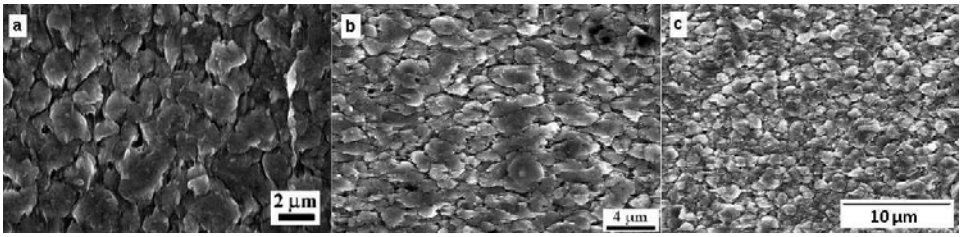

Figure 5. Surface topography of tensile tested samples showing the operation of GBS: a) ARB 300˚ 3:1 5p tested at 300˚C 10^{-2} s^{-1}, b) ECAP 130˚C 8p tested at 300˚C 10^{-3} s^{-1}, c) FSP tested at 300˚C 10^{-2} s^{-1}.

Effectively, tensile tests showed for ECAP and ARB processing methods that, generally, the higher is the number of passes, i.e., the smaller and more misoriented grains, the larger the elongation to failure, the lower the flow stress and the lower the apparent stress exponent, n_{ap}, are. For instance, for ARB 300°C 3:1 4p an elongation of 202% at 10^{-2} s^{-1} and 300°C with n_{ap} = 3.6, or 235% at 10^{-2} s^{-1} and 350°C with a n_{ap} = 3.1 is obtained. At this point it should be mentioned that the 4p sample gave better results than the 5p sample. This is attributed to the fact that processing at 300°C coarsens progressively the fine hardening $MgZn_2$ precipitates generated at the T6 temper. With increasing the number of passes the precipitates grow and the distance among them becomes larger. As predicted by the concept of Zenner pinning [46], the processed alloy will be more prone to recrystallization and grain coarsening with increasing the number of passes, as it is the case for the 5p sample respect to the 4p sample. Therefore, the higher elongation of the 4p sample is attributed to its microstructural stability. These concepts will be abounded in the discussion.

In the case of ECAP 90° at 130°C 8p an elongation to failure of 320% at 10^{-3} s^{-1} is obtained, and 210% at $10^{-2}s^{-1}$ at 300°C both with approximately n_{ap} = 3.2. For the FSPed sample, a value of 550% at 300°C and 10^{-2} s^{-1} with n_{ap} = 2.5 is achieved. The HPTed sample was mechanically tested by SPT [11] and showed large elongation to failure as well as a value of n_{ap} = 2.5 at 300°C, at ≈ 10^{-2} s^{-1}. As usually higher n_{ap} values are obtained for ECAP samples tested by SPT than

by tensile tests, the value obtained of n_{ap} = 2.5 for the HPT sample can be considered as an overestimation. Therefore, n_{ap} about 2.3 and elongations in excess of 720% could probably be obtained, although these values should be checked with tensile tests. In the discussion a prediction of these values is made.

At this point it has to be mentioned that although GBS and superplastic deformation has been undoubtedly found, the tests never achieved the theoretical stress exponent value of n=2. However, a clear inverse relationship between elongations and n_{ap} is observed, which, again, correlates excellently with both the fineness and the misorientation of the obtained grains.

4. Discussion

Important advances have been made in the microstructure refinement and mechanical properties improvement, especially at intermediate to high temperatures, of the aerospace Al 7075 alloy by means of SPD [11-18]. The use of four very different SPD processing methods such as ECAP, ARB, FSP and HPT, has allowed a sufficiently broad view so as to determine the principal aspects influencing refining processes and mechanical properties, especially superplasticity [11-12, 17-18].

From results obtained for every processing method such as ARB and ECAP, and from combination of all processing methods it has been shown that as long as there is not any discontinuous recrystallization process the material gets its microstructure finer and more misoriented with increasing deformation. However, is the (sub)grain size a function of strain? It is our contention that it is not, as it will be shown below.

The refinement is usually associated to the “severity” of the processing. So far, the concept of severity has been related to the accumulated deformation during processing [8, 30, 47-50]. However, it is our contention that deformation is not the key parameter to predict the fine microstructures obtained, but the stress, through the “processing stress” [51].

As it is well known, refinement processes are usually related to the generation and reorganization of massive amounts of dislocations [52]. This has to be in this way because each dislocation is a linear lattice distortion causing a stress field, which approximately decays from its core as the inverse of distance [53]. The only way a dislocation (a mobile stress field) can be moved is through

other stress fields. Furthermore, the "objective" of dislocation movement is to reduce the external stress field and the total energy of the applied stress field by producing plastic deformation of the sample. Therefore, under an external applied stress, with increasing deformation, there is a progressive evolution from dislocation tangles to cells, subgrains and grains, assisted by dislocation mobility. It has to be noted that the size of these lower energy structures (cells, subgrains and grains) is given essentially by the applied stress. This is the case for development of subgrains during deformation at high temperature, being their size inversely proportional to the flow stress [54-55]. Let's perform a thought experiment: A sample is pressed in an ECAP device where the force is registered. Once half sample has passed through the intersection of the entry and exit channels, up to certain force level, the device is now set up to load control and the new load is set to half the previous force. It follows in this case, logically, that the sample will not deform anymore. This is because the dislocation structures, cells and (sub)grains have rearranged themselves to certain characteristic distances such that they have defined the minimum stress needed for another dislocation to move in the just generated "microstructural stress field". Deformation can only continue if applied stress is larger than the stress associated to the microstructure at that instant.

This is consistent with Table 1 and Figure 3 for the ECAPed samples for which the processing load could be measured. These data show clear correlation between fineness and higher load, which increases with the number of passes. Additionally, it is well known that HPT usually achieves finer structures than those associated to ECAP. This is logical as HPT is usually performed under a hydrostatic pressure of several GPa, which have some influence in the refining capacity [30, 56-57].

To illustrate the fact that "processing stress" is the driving force for microstructural refinement in Figure 6a the "processing stress" for ECAP, defined as the maximum load during processing divided by channel cross section, is plotted versus the (sub)grain size for various samples. Figure 6b shows a plot of the same data points as figure 6a but represented as accumulated deformation, ε_t, as a function of (sub)grain size. Clearly there is an inverse relationship between applied stress and (sub)grain size, which is more predictive than the relation involving accumulated deformation and (sub)grain size. Therefore, not only is the processing stress the driving force for refining the microstructure, but also is the main variable with true predictive

capability. It is suggested in these lines that in the future all processing stresses should be measured, or at least estimated, when the direct measurements are too complicated, to benefit from this predictive capability. It should be mentioned that the presented "processing stress" is an estimator of the stress field the sample is suffering. It is apparent that the different stress fields applied by the various processing methods could not be immediately comparable as there should be some influence of hydrostatic pressure components (and in general of the whole stress tensor), friction, strain localization, etc., on the shear stresses concerned in the dislocation generation and movement. However, it is our contention that all these data will be rationalized successfully in the future.

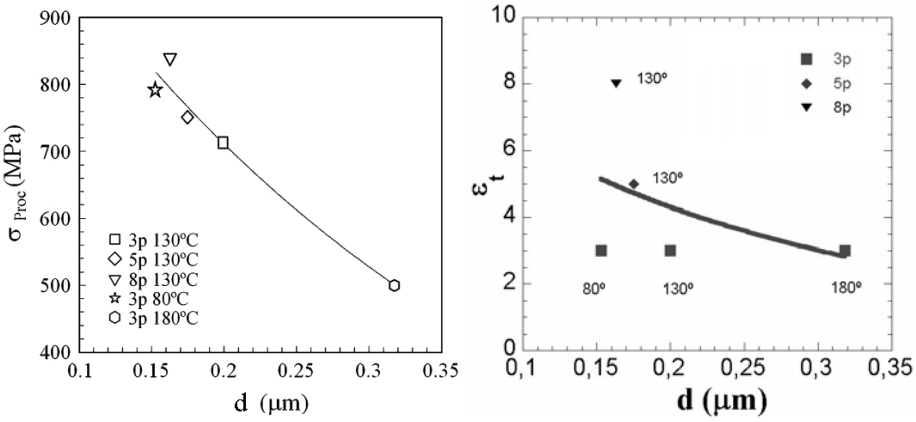

Figure 6. a) σ_{Proc} and b) ε_t as a function of d for ECAP processed samples at various conditions.

As it is expected, with increasing accumulated applied deformation, (sub)grains increase gradually their relative misorientations. This will be of maximum importance for superplastic properties. As widely reported, fine, equiaxed and highly misoriented grains are needed for GBS to operate [5-6] as it has been corroborated again with the present data. In the case of SPD, in general, better superplastic properties are obtained with increasing misorientations, which in turn, increase with accumulated deformation. This happens usually when processing temperature is not excessively high or when discontinuous recrystallization processes do not alter the monotonic refining process. I.e., it is convenient for the progressive refining process the operation of recovery processes, which are directly related to dislocation mobility. Dislocation

mobility [52-53] is related to dislocation core structure (stacking fault energy) and temperature. High stacking fault energy promotes easy dislocation interaction and therefore, easy recovery, such as in aluminum. Low stacking fault energy implies a more extended dislocation core complicating its mobility and microstructure recovery, thus promoting high work hardening and recrystallization processes, which are typical in copper. Additionally, dislocation mobility increases with temperature. Regarding refining processes, recovery is usually more beneficial than discontinuous recrystallization because grain boundary migration favors grain coarsening. However, recrystallization and grain coarsening can be retarded with a convenient volume fraction of stable precipitates. The Al 7075 alloy possesses a variety of precipitates, both stable and unstable with increasing temperature, with maximum volume fraction close to 300°C which decreases with temperature to a minimum at about 465°C [58]. Therefore, recovery processes are expected to be dominant up to 300°C, while recrystallization processes may be deleterious at higher temperatures.

For the ECAPed and HPTed samples the starting alloy was overaged 5h at 280°C [10-11, 16-17], thus being in the state of minimum hardness corresponding to coarse hardening precipitates with the largest distance between them and with limited Zener pinning force on the grain boundaries. For the FSPed and ARBed samples the initial alloy was the Al 7075 in T6 temper [13-14, 18, 39], with very fine hardening precipitates and minimum interparticle distance. However, processing at high temperatures produces coarsening of precipitates. For ARBed samples, processing at 300°C increase precipitates size with increasing number of cycles, thus reducing pinning force on grain boundaries and therefore, reducing thermal stability with increasing N. When ARB is performed at 350°C not only coarsening of precipitates is obtained but also some dissolution, thus reducing additionally the pinning force on grain boundaries and increasing the thermal instability [13]. This is the cause of successive discontinuous recrystallizations impeding the achievement of finer grains by ARB at 350°C (Figure 4). Confirming this scenario is the instability of superplastic deformation during tensile testing at 350°C for some ARBed and ECAPed samples [17]. Furthermore, suspectedly, Figure 5 showed similarly coarsened grain sizes after deformation by ECAP and ARB, indicating that almost independently of the initial (sub)grain size, this one grows towards a size given approximately by the effective interparticle distance for Zener pinning drag. Therefore, above 300°C, Al 7075 alloy is not thermally stable and

the grains tend to grow quickly, even abnormally in certain conditions [17]. This microstructure stability temperature limit is, consequently, a problem for superplastic forming unless the processing is made at temperatures below 300˚C. However, nowadays, thanks to SPD, it is possible to obtain very fine, equiaxed and misoriented grains providing superplasticity at high strain rates and lower temperatures (≤300°C) so that it is feasible and profitable its industrial implementation.

Regarding the mechanical tests, it has been observed that the finer and more misoriented microstructures are, the higher elongations are obtained (as high as 550% for FSP), as well as lower stresses and lower stress exponents (down to n_{ap} = 2.5 for FSP). This "soft" behavior is obtained at a temperature as low as 300°C and at strain rates as high as $\approx 10^{-2}$ s^{-1}, for which high strength, much lower ductility and stress exponent as high as n_{ap} = 10 is achieved ("hard" behavior) for the as received material. Additionally, the topographic surfaces of tensile tested specimens showed equiaxed, emerging fine grains (1-3 µm) with some fibers in the loading direction corroborating the operation of GBS as the principal deformation mechanism (Figure 5).

Until recent years, previous to SPD, with thermomechanical treatments for which grain sizes about 10 µm were obtained in this alloy, superplastic conditions were found at much higher temperatures (≈500°C) and lower strain rates ($\approx 10^{-4}$ s^{-1}), being industrially expensive. It must be mentioned that usually, at these high temperatures, a stress exponent of n_{ap}=2 is obtained for most superplastic alloys. At the same time, a smooth transition in deformation mechanism towards dislocation slip with n_{ap} = 5 is produced at higher stresses. However, at temperatures 200°C lower, it is rarely found apparent stress exponents as low as 2. Most samples obtain values of $n_{ap} \approx 3$, which could suggest the operation of a mechanism for which solute drag would influence dislocation glide. However, the studies concerning the Al 7075 alloy processed by SPD confirm that this is not the case for several reasons: First, there is negligible concentration of solutes at 300°C. Second, no transients during creep related to solutes were found. Third, the processed alloy is "softer", not "harder" ("solute drag" is a reinforcing mechanism). Fourth, grain morphology does not match with the large elongations obtained if a dislocation mechanism would operate, disagreeing with Figure 5. Fifth, the stress exponents higher than 2 are nothing but the transitory values from a very high initial $n_{ap} \approx 10$

towards n_{ap} = 2 which reflect the more or less significant contribution of GBS to the total elongation.

To show this latter point, Figure 7 shows a graph of the elongation to rupture as a function of the obtained n_{ap}. The three square points correspond to the ARB 4p, ECAP 8p and FSP processed samples tensile tested at the same conditions of 300°C and 10^{-2} s^{-1}. The solid curve fit has been traced taking into account these three points. Additionally, this fitting fulfils two conditions: for n = 1 elongation is infinite and for n = ∞ elongation is zero. These conditions are in line with deformation stability criteria (not taking into account strain hardening coefficient), for which with a strain rate sensitivity m = 1/n = 1 there should be no necking (maximum stability) and with m=0 (n = ∞) necking should be immediate (minimum stability). A simple relation for the ductility can be chosen:

$$e_f = \frac{A}{\exp^{(n-1)} - 1} \qquad (1)$$

where e_f is the engineering elongation to failure, n is the stress exponent, and A = 19.18 is a fitting constant.

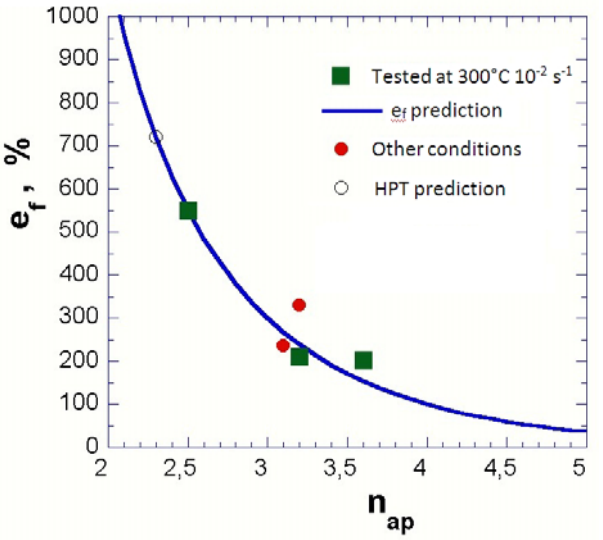

Figure 7. Elongation to failure (%) vs. n_{ap} for the ARB, ECAP and FSP samples. The solid line and the HPT value are predictions from Eq. 1.

Additionally, three points corresponding to ECAP 130°C 8 passes tested at 300˚C and 10^{-3} s^{-1} (n_{ap} = 3.2 giving e_f = 330%), and ARB 300°C 3:1 tested at 350˚C and 10^{-2} s^{-1}, (for 4 passes n_{ap} = 3.1 with e_f = 235%, and for 3 passes n_{ap} = 3.2 with e_f = 204%), have been incorporated. As it can be observed in Figure 7, these three solid round points are in line with predictions of eq. 1. Using this expression the tensile elongation of the HPTed sample can be estimated, assuming n_{ap} = 2.3, as about 720%.

This value is very realistic and it will be checked when additional HPT processings will be performed. In general, it is observed a very reasonable trend of tensile elongation vs. apparent stress exponent for this alloy, which could indicate that the transition from high apparent stress exponents ($n_{ap} \geq$ 10, in the power law breakdown region, PLB) towards ideal superplastic n_{ap} = n = 2 is much slower, requiring much more microstructure transformation, than for superplastic transition for coarser microstructures at higher temperatures and lower strain rates (well below the PLB region). Thus, there is still room for further improvements in ductility as long as n_{ap} deviate from the ideal value of 2. However, despite values apparently high such as n_{ap} = 3.6, the alloy deforms mainly by GBS, as already confirmed by microstructure and tensile data [11, 17]. These n_{ap} values higher than ideal are, in fact, related to microstructure, as it has been already pointed out, since n_{ap} was inversely related to the presence of very fine and highly misoriented grains. Therefore, for superplastic forming purposes it is convenient to process the alloy severely (the higher the stress, the best, at limited temperature) with high enough accumulated deformation to guarantee a very elevated fraction of high angle boundaries.

5. Conclusions

Large refinement can be obtained by SPD processes in the Al 7075 alloy, being (sub)grain as fine as 100 nm (HPT). ECAP, FSP and ARB also obtain (sub)grain sizes from 150 to 350 nm. Average misorientations and f_{HAB} increase with accumulated applied strains.

The main cause of the grain refinement is the “processing stress” as shown by ECAP processing under different conditions. This is expected because dislocations are themselves sources of stress fields.

Low processing temperatures are preferred such that recovery processes are favored against discontinuous recrystallization processes, which enhance

microstructure instability. Additionally, diminishing precipitates volume fraction and increasing coarsening with increasing temperature limit processing stability of the Al 7075 alloy to about 300°C.

Improved superplasticity is obtained with decreasing grain size and with increasing misorientation at relatively low temperatures 250-350°C and high strain rates (10^{-2} s^{-1}). Elongations as high as 550% at 300°C and 10^{-2} s^{-1} are obtained by FSP and an elongation of 720% is predicted after HPT processing with a predictive simple exponential equation as a function of n_{ap}, which takes into account deformation stability criteria.

Stress exponents at 300˚C decrease from n_{ap} = 10 (unprocessed alloy) towards $n_{ap} \approx 2$. Values as low as 2.5 for FSP and even lower for HPT, decreasing with increasing the misorientation of the samples, are found. ECAP and ARB samples (having lower average misorientation values) present higher stress exponents about $n_{ap} \approx 3$ but they are not due to a solute drag mechanism but to GBS in less superplastic microstructures.

Severe plastic deformation is nowadays capable of increasing substantially, and profitably, the formability of the 7075 alloy.

6. Bibliography

[1] J.E. Hatch (Ed.), Aluminium: Properties and Physical Metallurgy, American Society for Metals, Ohio, 1984, pp.370.

[2] E.A. Starke Jr, J.T Staley, *Prog. Aerospace Sci*. 32 (1996) 131-172.

[3] G. Fribourg, Y. Bréchet, J.L. Chemin and A. Deschamps, *Metall. Mater. Trans. A* 42 (2011) 3934-3940.

[4] L. Boni, A. Lanciotti, *Fatigue Fract. Eng. Mater. Struct.* 34 (2011) 60-71.

[5] J.W. Edington, K.N. Melton, C.P. Cutler, *Prog. Mater. Sci*. 21 (1976) 63-170.

[6] O.A. Ruano, O.D. Sherby, *Rev. Phys. Appl*. 23 (1988) 625-637.

[7] P.N. Comley, *J. Mater. Eng. Perform.* 13 (2004) 660-664.

[8] R.Z. Valiev, R. K. Islamgaliev, I.V. Alexandrov, *Prog. Mater. Sci.* 45(2000) 103-189.

[9] A.P Zhilyaev, M.D. Baró, T.G. Langdon, T.R. McNelley, Reviews on Advanced Materials Science 7 (2004) 41-49.

[10] J.M. García-Infanta, A.P. Zhilyaev, C.M. Cepeda-Jiménez, O.A. Ruano, F. Carreño, *Scripta Mater.* 58 (2008) 138-141.

[11] J.M. García-Infanta, A.P. Zhilyaev, A. Sharafutdinov, O.A. Ruano, F. Carreño, *J. Alloys Comp.* 473 (2009) 163–166.

[12] K. Turba, P. Málek, E.F. Rauch, F. Robaut, M. Cieslar, *Int. J. Mater. Res*. 100 (2009) 851-857.

[13] P. Hidalgo, C.M. Cepeda-Jiménez, O.A. Ruano, and F. Carreño, *Metal. Mater. Trans. A* 41A (2010) 758-767.

[14] P. Hidalgo, C.M. Cepeda-Jiménez, O.A. Ruano, F. Carreño, *Mater. Sci. Forum* 638-642 (2010) 1929-1933.

[15] C.M. Cepeda-Jiménez, P. Hidalgo, M. Pozuelo, O.A. Ruano and F. Carreño, *Mater. Sci. Eng. A* (2010) 2579-2587.

[16] C.M. Cepeda-Jiménez, J.M. García-Infanta, O.A. Ruano, F. Carreño, *J. Alloys Comp*. 509 (2011) 8649– 8656.

[17] C.M. Cepeda-Jiménez, J.M. García-Infanta, O.A. Ruano, F. Carreño, *J. Alloys Comp*. 509 (2011) 9589– 9597.

[18] P. Hidalgo-Manrique, C.M. Cepeda-Jiménez, O.A. Ruano, F. Carreño, *Mater. Sci. Eng*. A 556 (2012) 287–294.

[19] R.Z. Valiev, N.A. Krasilnikov and N.K. Tsenev, *Mater. Sci. Eng. A*, 137 (1991) 35-40.

[20] V.M. Segal, *Mater. Sci. Eng. A* 197 (1995) 157-164.

[21] S.D. Terhune, D.L. Swisher, K. Oh-Ishi, Z. Horita, T.G. Langdon, T.R. McNelley, *Metall. Mater. Trans. A* 33 (2002) 2173-2184.

[22] Y. Saito, N. Tsuji, H. Utsunomiya, T. Sakai, R.G. Hong, *Scripta Mater*. 9 (1998) 1221-1227.

[23] N. Tsuji, Y. Saito, S.-H. Lee, Y. Minamino, *Adv. Eng. Mater*. 5 (2003) 338-344.

[24] X. Huang, N. Tsuji, N. Hansen, Y. Minamino, *Mater. Sci. Eng. A* 340 (2003) 265-271.

[25] S. Roy, D.S. Singh, S. Suwas, S. Kumar, K. Chattopadhyay, *Mater. Sci. Eng. A* 528 (2011) 8469-8478.

[26] N.A. Smirnova, V.I. Levit, V.I. Pilyugin, R.I. Kuznetsov, L.S. Davydova, V.A. Sazonova, *Fiz. Met. Metalloved*. 61 (1986) 1170-1177.

[27] A. Vorhauer, R. Pippan, *Scripta Mater*. 51 (2004) 921-925.

[28] G. Sakai, Z. Horita, T.G. Langdon, *Mater. Sci. Eng. A* 393 (2005) 344-351.

[29] A.P. Zhilyaev, J.M. García-Infanta, F. Carreño, T.G. Langdon, O.A. Ruano, Scripta Mater. 57 (2007) 763-765.

[30] A.P. Zhilyaev and T.G. Langdon, *Prog. Mater. Sci*. 53 (2008) 893-979.

[31] C.M. Cepeda-Jiménez, J.M. García-Infanta, A.P. Zhilyaev, O.A. Ruano, F. Carreño, *J. Alloys Comp*. 509 (2011) 636-643.

[32] R.S. Mishra, M.W. Mahoney, S.X. McFadden, N.A. Mara, A.K. Mukherjee, *Scripta Mater*. 42 (2000) 163-168.

[33] P.B. Berbon, W.H. Bingel, R.S. Mishra, C.C. Bampton, M.W. Mahoney, *Scripta Mater*. 44 (2001) 61-66.

[34] N. Saito, I. Shigematsu, T. Komaya, T. Tamaki, G. Yamauchi, M. Nakamura, *J. Mater. Sci. Lett*. 20 (2001) 1913-1915.

[35] Z.Y. Ma, R.S. Mishra, M.W. Mahoney, *Acta Mater.* 50 (2002) 4419-4430.

[36] K. Oh-Ishi, T.R. McNelley, *Metal. Mater. Trans. A* 35A (2004) 2951-2961.

[37] F.C. Liu, Z.Y. Ma, *Mater. Sci. Eng. A* 530 (2011) 548-558.

[38] P. Rey, D. Verdera, A. Orozco-Caballero, O. A. Ruano, A. Fernández, D. Gesto, F. Carreño, *XIII Congreso Nacional de Propiedades Mecánicas de Sólidos PMS2012* (Alcoy-Alicante, Spain, 26-28 Sept. 2012), in press.

[39] A. Orozco-Caballero, P. Rey, D. Gesto, D. Verdera, C.M. Cepeda-Jiménez, P. Hidalgo-Manrique, O.A. Ruano, F. Carreño, *XIII Congreso Nacional de Propiedades Mecánicas de Sólidos PMS2012* (Alcoy-Alicante, Spain, 26-28 Sept. 2012), in press.

[40] G.E. Dieter, Mechanical Metallurgy SI Metric Edition, 1988, McGraw-Hill Series in Materials Science and Engineering, ISBN 0-07-084187-X, printed in Singapore.

[41] P. Asadi, R.A. Mahdavinejad, S. Tutunchilar, *Mater. Sci. Eng. A* 528 (2011) 6469-6477

[42] E. F. Rauch, M. Veron, Materialwiss. Werkstofftech. 36 (2005) 552-556.

[43] E. F. Rauch, L. Dupuy, *Arch. Metall. Mater*. 50 (2005) 87-99.

[44] E. F. Rauch, L. Dupuy, *J. Appl. Crystallogr*. 39 (2006) 104-105.

[45] C.G. Rhodes, M.W. Mahoney, W.H. Bingel, R.A. Spurling and C.C. Bampton, *Scripta Mater*. 36 (1997) 69-75.

[46] C. Zener, quoted by C.S. Smith, *Trans. Metall. Soc. A.I.M.E*. 175 (1948) 15-51.

[47] P.J. Apps, M. Berta, P.B. Prangnell, *Acta Mater*., 2005, vol. 53, pp. 499-511

[48] P. Kumar, C. Xu, T.G. Langdon, *Mater. Sci. Eng. A*, 2006, vol. 429, pp. 324-328

[49] R.Z. Valiev, T.G. Langdon, *Prog. Mater. Sci*., 2006, vol. 51, pp. 881-981

[50] N. Kamikawa, X. Huang, N. Tsuji, N. Hansen, *Acta Mater*., 2009, vol. 57, pp. 4198-4208.

[51] C.M. Cepeda-Jiménez, J.M. García-Infanta, E.F. Rauch, J-J. Blandin, O.A. Ruano, and F. Carreño, *Metall. Mater. Trans. A* (2012), in press on-line, DOI 10.1007/s11661-012-1206-5

[52] F.J. Humphreys, M. Hatherly, "Recrystallization and related annealing phenomena", 2nd edition, 2004, Elsevier, Oxford (UK), ISBN: 0 08 044164 5.

[53] D. Hull, D.J. Bacon, "Introduction to dislocations", International Series on Materials Science and Technology 37, 1984, Pergamon Press, Oxford (UK).

[54] O.D. Sherby, P. M. Burke, *Prog. Mater. Sci.* 13 (1968) 323-390.

[55] O.D. Sherby, R. H. Klundt, A.K. Miller, *Metal. Trans. A* 8 (1977) 843-850.

[56] F. Wetscher, A. Vorhauer, R. Pippan, *Mater. Sci Eng A* 410–411 (2005) 213-216.

[57] A. Bachmaier, M. Hafok, R. Pippan, *Mater. Trans*. 51 (2010) 8-13.

[58] R. Deiasi, P. N. Adler, *Metall. Trans. A* 8 (1977) 1177-1183.

7. Acknowledgements

Financial support from the CICYT and MICINN (Projects MAT2003-01172, HF2004-0266, MAT2006-11202 and MAT2009-14452) is gratefully acknowledged. The authors thank J.-J. Blandin and E.F. Rauch for assistance with initial ECAP experiments, A. Zhilyaev for HPT processing, P. Rey, D. Gesto and D. Verdera for performing FSP, A. García Delgado and W.E. More for assistance with electron microscopy and, again, E.F. Rauch for the ACOM-TEM measurements. Finally, the authors make a special mention in memory of P.J. González Aparicio for his assistance with electron microscopy during all these years.

International Symposium on Plastic Deformation and Texture Analysis
Alcoy (Spain) 24-25 September 2012
105-118

CENIM-TECNALIA collaboration in innovation projects of companies: Production, characterization and properties of ferritic steels for high temperature

F. Peñalba[1], M. Carsí[2], O. A. Ruano[2]

[1]TECNALIA, Paseo de Mikeletegi 2, 20009 San Sebastián

[2]CENIM-CSIC, Avenida Gregorio del Amo 8, 28040 Madrid

Abstract

Some main keys needed to participate in innovation projects with companies are given. It also highlights the topics of the projects developed with the industry during the more than 25 years of CENIM-TECNALIA mutual cooperation. Some ferritic steels containing Cr steels (P/T-23; P/T-91; P/T-92) for use at high temperatures in power plants are studied. Process and deformation properties of these steels have also been analyzed. Hot torsion, tensile and compression tests at various temperatures and strain rates are carried out in these steels and the generalized stresses and strains to rupture are determined in order to know the influence of the strain rate in the hot workability. This study has done in steels. Resolution of EN X10CrMoVNb9-1<> P/T91 tube quality problems developed during rolling steel have been conducted by means of analysis of the chemical composition, hot ductility and the study of metallurgical and mechanical properties..

Resumen

Se dan algunas claves necesarias para participar en los proyectos de innovación de las empresas y se destacan los temas de los proyectos con la industria abordados durante los más de 25 años de colaboración mutua.

Se describirán estudios realizados sobre aceros ferríticos al Cr (P/T-23; P/T-91; P/T-92) que trabajan a altas temperaturas en centrales térmicas, sobre los que se analiza la fabricación y propiedades de conformación de las tuberías de estos aceros. Para lo que se realizan ensayos de torsión, tracción o

compresión rápida en caliente a diferentes temperaturas, y velocidades generalizadas de deformación, analizándose la influencia de la velocidad de deformación y temperatura en la laminabilidad de los mismos. En especial, se dan resultados de la resolución de algunos problemas de calidad en tubos de acero EN X10CrMoVNb9-1<> **P/T91,** mediante el estudio de su composición química, su ductilidad en caliente y de sus características metalúrgicas y mecánicas.

Keywords: Innovation projects companies, research collaborative, high temperature steels, chemical composition, hot workability, mechanical and creep properties.

Palabras clave: Proyectos industriales de innovación, colaboración entre centros, aceros para alta temperatura, ductilidad en caliente, composición química, propiedades mecánicas y de fluencia.

1. Introduction

The main keys to participate in innovation projects of companies are:

- Be as close as possible to the company technology in order to influence the creation of a climate for innovation. (MOTIVATE)
- Develop basic and applied knowledge necessary to contribute to the uptake and assimilation of innovation that are keys to industry development in the short to medium term. (DEVELOP APPLIED KNOWLEDGE)
- The knowledge transfer to the company would be done alone or in collaboration with other innovation actors: University departments, technology centers, etc. (KNOW HOW)
- The knowledge developed by the Company shall be maintained ~~as~~ confidential (confidentiality agreement) during the time agreed. Any publication must also be agreed between parts. (CONFIDENTIALITY)
- Finally, if the innovation developed makes the Company increase its value added. This will serve as a platform to work with the same and other companies (CONTINUED).

Complementarity and mutual trust are key elements for collaboration between innovation agents and companies.

The more than 25 years ~~of~~ collaboration between CENIM and TECNALIA (INASMET) has allowed the improvement of both processes and products manufacturing in the metal industry. Rolling mills for flat and long products of steel have been optimized. Several manufacturers are producing new grades of steel (microalloyed steels, ultra high carbon steels, etc.) or some new formats have been put in the market. Thermomechanical processes of billets and rounds and reinforced bars have been defined. Forging processes in both steel and light alloys (Al, Ti and Mg), have been improved, optimized and characterize. In recent years, among all of these works, our collaboration has been focused on ferritic steels for use at high temperature (heat resistant ferritic steels). In addition, manufacturing processes, heat treatments, microstructural observations and mechanical and creep studies have been performed for their total characterization [1,2,3,4].

Coal is an abundant, low cost resource used for electric power generation; therefore, one of the largest and most reliable energy supplies for many countries in the future will be coal-fired power, together with nuclear power.

Traditional coal-fired power plants, however, emit environmentally damaging gases, such as high levels of CO_2, relative to other electric power generation options. The adoption of ultra supercritical (USC) power plants with increased steam parameters significantly improves efficiency, which reduces fuel consumption and CO_2 emissions [5].

Therefore, the power generation have a renewed interest in high-efficiency coal power plants operating under more severe conditions that the present supercritical power plants. This increase in efficiency is aimed to be reached with the new ultrasupercritical, USC, steam plants which require new materials allowing higher temperature and pressure operation conditions [6]. As an example, increasing the temperature from 540ºC of conventional plants to 650ºC of the supercritical plants makes a gain in thermal efficiency from 39 to 43%.

Ferritic heat resistant steels have been development during the last 10 years due to of their lower prices and lower thermal expansion and larger thermal conductivity compared to austenitic steels. The thermal cycling capabilities of thick section components in a USC plant would be severely restricted by fatigue damage due to thermal stress; however, the creep strength and oxidation resistance of ferritic heat resistant steels are lower than those of austenitic heat resistant steels due to enhanced self-diffusion at elevated

temperature and lower chromium content, respectively. Thus critical issues for the improvement of high efficient, low emission power plants are the enhancement of oxidation resistance as well as creep strength at elevated temperatures.

Under these circumstances, R&D projects of advanced ferritic heat resistant steels have been promoted around the World. In Europe, the COST (Co-operation in the Field of Science and Technology) project has systematically been conducted for advanced ferritic heat resistant steels, such as COST 501 for 600ºC class 9 to 12Cr steels from 1983 to 1997; COST 522 for 625ºC class 9 to 12Cr steels from 1998 to 2003; and COST 536 for 650ºC class 9 to 12Cr steels from 2004 to 2009. Most countries in Europe are currently participating in the COST project. Projects to get temperatures over 620ºC with 9 to 12Cr steels has been development. The next development will be USC plants operating at 30 MPa and 700ºC, could lead to a thermal effciency of 53%.

The research and development of heat resistant steels and alloys for high-efficient USC power plants at 650ºC and above are being now promoted in Japan, USA and Europe, as shown in Figure 1 [5].

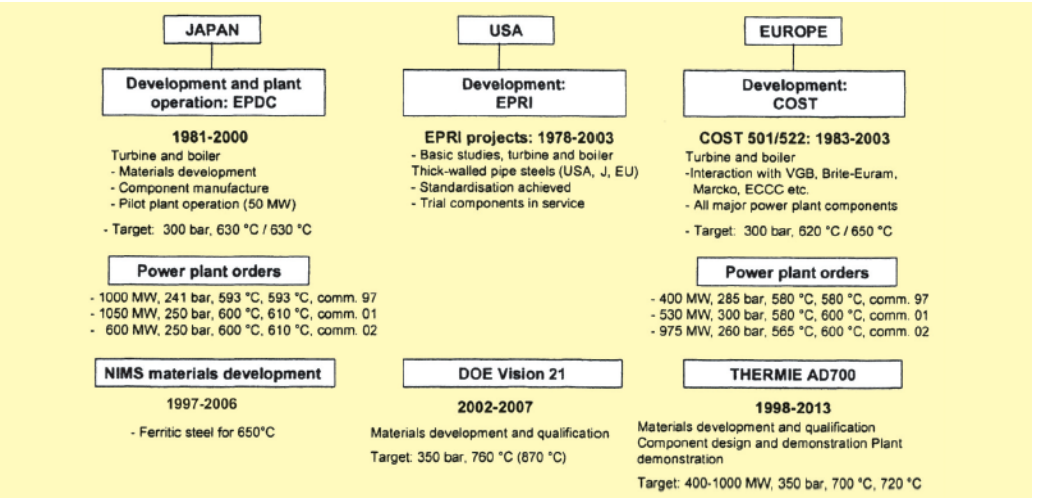

Figure 1. International projects for USC materials.

The work between CENIM-TECNALIA has been focused on the development of ferritic steels containing Cr (HCM2S (2.25Cr-1.6WVNb) <> P/T-23; EN X10CrMoVNb9-1<>P/T-91; NF616 (9Cr-0,5Mo-2WVNb)<>P/T-92) for use at high temperatures in power plants to guarantee a good production quality and

mechanical and creep properties by means of optimization of the manufacturing processes and their implementation it in the Companies. Chemical composition, hot deformation (hot ductility and workability maps), heat treatment processes (CCT diagrams) and metallurgical, mechanical and creep properties (ISOSTRESS and long term tests) on these ferritic steels have been determined. In this paper, however, we will present only same of those aspects: chemical composition, steels position in the Schaeffler-Delong diagram and in the equilibrium diagrams and hot ductility results. In the steel EN X10CrMoVNb9-1<> P/T-91, the optimum rolling conditions and the influence of the chemical composition in the manufacture of seamless tubes without quality problems have also been studied. Moreover, the ductility for different chemical compositions and rolling conditions in the train has been simulated.

2. Experimental Method

2.1. Raw material

Mainly these ferritic steels are used for manufacturing tubes. The material format used for manufacturing the tubes is rounds of different diameters from ingots with a sufficient reduction, greater than 7:1.

2.2. Tubes manufacturing

1. The CPE (Cross-roll Piercing and Elongation) process consists of a sequence of drilling and stretching by cross roller bearings which rotate in the same direction and at the same time, making progress slowly over the head of mandrel, located between the two rollers (punch-bench train). The deformation is performed by cross roller bearings not by the mandrel. The forming process encompasses diameter reduction, piercing, wall thickness reduction and a diameter increase (small and medium size tubes). Afterward the tube is heated and rolled in the stretch reducing mill to the final dimensions.

2. In the Pilger rolling in which the deformation is produced through joint action of a roller and a mandrel up to the final dimensions are achieved. The name pilgrim step rolling mill is because the rolling is not continuous, but the roller has two forward movements after which the tube go back the equivalent of half the advanced and the cycle is repeated until the entire process is

finished. Moreover, the forming roller is not cylindrical and has a parabolic section, which implies an additional compressive stress, similar to a forging (large size tubes).

2.3. Chemical composition

The average chemical compositions of these ferritic steels is shown in Table 1:

Table 1. Chemical compositions of P/T-91; P/T-92 y P/T-23 steels

	%	C	Si	Mn	P	S	Cr	Ni	Mo	V	Nb	N	Al	B	W
■	P/T-91	0,10	0.41	0.38	0,012	0,006	9.02	0,09	1,0	0,22	0,073	0,044	0,019	0.000	0,00
■	P/T-92	0.096	0.39	0.43	0.017	0,003	9,00	0.12	0.45	0.20	0.080	0.050	0.026	0.003	1.75
■	P/T-23	0.080	0.35	0.40	0.015	0.005	2,25	0,00	0,20	0.25	0.050	<0.03		0.003	1.60

2.4. Schaeffler-Delong diagram

The position of these steels in the Schaeffler-Delong diagram is indicated in Figure 2:

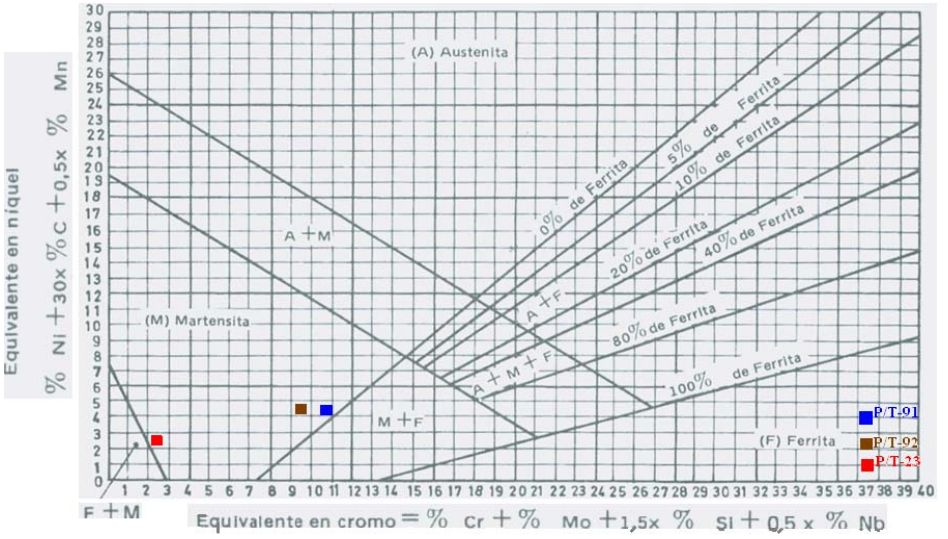

Figure 2. *Schaeffler-Delong* diagram. Position of steels.

As can be seen both in the steels P/T-91 as P/T-23 are near the area of appearance of ferrite, even P/T-92 steel.

2.5. Equilibrium diagrams

To better understand the influence of the carbon content and the content of Cr, (Mo is taken as Cr) we will use the Cr-Tª equilibrium diagrams for carbon weight percent of 0.10 and 0.05%. The positions of the three types of ferritic steels studied are indicated by colored bars. The diagrams show that the P/T-91 and P/T-92 steels (specially the first one) can transform a certain amount of delta ferrite at the austenitizing temperature of 1225 to 1275°C for the case of chemical composition steels with the highest carbon (0.10%C). The transformation to ferrite is produced to lower temperatures (900-1120°C) for the lower carbon compositions (0.05%C) (Figure 3).

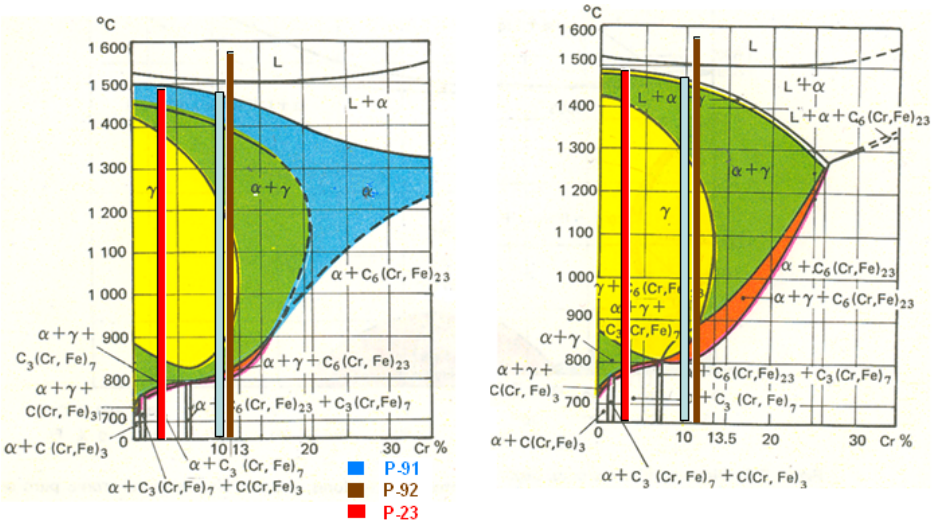

Figure 3. Steels position in *Fe-C* equilibrium diagram for *C=0.05 y 0.10%*[6].

3. Results and discussion

3.1. Hot ductility

A hot ductility study was carried out by hot torsion, hot tensile and hot compression. The latter two were tested in the Gleeble system, simulating the minimum and maximum deformation rate of the tube manufacturing process.

Parameters

- T ª s (°C): 850 °C-950 °C-1050 °C-1150 °C-1200 °C-1275 °C-1350 °C
- Time residence: 21 min / inch (total test time 300 s).
- Deformation rate ε = 2 s^{-1} and 10 s^{-1} (minimum and maximum calculated in the rolling bank).

Curves of hot ductility- Reduction of Area (RA) after hot tensile tests of P/T-23 steel, P/T-92 and P/T-91 steels, at two deformation rates, are shown in Figure 4:

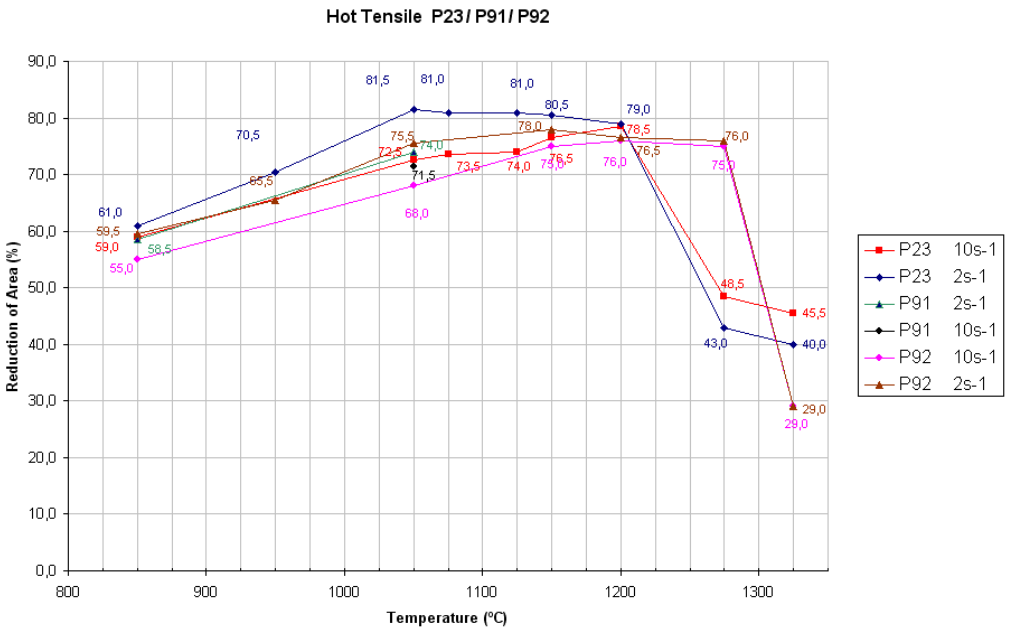

Figure 4. Hot ductility (reduction of area) of GLEEBLE tensile tests for P/T-23, P/T-91 and P/T-92 steels at two deformation rates.

Figure 4 shows that the largest hot ductility is for the P/T-23 steel. This ductility is better than that obtained for the P/T-92 steel and even better than the ductility of steel P/T-91. The P/T-92 steel has the highest ductility at highest temperatures. At lower strain rates, the ductility is better in all the cases.

For comparison, Figure 5 shows-the different parameters that can be obtained from the three main methods for determining the hot ductility: Torsion

(number of turns), tensile (area reduction-RA (%)) and compression (ε-reduction) for the three types of steels studied.

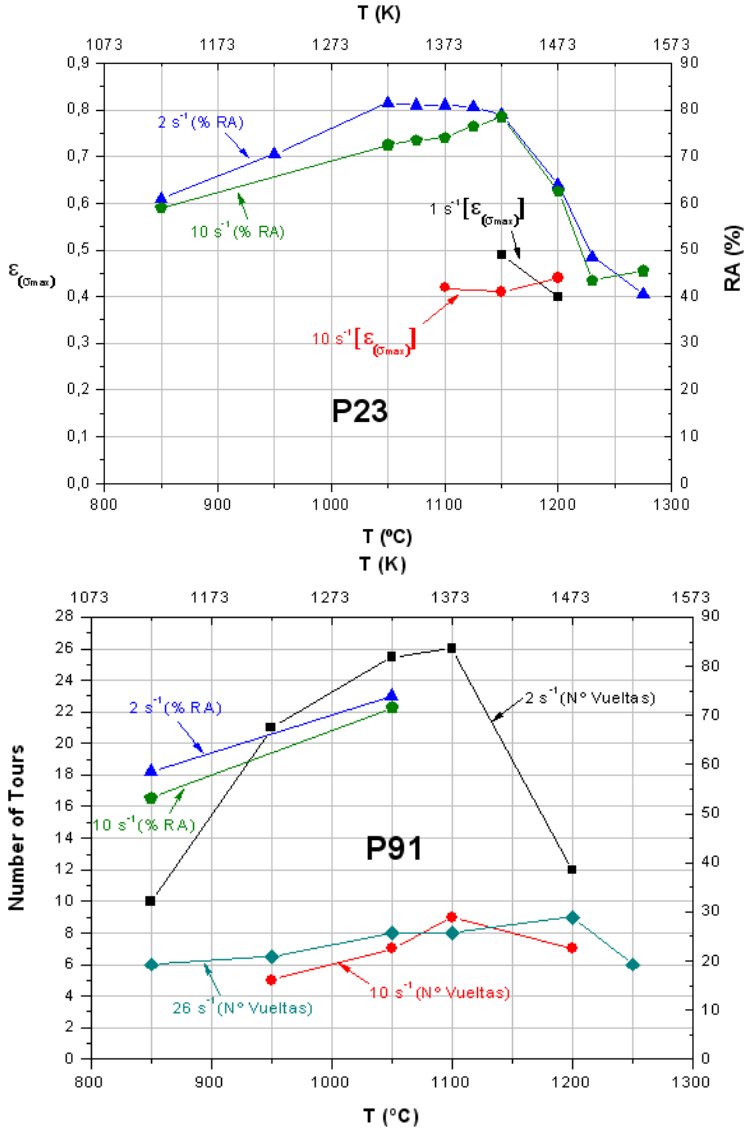

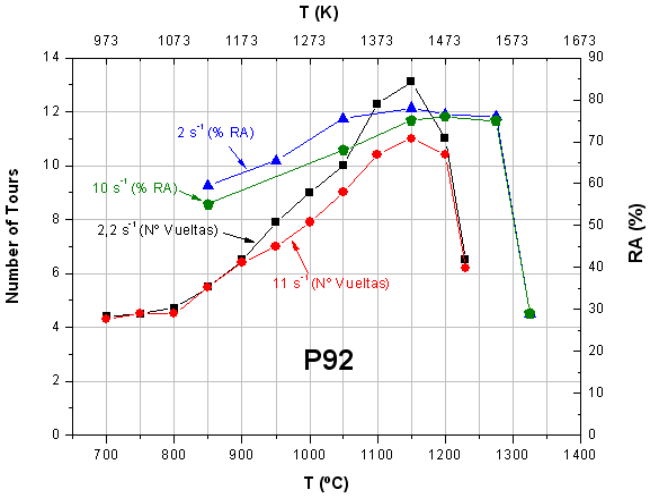

Figure 5. Comparison of hot tensile test (RA-%), torsion (number of turns) and compression (ε) of P/T23-P/T91-P/T92 steels (2 deformation rates).

From Figure 5, it can be deduced that the tensile and torsion tests are the best defining the hot ductility. In contrast, hot torsion shows greater sensitivity of the ductility with test temperature. For both tests the sensitivity of the tests with respect to the strain rate is very similar. The hot compression does not reflect so adequately the hot ductility.

As an example, we will show the main industrial problems resolved in the case of P/T-91 steel: the cracks formed, Figure 6, during tube rolling of heat B (not in heat A) in the stretch reducing mill.

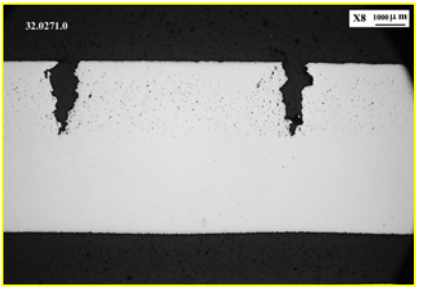

Figure 6. Tube defects in the heat B.

Two heats of the P/T-91 steel (heats A and B) with chemical composition in Table 2, were studied:

Table 2. Chemical compositions of P/T-91 steel (heats A and B).

P91	C	Mn	Si	P	S	Cr	Ni	Mo	V	Nb	N	Al	Cu	Ti
A	0,11	0,49	0,25	0,010	0,005	8,22	0,30	0,91	0,21	0,078	0,0490	0,015	0,017	0,003
B	0,11	0,38	0,30	0,011	0,006	9,06	0,10	1,01	0,23	0,08	0,0410	0,019	0,018	0,003

The seamless tubes were rolled for these two heats by CPE process. The rolling maximum parameters in the train were (converted in strain and strain rate) ε = 0.078 and έ = 11.4.

For these heats the Chromium-Nickel balance CBN [7, 8] obtained by the expression:

CNB = Cr +6 Si +4 Mo +1.5 W +11 V +12 Ti +5 Nb +9 Al-40C-30N-4Ni-2Mn-1Cu, were:

CNB (Heat A) = 8.38 -% C = 0.107. In this case the response to the tube rolling was good (no cracks observed).

CNB (Heat B) = 11.79-% C = 0.106. In this case the response to the tube rolling was bad (cracks observed).

After the study of hot ductility (hot torsion) some differences were found Figure 7.

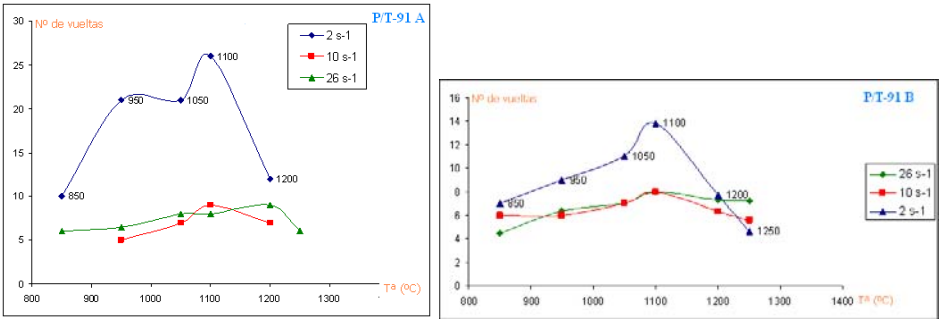

Figure 7. Hot ductility for heats A and B (torsion tests).

As we can see in Figure 7, the heat A has better hot ductility than the heat B, but these differences are almost negligible at high strain rates.

The metallography examination of the raw material and the tube after punch-bench train showed that delta ferrite bands were in both two samples of heat B (Figure 8).

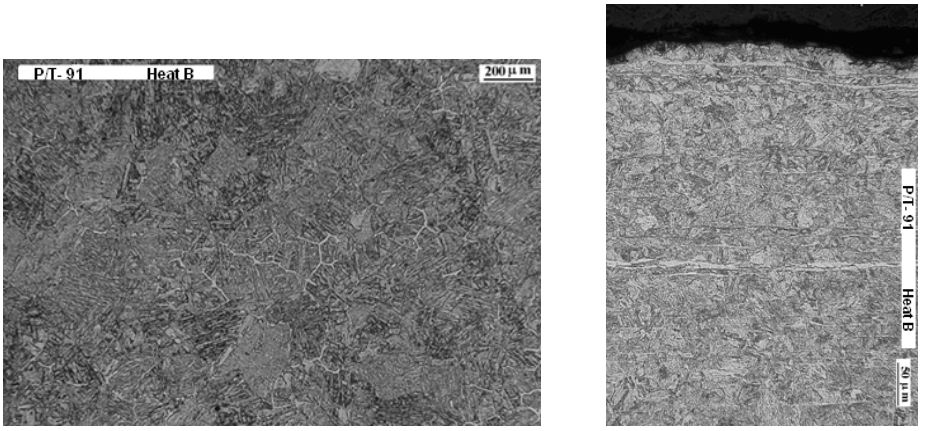

Figure 8. Delta ferrite in the raw material and punch-bench tube in the heat B.

Some early breakages in the delta ferrite bands of the punch-bench tubes of the heat B are observed (Figure 8). Delta ferrite has less hot ductility and is necessary to be eliminated from the P/T 91 microstructure in order to avoid cracks during tube rolling. The tube reheating temperature and deformation conditions in the stretch reducing mill were simulated by means of hot torsion tests in heat A and B.

The study of the microstructures of these heats shows that the delta ferrite is formed at 800°C and only disappears completely in heat B after maintenance at 1050°C [8]. Some isolated grains remains at 1000°C.

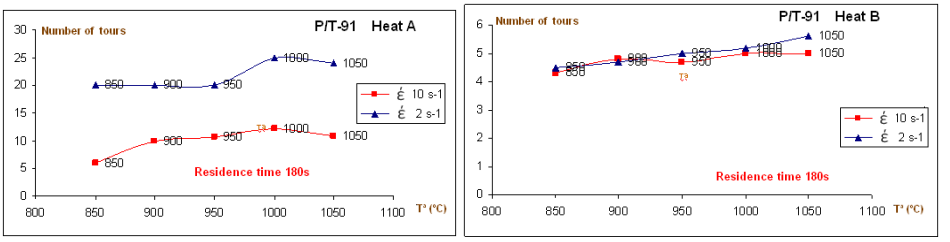

Figure 9. Hot ductility in stretch reducing mill for heats A and B (residence time 180s).

Torsion tests to rupture were preformed in heats A and B (Figure 9) with these parameters: Preheating at 1250°C (residence time 7 min-30 min per inch) and cooling to 650°C to simulate the punch-bench train. Afterward, this torsion test specimen is reheated at different temperatures: 850ºC to 1050ºC [residence

time of 60s (4.3 min per inch) and 180s^{-1} (12.7 min per inch)] with strain rates of ἐ = 2 and 10 s^{-1} in order to simulate the stretch reducing mill.

As observed in Figure 9, the heat A has much better hot ductility than the heat B at low strain rates (2 s^{-1}). The hot ductility differences are not negligible at high strain rates (10 s^{-1}) due to the presence of delta ferrite in heat A.

The influence of the residence time in hot ductility is shown in Figure 10.

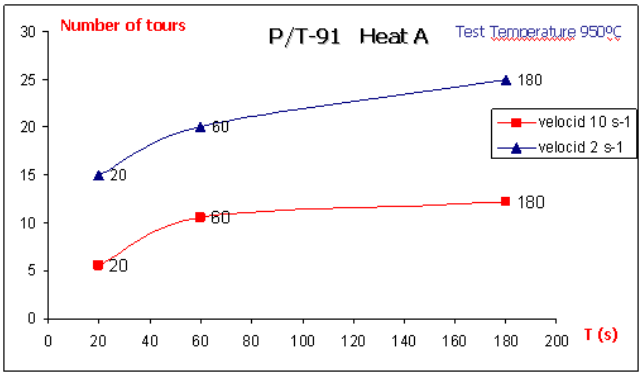

Figure 10. Influence of residence time in the furnace of the stretch reducing mill in the hot ductility.

Delta ferrite has been eliminated at temperatures of 950ºC with stretch reducing mill furnace residence time of 180s.

Both the temperature and residence time in the furnace of the stretch reducing mill will be one of the keys for reducing the tubes defects. However the chemical composition is the main key for elimination of the cracks in the P/T-91 tubes having a CNB value of less than 9.

4. Conclusions

1. The main keys to participate in innovation projects of companies are quick assimilation of innovation by the industry, added value and confidentiality.

2. Tensile and torsion tests are the best tests to define the hot ductility. The hot torsion tests show greater sensitivity for determine the variation of ductility with temperature. In both tests, tensile and torsion, the sensitivity of them with respect to the strain rate is adequate. The hot compression does not reflect adequately the hot ductility properties. But is with the torsion test one of the best method to study the conformation maps

3. Industrial problems should be studied with a deep knowledge of the industrial processes. For the cracks problem in the T/P-91 steel, the chemical composition is the main key for their elimination. CNBs lower than 9 should be enough to eliminate the cracks problem. Both temperature and residence time in the furnace of the stretch reducing mill will be also other main factor for reducing the tubes defects.

5. References

[1] M. Carsí, R. Allende, F. Peñalba, J.A. Jiménez , O.A. Ruano , "Simulation of the Forming Behavior of a Boron Modified P91 Ferritic Steel", Steel Research Int. 75 (2004) 26-32.

[2] F. Peñalba, X. Gómez, R. Allende, M. Carsí, O.A. Ruano, "Mechanical properties and forming behavior of a type 9%Cr steel containing 2%W", Mater. Sci. Forum 638-642 (2010) 3128-3133.

[3] M. Carsí, F. Peñalba, I. Rieiro, O. A. Ruano "High temperature workability behaviour of a modified P92steel " Int. J. Mater. Res. (formerly Z. Metallkd.) 102 (2011). Pages 1378-1383.

[4] F. Peñalba, J. Umbelina, M.Carsí, M.T. Larrea,O.A. Ruano, R.Allende. "Aceros experimentales tipo 9% Cr modificados con W y B. Propiedades mecánicas" Tube´01 (International Tube Association). Proc. Pages 1-11. Bilbao Oct.2001.

[5] R. Viswanathan, R. Purgert, S. Goodstine, J. Tanzosh, G. Stanko, J.P. Shingledecker, B. Vitalis, Proc 5th Int Conference on Advances in Matererial Technology for Fossil Power Plants, EPRI, 2008, p. 1.

[6] A. Inchaurza. "Aceros inoxidables y aceros resistentes al calor: Propiedades, transformaciones y normas". Limusa. Mexico. 1981.

[7] L. Cipolla, A. Di Gianfrancesco, S. Caminada, G. Cumino. "Production Experience of Tenaris-Dalmine Grades 91 and 23: microstructure, mechanical properties and creep behaviour". ETD Seminar. London Jun. 2007

[8] http://www.docstoc.com/docs/27174168/ANALYSIS-OF-EFFECT-OF-CHEMICAL-COMPOSITION-ON-HOT-FORMING

[9] F.Peñalba, M.Carsí, O. A. Ruano. Informe privado. San Sebastian 2011.

6. Acknowledgements

This work was supported by Project MAT2009-C02-C01

International Symposium on Plastic Deformation and Texture Analysis
Alcoy (Spain) 24-25 September 2012
119-124

Controversial aspects of deformation at high temperature

O.A. Ruano

Department of Physical Metallurgy, CENIM-CSIC, Av. Gregorio del Amo 8, Madrid 28040, Spain

Abstract

A large amount of creep data at various temperatures and strain rates have been obtained in a large variety of pure metals and alloys. Rationalization of these data to determine the controlling mechanism of deformation is however difficult because various factors affect the creep behaviour that can be explained on hand of various models. This give rise to strong controversies present in the literature that obscure the comprehension of the creep phenomena. This work considers seven controversial aspects that have been present in the research work of the present author. These are the following: thermodynamics of creep versus diffusion controlled creep, interpretation of creep data assuming a power law versus a hyperbolic sine, law, diffusional creep as a mechanism controlling deformation, the presence of a threshold stress to rationalize creep data, grain boundary sliding controlled by dislocation movement, cooperative versus single grain boundary sliding, and solute drag creep as a mechanism showing large elongations.

Resumen

Se ha obtenido una gran cantidad de datos a la fluencia, a diversas temperaturas y velocidades de deformación, en una gran variedad de metales puros y aleaciones. La racionalización de estos datos para determinar el mecanismo de control de la deformación es, sin embargo, difícil a causa de diversos factores que afectan el comportamiento de fluencia, que puede explicarse, en parte, con diversos modelos. Esto da lugar a fuertes polémicas presentes en la literatura que oscurecen la comprensión de los fenómenos de fluencia. Este trabajo considera siete aspectos controvertidos que han estado presentes en el trabajo de investigación del autor de este artículo. Estos son

los siguientes: termodinámica de fluencia versus fluencia controlada por difusión, la interpretación de los datos de fluencia suponiendo una ley de potencia frente a un seno hiperbólico, la fluencia difusional como un mecanismo de control de la deformación, la presencia de una tensión umbral para racionalizar los datos de fluencia, el deslizamiento en frontera de grano controlado por movimiento de dislocaciones, deslizamiento en frontera de grano cooperativo versus simple, y arrastre de soluto por fluencia como un mecanismo que muestra grandes alargamientos.

Keywords: creep, deformation mechanisms, threshold stress, diffusional creep, superplasticity.

Palabras clave: fluencia, mecanismos de deformación, tensión umbral, fluencia difusional, superplasticidad.

1. Introduction

Fundamental and experimental studies on the creep behavior of materials have been strongly pursued over the last century. Extensive experiments at high temperature of coarse grain materials reveal that the experimental activation energy for creep is about equal to the respective activation energy for volume self-diffusion providing that the determination is carried out in the steady state. This suggests that creep is controlled by dislocation climb, a mechanism that usually shows a stress exponent, n, of five or higher. In fine grained materials, usually less than 10 μm, other deformation mechanisms come into play being grain boundary sliding and diffusional (Nabarro-Herring and Coble) creep, with $n<2$, the most likely to control deformation.

However, many factors come into play that obscure this simplified vision of creep, creating a controversy that is reflected in the literature. This controversy is usually related to the presence of solutes and threshold stresses, changes in the microstructure during deformation, dynamic recrystallization, extremely high strain rates and competing mechanisms in a giving range of testing temperatures and strain rates.

In this presentation seven controversial aspects of deformation at high temperature are presented and discussed. These have been present in the scientific work of the groups where I have been involved. They are the following:

2. Thermodynamics of creep versus diffusion controlled creep

The shear strain rate can be described as a function of an activation enthalpy for creep and an activation volume for creep that is equal to the activation area multiplied by Burgers vector [1]. Although this is a low temperature concept, it is applied also to high temperatures [2]. The interpretation of creep data is opposed to the description made assuming atomic diffusional processes, although both interpretations involve dislocation motion.

3. Interpretation of creep data assuming a power law versus a hyperbolic sine law

Creep data usually show a breakdown of the power law at high strain rates and low temperatures. The interpretation of creep data at different temperatures can be made assuming various power law equations with different stress exponents or assuming a single hyperbolic sine, Garofalo, equation. This last concept can be extended assuming a hyperbolic sine equation as description of the creep behavior of materials at any temperature and any strain rate range. This equation can be applied to a wider range of temperatures and strain rates and therefore its predictive capability is more precise than that assuming a set of power laws [3].

4. Diffusional creep as a mechanism controlling deformation

Diffusional creep is a mechanism observed at low strain rates and high temperatures in fine grain materials and is based in the mass transport of atoms through the grains (Nabarro-Herring creep [4,5]) or along the grain boundaries (Coble creep [6]). The occurrence of precipitate denuded zones has been considered a proof of this deformation mechanism [7]. The existence of diffusional creep has been questioned based on a discrepancy between the predicted and experimental strain rates and also between the measured and predicted size of the denuded zones [8,9].

5. The presence of a threshold stress to rationalize creep data

A number of reinforced materials show creep data approaching asymptotically a single stress at high temperatures and low stresses. This is named threshold stress and indicates that measurable creep does not occur below this stress or,

in other words, that the creep mechanism do not operate below this stress [10,11]. This concept can be applied to any creep mechanism but its existence must be inferred from indirect experimental evidence, which includes assumption of a given mechanism and in many cases is a strong function of temperature and grain size which means that not a single threshold stress but a number of threshold stresses are assumed. These stresses are difficult to be physically rationalized [12,13].

6. Grain boundary sliding controlled by dislocation movement

It is widely accepted that grain boundary sliding is the deformation mechanism responsible of the superplastic behavior of fine-grained materials deformed at relatively low strain rates and high temperatures [14,15]. The texture is assumed to become weaker with deformation assuming this mechanism. Some controversy exists because the texture and microstructure changes are not consistent with relative grain translation via boundary sliding. Instead of grain boundary sliding, a combination of rate-sensitive slip and dynamic grain growth is proposed to explain the creep behavior [16].

7. Cooperative versus single grain boundary sliding

The precise mechanism of grain boundary sliding is a matter of controversy in superplasticity. Opposed to the concept of sliding between the boundary of single grains, there is also in the literature the concept of cooperative action of a number of grains following the direction of the maximum shear stress building shear bands [17]. In other words, sliding occurs non-uniformly along grain boundaries, while main deformation occurs along the boundaries that cover several grains and therefore bands are observed from the localized displacement of a group of grains [18]. Numerous evidence for both concepts is presented in the literature.

8. Solute drag creep as a mechanism showing large elongations

Large elongations and low stress exponents characterize the creep behavior of materials containing solutes that are controlled by the solute drag of dislocations [19,20]. This behavior may be erroneously attributed to grain boundary sliding and therefore it has been proposed a new definition of superplasticity as (i) elongations of "at least 400%" and (ii) materials having "a

measured strain rate sensitivity close to about 0.5 (n=2)" [21]. In this controversial definition grain boundary sliding is not mentioned, either a randomization of the texture with deformation or a dependence of strain rate with grain size which is [22].

9. References

[1] S.V. Raj, J. Mater. Sci., 24 (1989) 3196.

[2] O.A. Ruano, G. Elssner, J. Less Common Met., 40 (1975) 121.

[3] I. Rieiro, M. Carsí, O.A. Ruano, Mater. Sci. Technol., 25 (2009) 995.

[4] F.R.N. Nabarro, In: Report of conference on the soils. London: The Physical Society, 1948. p. 75.

[5] C. Herring, J Appl. Phys., 21 (1950) 437.

[6] R.L. Coble, J. Appl. Phys., 34 (1963) 1679.

[7] R.L. Squires, R.T. Weiner, M. Phillips, J. Nucl. Mater., 8 (1963) 77.

[8] O.A. Ruano, J. Wadsworth, J. Wolfenstine, O.D. Sherby, Mater Sci. Eng. A, 165 (1993) 133.

[9] O.A. Ruano, O.D. Sherby, J. Wadsworth, J. Wolfenstine, Scripta Mater., 38 (1998) 1307.

[10] R.W. Lund, W.D. Nix, Acta Metall., 24 (1976) 469.

[11] F. Carreño, O.A. Ruano, Acta Mater., 46 (1998) 159.

[12] J.A. del Valle, O.A. Ruano, Rev. Metall. Madrid, 46 (2010) 71.

[13] A. Yawny, G. Eggeler, Mater. Sci. Eng. A, 387–389 (2004) 905.

[14] O.A. Ruano, A. Miller, O.D. Sherby, Mater. Sci. Eng., 51 (1981) 9.

[15] O.A. Ruano, O.D. Sherby; Rev. Phys. Appl., 23 (1988) 625.

[16] P.S. Bate,F.J. Humphreys, N. Ridley, B. Zhang, Acta Mater., 53 (2005) 3059.

[17] O.A. Kaibyshev, A.I. Pshenichnyuk, Mater. Sci. Eng. A, 410–411 (2005) 105.

[18] N.A. Maraa, A.V. Sergueeva, T.D. Marab, S.X. McFadden, A.K. Mukherjee Mater. Sci. Eng. A 463 (2007) 238.

[19] E.M. Taleff, G.A. Henshall, T.G. Nieh, D.R. Lesuer, J. Wadsworth, Metall. Mater. Trans. A, 29 (1998) 1081.

[20] J. Qiao, E.M. Taleff, Trans. Nonferrous Met. Soc. China, 20 (2010) 564.

[21] T.G. Langdon, J. Mater. Sci., 44 (2009) 5998.

[22] C.M. Cepeda-Jiménez, J.M. García-Infanta, O.A. Ruano, F. Carreño, J. Alloys Comp., 2012, in press.

10. Acknowledgements

During my 42 years of research in the field of mechanical properties of materials, I received an enormous amount of help from a lot of people. I want to acknowledge my mentors, colleagues and students for their support and especially for their friendship and loyalty. Without their contribution, not only would this work not be possible but it would not be worthwhile.

International Symposium on Plastic Deformation and Texture Analysis
Alcoy (Spain) 24-25 September 2012
125-134

Recrystallization mechanism in Fe20Cr6Al ODS alloy

G. Pimentel[1], C. Capdevila[1], J. Chao[1] and V. Amigó[2]

[1]Grupo Materalia, Centro Nacional de Investigaciones Metalúrgicas (CENIM-CSIC), Avda. Gregorio del Amo 8, 28040 Madrid, Spain

[2]ITM, Universitat Politècnica de València, Camino de Vera s/n, 46022 Valencia, Spain

Abstract

The yttria dispersion in ODS Fe-Cr alloys improves the high-temperature creep and stress rupture life. The creep strength is further enhanced by the development of a coarse-grained microstructure during recrystallization. Factors controlling the evolution of this desirable microstructure are explored in this work, focusing specifically on PM 2000.

EBSD analysis has been used to identify the changes during recrystallization. Before the coarse grain takes place, the alloy undergoes a continuous recrystallization process followed by an abnormal grain growth process. As the secondary recrystallization interface travels further down the specimen, the grain size and the proportion of 'special' boundaries both increase. The initial strong (110) fibre texture is transformed into textures lying on the (112) zone axis.

It has also been studied the role of compression strain on the development of recrystallized grain structure. In this sense, the induced deformation lead to more refined and more isotropic grain structures. Furthermore recrystallized grains no longer have a preferred growth orientation.

Resumen

La dispersión óxidos de itrio en las aleaciones ODS Fe-Cr mejora la resistencia a fluencia a alta temperatura y el tiempo de vida a rotura por estrés. El desarrollo, durante el proceso de recristalización, de una microestructura de grano grueso refuerza dicha resistencia a la fluencia. En este trabajo se

estudian los factores que controlan la evolución de esta microestructura centrándose específicamente en la aleación PM 2000.

Mediante análisis de EBSD se han identificado los cambios producidos durante la recristalización. Previa a la formación del grano grueso, la aleación experimenta un proceso de recristalización continua seguido por un proceso de crecimiento de grano anormal. Mientras el frente de recristalización secundaria avanza, tanto el tamaño de grano como la cantidad de límites de grano 'especiales' aumenta. La marcada textura de fibra inicial (110) se transforma en orientaciones situadas en el eje de zona (112).

También se ha estudiado el efecto de deformaciones por compresión en el desarrollo de la estructura de grano recristalizado. En este sentido, la deformación conduce a microestructuras de grano más fino e isotrópico. Además los granos recristalizados dejan de tener una orientación preferencial de crecimiento.

Keywords: ODS alloy, mechanical alloying, continuous recrystallization, texture, abnormal grain growth.

Palabras clave: Aleación ODS, aleado mecánico, recristalización continua, textura, crecimiento anormal de grano.

1. Introduction

ODS alloys are manufactured by mechanical alloying (MA), process in which powders of the alloy components were deformed until they form a solid solution with a fine grain structure [1]. Their high temperature resistance is due to the yttria nanometric size. Recrystallization process in ODS alloys is mainly characaterized by the great differences between the as-deformed and recrystallized states. As the deformed state presents a sub-micrometer grain size, the recrystallization process leads the formation of large columnar grain microstructures[2]. Moreover, the ODS recrystallization temperature is exceptionally high which implies homologous temperatures (ratio between temperature and melt temperature) the order of 0.9 [3].

The aim of this study is to characterize the middle stages recrystallization process from the sub-micrometer grain size to the abnormal grain.

2. Experimental Method

The material was provided by PLANSEE GmbH. The alloy is commercially named PM 2000 and has the nominal composition Fe-20Cr-6Al-0.5Ti-0.5Y_2O_3 (in wt.-%). After mechanical alloying, the powder is consolidated by hot isostatic pressing (HIP) and then formed into tubes by hot extrusion. The extruded tube was then further hot-rolled at 900 ^{o}C, and finally, cold rolled.

Cylindrical samples of about 10x4mm were cut from the as-receive tube to study the microstructural evolution during the recrystallization process and were subjected to different isothermal heat treatments at 1350 °C. After heat treatments both longitudinal and cross sections of the treated samples were prepared for the study by TEM [4] (JEOL JEM-200 CX), SEM and EBSD [4] (FEG-SEM JEOL JSM-6500F). To study the deformation effect on the recrystallization process two samples were deformed by compression in order to reduce their shape by 10%. One of them was heat treated for one hour at 1350 ^{o}C. The otherone was taken as reference. Both were prepared [4] for the study by EBSD. The EBSD patterns were generated at an acceleration voltage of 20KV and collected using a CRYSTAL detector of Oxford Instruments mounted in a SEM JEOL JSM6300. The indexation of the Kikuchi lines and the determination of the orientations were done with the software INCA developed by Oxford Instruments. The results were represented by means of an inverse pole figure (IPF) maps, which give the orientation of a macroscopic direction with respect to a specific crystal direction.

3. Results and discussion

3.1. As-received state

In the as-received state the microstructure consists of elongated grains along the longitudinal direction. As it is shown in figures 1 a) and b), the grains have a high grain aspect ratio (GAR) and are 3-4 μm in length and diameter 0.5 μm.

Well define grain morphology, as well as the absence of a strain cell structure (Fig. 2a) lead to the conclusion that the material has suffered dynamic-recovery process during the manufacturing and therefore the as-received microstructure corresponds to a grain themselves microstructure and not to a deformation structure, as have made clear in several communications [5-6].

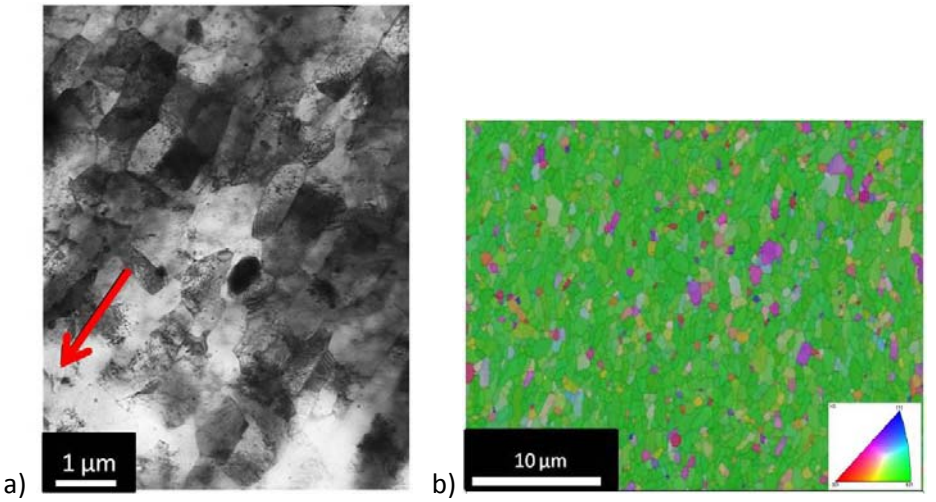

Figure 1. PM 2000 as-received state a) TEM micrograph of the longitudinal section, b) IPF map of the cross section. Red arrow indicates the rolling direction.

Such grains are formed by subgrains separated by low angle grain boundaries (LAGB) as can be seen in Figure 2b. EBSD texture analysis (Figure 1b) shows the presence of <110>||RD fiber texture. Such as texture normally is found in materials deformed, whether extrusion or rolling, with BCC structure [7].

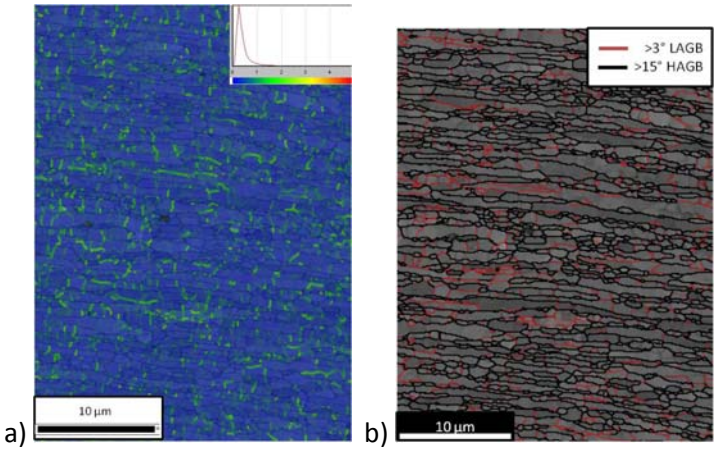

Figure 2. Longitudinal section a) Kernel-map, b) grain boundary localitation: red lines correspond to LAGB and black with HAGB.

3.2. Continuous recrystallization

From the as-received state the material was subjected to a heat treatment at 1350 °C without maintenance over time, in that case no significant microstructural changes were observed. As shown in Figure 3a, the thermal activation means, only a slight grain thickening. Greater treatment times imply the morphological change of the grains from elongated to equiaxial morphology (Figure 3b). Equiaxial grains growth until abnormal grain growth takes place (Figures 3c and 3d).

During the treatment time the initial high GAR decreases progressively. B. Ralph et al. [9] indicate that the decrease in grain elongation is due to not only the restoration of the equiaxial geometry (closer to the equilibrium geometry) but also the rapid subgrain growth.

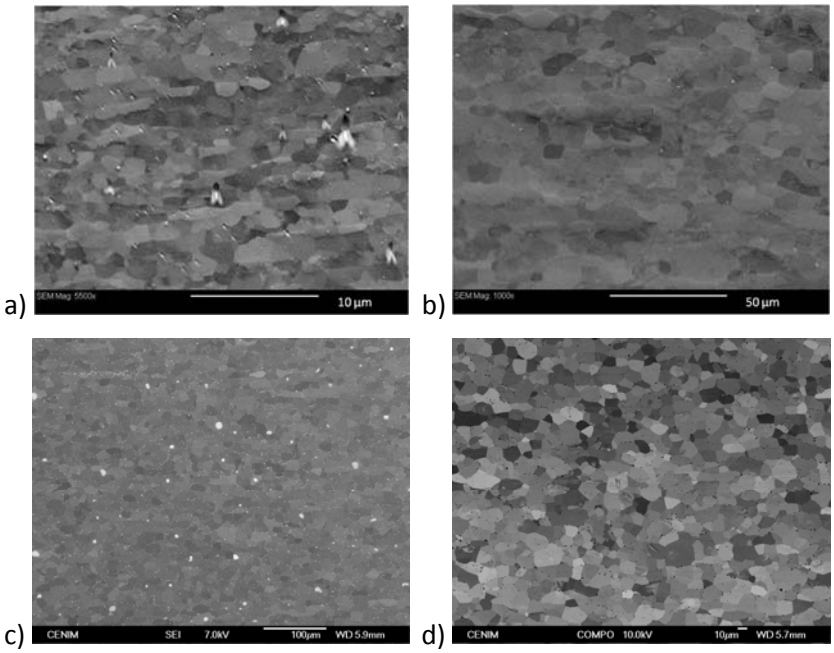

Figure 3. SEM micrographs of the longitudinal section after 1350 °C heat treatments a) without maintenance in time, b) 6, c) 15 and d) 20 minutes.

Of all the treatments performed five times representative of each stage were taken to analyze, by EBSD, the texture and grain boundaries types. Figure 4 shows IPF maps and grain boundary type. It could be concluded that

microstructural evolution doesn't imply LAGB disappearance. Also there is no significant evolution in the material texture.

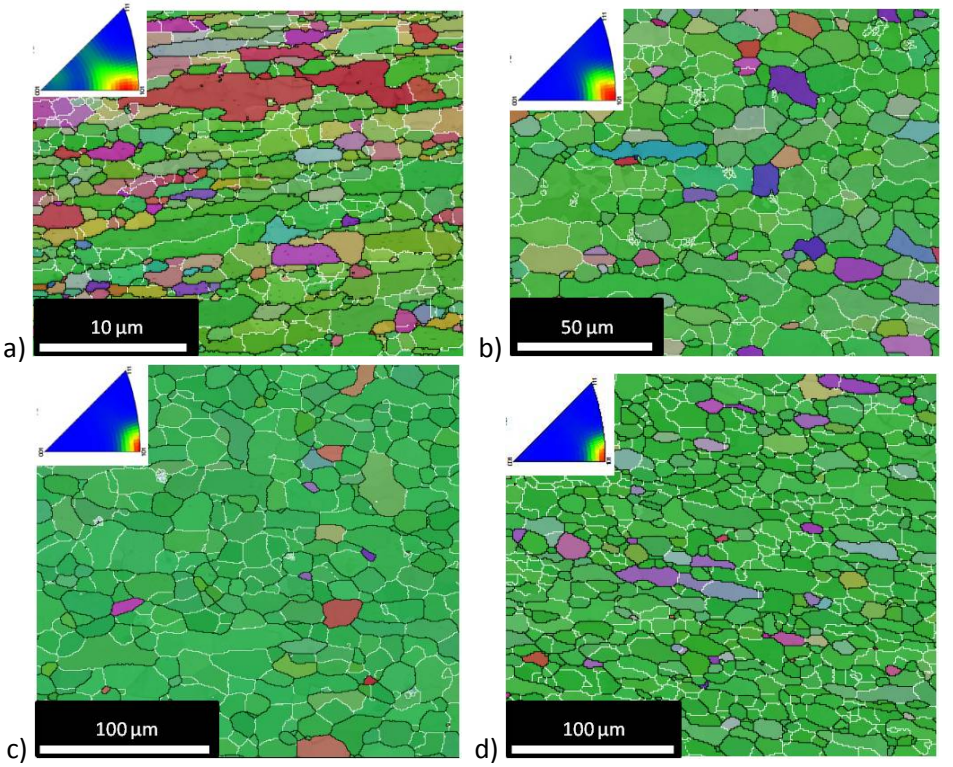

Figure 4. IPF maps and grain boundary type (in white LAGB and in black HAGB) a) without maintenance in time, b) 6, c) 13, d) 15 and e) 20 minutes.

Both features are consistent with the description of a continuous recrystallization process in which predominates subgrain boundary movement (whether subgrain migration or coalescence) which means (and justifies) the deformation texture is not altered [10-11 - 12].

3.3. Abnormal grain growth

Finally, as can be seen in figure 5, equiaxial grained microstructure is lost in favor of elongated (along the rolling direction) and coarse-grained one (the order of mm).

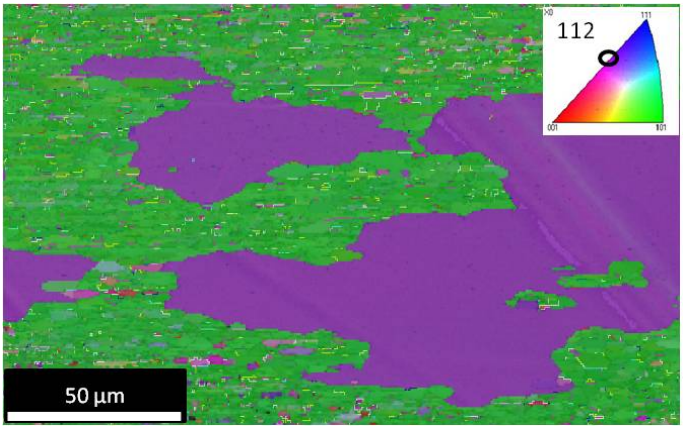

Figure 5. IPF map.

Abnormal grain growth implies selective growth of grains which were present in the initial microstructure and orientations between (100)-(111). More precisely close to (112). Therefore, it could be said that there is a preferential texture of abnormal grain growth which consumes the remainder matrix at the expense of the other orientation (110) [13].

3.4 Deformation effect

Figure 6a shows the effect of 10% reduction on superficial area due to a compression along the axial direction. Compared with the IPF map shown in figure 1b it could be concluded that deformation causes a change in texture consisting of the increasing number of grains with orientations close to (112) parallel to rolling direction, which is consistent with previous publications [14].

The compression along the axial direction also affects the grain boundary distribution. Compared with figure 2b, the deformation causes a decrease of LAGB number and an increase of the HAGB number.

After the 1h heat treatment at 1350 ^{o}C, the induced deformation lead to more refined and more isotropic grain structures as is clearly shown in figure 7a. Furthermore recrystallized grains not only don't have the preferred growth orientation close to (112), but also they don't have any preferred growth orientation (figure 7b).

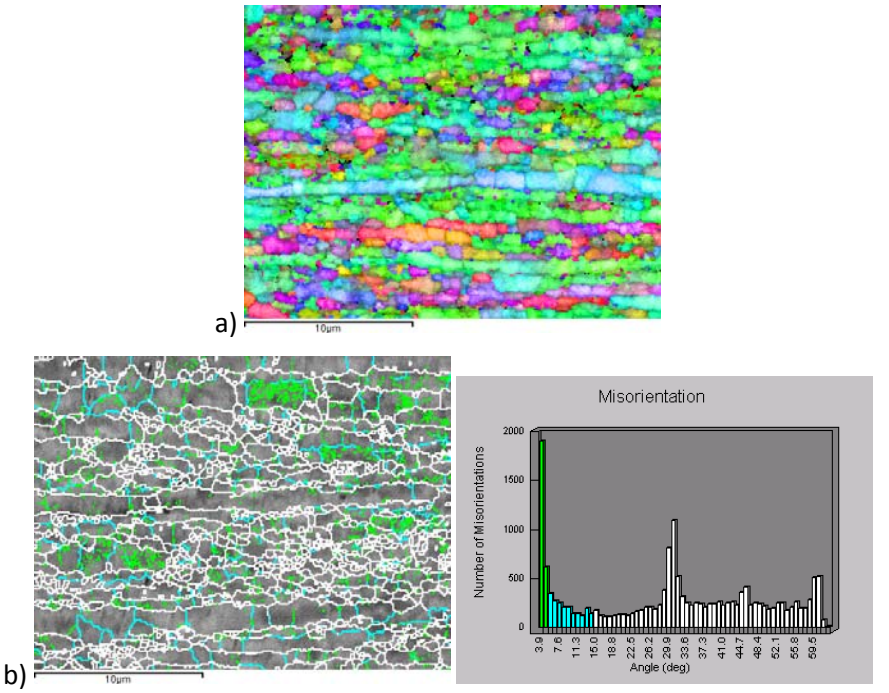

Figure 6. 10% superficial area reduction sample a) IPF map b) grain boundary localization (green less than 5^{o} misorientation angle, blue LAGB and white HAGB).

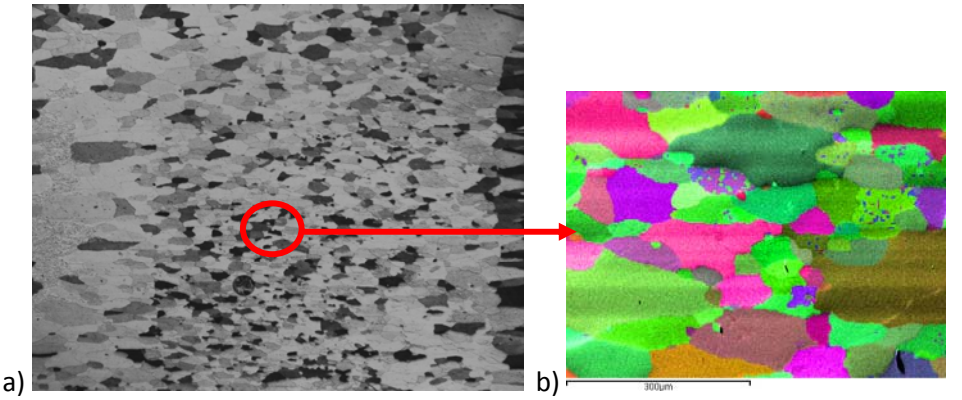

Figure 7. a) Optical micrograph after 1h heat treatment at 1350 ^{o}C of sample 10% compression deformed, b) IPF map of the region inside the ring.

4. Conclusions

In the PM2000 recrystallization process it could be differentiated two stages. During the first one a continuous recrystallization process takes place and it is featured by a geometrical change in grain structure with no significant change in material texture. During the second stage the abnormal growth of grains with orientations closet o (112) takes place.

Compression strains induced more texture heterogeneity and less low angle grain boundaries which implies finer recrystallization microstructures and no preferred growth orientation.

5. Bibliography

[1] C. Capdevila and H.K.D.H. Bhadeshia, *Advance Engineering Materials*, 5 (2003) 232.

[2] J. S. Benjamin, *Metallurgical and Materials Transactions*, 1 (1970) 2943.

[3] H.K.D.H. Bhadeshia, *Materials Science and Engineering A*, 223 (1997) 64.

[4] C. Capdevila, M.K. Miller, G. Pimentel and J. Chao, *Scripta Materialia*, 66 (2012) 254.

[5] C. Capdevila, Y. L. Chen, A. R. Jones and H.K.D.H. Bhadeshia, *Isij International*, 43 (2003) 777.

[6] C. Capdevila, U. Miller, H. Jelenak and H.K.D.H. Bhadeshia, *Materials Science and Engineering A*, 316 (2001) 161.

[7] D. Raabe, K. Luecke, *Materials Science Forum*, 157 (1994) 597.

[8] M. Klimiankou, R. Lindau, A. Möslang and J. Schröder, *Powder Metallurgy*, 48 (2005) 277.

[9] B. Ralph, K. J. Kurzydtowski, A. Chojnacka, *Journal of Materials Science*, 29 (1994) 3964.

[10] Olaf Engler, Moo-Young Huh, *Materials Science and Engineering A*, 271 (1999) 371.

[11] F. J. Humphreys and M. Hatherly, *Recrystalization and Related Annealing Phenomena*, ed. Pergamon, (1995).

[12] H. Gudmundsson, D. Brooks and J. A. Wert, *Acta Metallurgica et Materialia*, 39 (1991) 19.

[13] M. A. Miodownik, A. J. Wilkinson and J. W. Martin, *Acta Materialia*, 46 (1998) 2809.

[14] G. Pimentel**,** I. Toda-Caraballo, J. Chao and C. Capdevila, *J Mater Sci*, 47 (2012) 5605.

6. Acknowledgements

G. Pimentel thanked the MINECO the financial assistance in the form of a FPI grant. The authors thank the Ministry of Economy and Competitiveness (MINECO) the financial support through the National project ENE2009-13766-C04-01.

International Symposium on Plastic Deformation and Texture Analysis
Alcoy (Spain) 24-25 September 2012
135-147

Study of the solidification of M2 High Speed Steel laser cladding coatings

J.J. Candel, P. Franconetti, V. Amigó

ITM, Universitat Politècnica de Valencia, Camino de Vera s/n, 46022 Valencia
e-mail: juacanbo@upv.es

Abstract

High speed steel laser cladding coatings are complex because cracks appear and the hardness is lower than expected. In this paper have been manufactured M2 coatings on C45 steel and after LC processing it has been applied a tempering heat treatment to reduce the amount of retained austenite and precipitate secondary carbides.

The study of metallurgical transformations by scanning electron microscopy (SEM) and backscattered electron diffraction (EBSD) shows that the microstructure is extremely fine and complex, with eutectic transformations and MC, M_2C and M_6C precipitation. Therefore, after the laser coating is necessary to use post-weld heat treatments.

Resumen

Los recubrimientos de acero rápido por laser cladding (LC) son complejos porque aparecen fisuras y la dureza es menor a la esperada. En este trabajo se ha fabricado recubrimientos de M2 sobre acero C45 y tras el procesado por láser, se ha revenido para reducir la cantidad de austenita retenida y precipitar carburos secundarios.

El estudio de las transformaciones metalúrgicas con microscopia electrónica de barrido (SEM) y difracción de electrones retrodispersados (EBSD) muestran que la microestructura es extremadamente fina y compleja, presenta transformaciones eutécticas y precipitación de carburos MC, M2C y M6C. Por tanto, tras el recubrimiento por laser es necesario recurrir a tratamientos térmicos post-soldeo.

Keywords: Laser Cladding, High Speed Steel, EBSD, Nanoindentation

Palabras clave: Recubrimiento por Láser, Acero Rápido, EBSD, Nanoindetación

1. Introduction

High Speed Steels (HSS) exhibits very high wear resistance combined with mechanical strength when proper heat treatment is applied. Thus, they are very appreciated for cutting tool applications [1]. Its microstructure is very complex and it is composed by a martensite matrix with MC, M_2C and M_6C secondary carbides embedded [2].

The solidification sequence of M2 high speed steel after ingot casting can be described by the following reactions:

(i) Primary crystallisation of δ ferrite

(ii) Peritectic reaction: ferrite+liquid$\rightarrow$austenite

(iii) Eutectic decomposition of residual interdendritic liquid: liquid$\rightarrow$austenite+carbides

(iv) Residual ferrite in the dendritic cores transforms to austenite and carbide, which is known as the 'δ eutectoid transformation'.

Thus, the resulting as cast microstructure has a matrix with products from austenite decomposition (normally martensite and some retained austenite) and a network of eutectic carbides heterogeneously distributed in interdendritic regions [3].

During the decomposition of the residual interdendritic liquid different eutectics can form namely γ-M_2C, γ-M_6C, and γ-MC. The alloy composition and the cooling rate determine which of these eutectics precipitate. Higher cooling rates and higher vanadium contents favor the formation of M_2C and MC eutectics, while higher carbon contents also favor the formation of the M_2C eutectic; the opposite is valid for the M6C eutectic. Thus, carbide composition depends on thermomechanical processing and vanadium content [4].

However, laser processing of M2 coatings imposes a fast localized heating till melting followed by very fast cooling due focused laser irradiance applied. Therefore an abrupt thermal gradient combined with a very high solidification rate is formed inside melting pool which promotes metastable phases formation and coating cracking [5]. To overcome these difficulties it is

necessary to study the solidification of M2 coating relating the microstructure to the laser processing window.

HSS microstructure determination after LC is very complex because of extremely fine grain size (less than 5 microns) and phase distribution. On one hand, lattice parameters of MC or M_2C carbides can be different depending on Mo, W content, see table 1. And on the other hand, crystallography of the present phase is not completely established as in the case of VC (VC, V_8C_7 or V_6C_5 can be present) [6]. This problem is more acute in the case of LC coating due to microstructure heterogeneity imposed by cooling rate.

Table 1. Type, structure and lattice parameters of some carbides present in M2 steel LC coatings.

Phase	Structure	a	b	c	Type
WC	Hexagonal	0.29006		0.2837	MC
W_2C	Hexagonal	0.2997		0.4727	M_2C
MoC	Hexagonal	0.2901		0.2786	MC
Mo_2C	Hexagonal	0.3012		0.4735	M_2C
W_3Fe_3C	FCC	1.1109			M_6C

Hertzner et al remarks the importance of combining Scanning Electron Microscopy (SEM) and Electron Back Scattered Diffraction (EBSD) to determine the composition and phase distribution in the microstructure after high alloying steels heat treating [7]. And for this reason, in this work this approach has been used and it has been completed with nanoindentation measurements to quantify the effect of the microstructure on the strength of the coating.

2. Experimental Method

2.1. Laser system and raw materials

Continuous wave Nd:YAG laser system equipped with coaxial cladding laser head was used for manufacturing coatings. After process optimization, it has been fixed E = 2.1kJ/mm^2 as an optimum laser specific energy and 20 single overlapped tracks have been deposited to form the coating.

A 5mm height C45 carbon steel plate has been used as a substrate and before laser processing, surface was grinded using a P500 SiC paper and degreased with acetone.

Argon atomized AISI M2 (EN 1.3344) HSS steel powder was used as a coating. This spherical powder has a specific granulometry for LC (+30μm, -75μm) and its chemical composition is 1.22%C, 4.1%Cr, 5%Mo, 2.9%V, 6.4%W, Fe bal.

After laser processing one coating was subjected to tempering heat treatment at 550°C during 2 hours, in order to enhance secondary carbide precipitation as well as to reduce the amount of retained austenite.

2.2 Materials Characterization

Coating cross section after and before tempering heat treatment has been metallographically prepared for observation and the microstructure was revealed with Vilella etchant (95ml Etanol, 5ml HCl, 1g Picric acid).

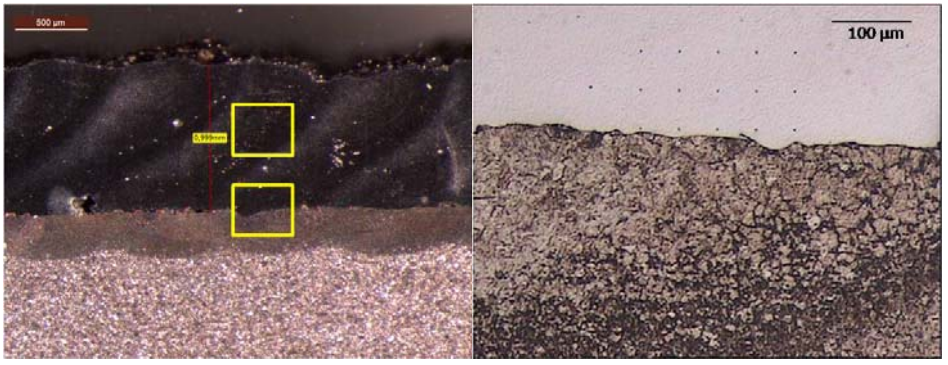

Figure 1. Cross section of the coating and selected areas for analysis.

Two different areas were selected for optical microscopy characterization, the interface between coating and substrate and the center of the coating (see figure 1). The microstructure was observed with SEM and the chemical composition determined by Energy Dispersive Spectroscopy (EDS). Finally, the phase maps distribution and orientation was determined with Electron Backscattered Diffraction (EBSD). EBSD analysis of laser cladding HSS coatings is very complex and time consuming due to the extremely fine grain size and the great variety of present phases, but coating delamination through interface justifies focusing EBSD analysis in this area.

In this preliminary work, different type phases have been selected (MC, M_2C, M_6C) taking into account that X-Ray Diffraction analysis should be necessary to determine if M is W, Mo or V with accuracy (see table 2). For metal matrix analysis, martensite and austenite phase have been selected as candidates. For secondary carbides determination, it has been selected M=W in MC, M_2C and M_6C phases, taking into account that W could be substituted by Mo, Fe or V with small lattice variations. There have not been included vanadium carbides due to their great variety, complexity (VC, V_6C_5, V_7C_8, V_2C) and residual contribution to mechanical properties.

Table 2. Selected phases for EBSD analysis

Phase group	Selected phase	Crystallography
Iron phase	Martensite	Tetragonal
Iron phase	Austenite	Face centered cubic
MC	WC	Hexagonal close packed
M_2C	W_2C	Hexagonal primitive
M_6C	Fe_3W_3C	Face centered cubic

Materials characterization is completed with nanoindentation analysis in order to determine the influence of phase distribution on nanohardness. Nanoindentation was done using Berkovich indenter and Oliver & Pahrr method. 5x5 matrix were done in the interface and in the center of the coating with F = 50 mN and 50 microns separation between imprints.

3. Results and discussion

3.1. Coating microstructure before heat treatment

Before tempering heat treatment, center of laser coating microstructure is composed by a cellular microstructure of approximately five microns grain size formed by martensite matrix and border grain carbides dispersion (see figure 2A). Near the interface between coating and substrate cooling rate increases and for this reason dendritic microstructure is present (see figure 2B).

At higher magnification a eutectic transformation in border grain can be appreciated (figure 2C). According with Boccalini M2 eutectic transformation

during solidification can be γ-M_2C, γ-M_6C or γ-MC depending on cooling rate, composition and maximum temperature [3].

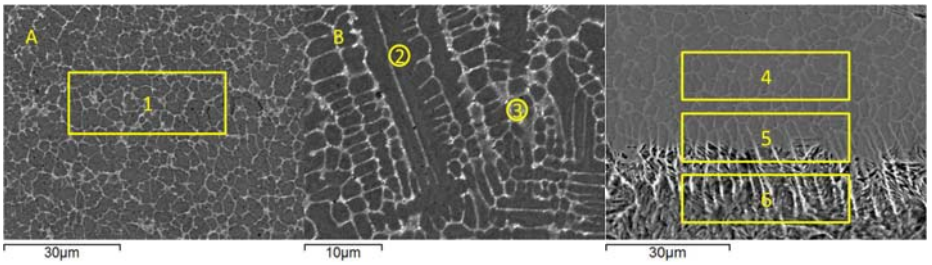

Figure 2. Microstructure of the coating before tempering: A) Center zone; B)Dendritic zone C) Coating-Substrate Interface

EDS microanalysis confirm that chemical composition of coating center area (EDS 1) is close to M2 powder initial composition, table 3. However, small variations are observed in dendritic zone due to interdifusion between coating and substrate (EDS 2, 3). Dendritic core is Fe, W-rich and according with Serna could be a martensite-M_6C zone whereas interdendritic region where eutectic transformation is present is rich in alloying elements as C, Mo and V. Interface EDS analysis (EDS 4, 5 and 6) remarks carbon diffusion to substrate whereas other sluggish alloying elements diffusivity like W or Mo is reduced. That is why zones 5 and 6 are very hard and fragile compared to C45 standard mechanical properties.

3.2. Coating microstructure after heat treatment

After tempering heat treatment it has been observed important chemical compositional change in coating and sub-interface HAZ. In cellular and dendritic microstructures, alloying element content is reduced inside cells (EDS 7) whereas it augments in border grain due to secondary carbide precipitation (EDS 8), as could be expected. However, another beneficial effect has been observed inside HAZ, alloying element content augments due to diffusion and secondary carbides also precipitates in HAZ. Thus, previous hard and fragile martensite is replaced by another complex microstructure formed by tempered martensite and secondary carbides.

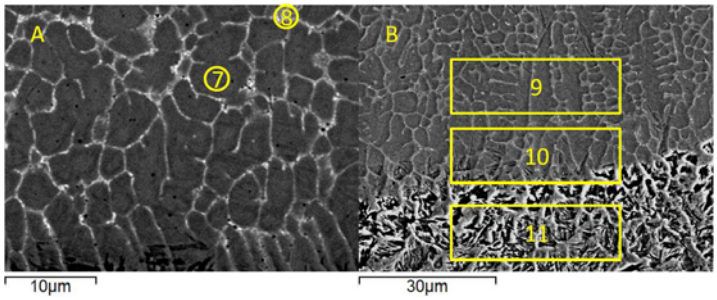

Figure 3. Microstructure of the coating after tempering: A) Cellular zone; B) Coating-Substrate Interface

Table 3. EDS microanalysis results from figure 2 and 3

Zona	C	V	Cr	Mn	Fe	Mo	W
1	1,97	2,45	3,71	0,36	80,52	4,5	6,49
2	2,22	1,62	3,35	0,32	85,25	2,63	4,63
3	5,08	4,51	4,28	0,39	69,42	6,75	3,58
4	4,12	2,68	3,42	0,44	80,18	5,08	6,31
5	2,07	2,17	2,82	0,46	83,41	3,87	5,21
6	1,95	0,35	0,51	0,54	92,99	0,63	0,86
7	2,31	1,5	2,85	0,33	85,07	2,64	5,3
8	3,87	5,64	4,45	0,45	65,48	9,36	10,75
9	1,78	2,67	3,77	0,48	80,08	4,37	6,84
10	1,6	2,52	3,74	0,35	80,93	4,57	6,29
11	3,07	1,19	1,90	0,61	87,61	2,28	3,34

3.3. EBSD analysis of phase transformations

Backscattered electron image of interface zone shows an abrupt transition before heat treatment (figure 4A). Heat affected zone (HAZ) is primary composed by martensite transformed inside austenite previous grain and for this reason EBSD quality pattern is excellent (figure 4B). Inside dendritic zone pattern quality is reduced due to microstructure complexity, thermal stress and extremely fine carbide and microporosity dispersion. However, it can be appreciated that dendrite cores are basically martensite whereas interdendritic region is composed by austenite and carbides formed after eutectic decomposition of residual liquid (figure 4C). According with Boccalini γ-M_2C, γ-M_6C or γ-MC should be the main phases distribution but it is formation depends on cooling rate and V-content during casting. With 2% vanadium and very low cooling rates (1.5 K/s) a duplex MC/M_2C microstructure was expected [3]. But, during LC process the significance of this information is

restricted because of cooling rates higher than 10^3 K/s and microstructure segregation that promote martensite transformation.

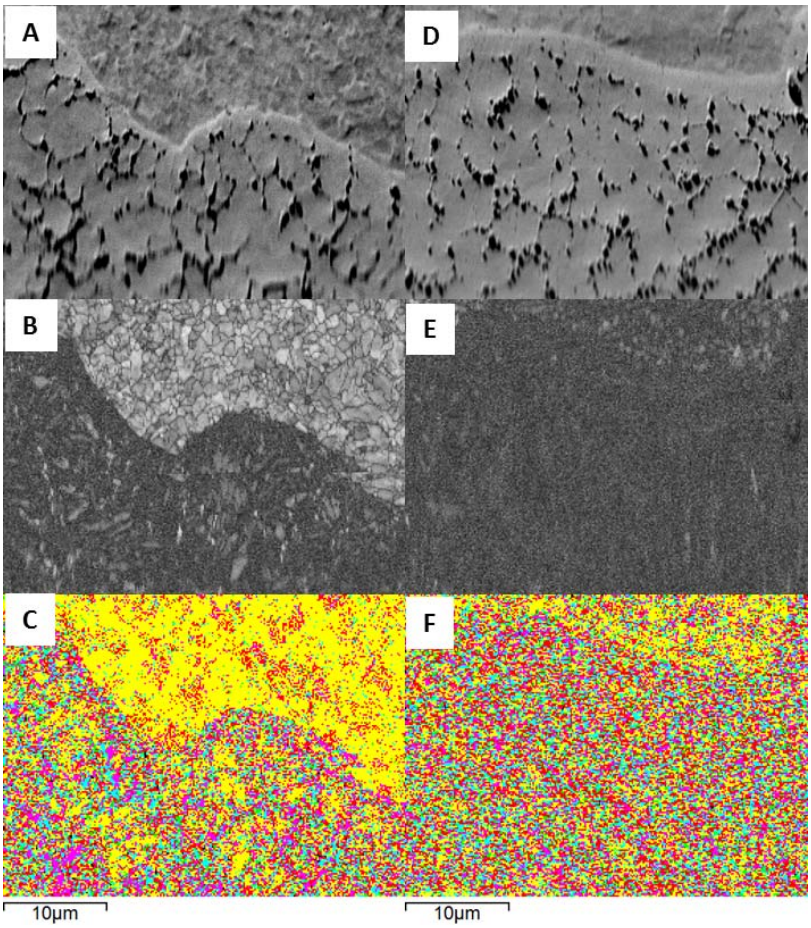

Figure 4. EBSD phase maps: SEI image of EBSD area (A, D); Quality patterns (B, E); Phase distribution map (C, F).

	Before Tempering	After Tempering
Martensite	47,9	24,2
Austenite	10,8	11,4
MC	13,8	16,8
M_2C	9,9	13,7
M_6C	3,5	4,8
None	14,2	29,1

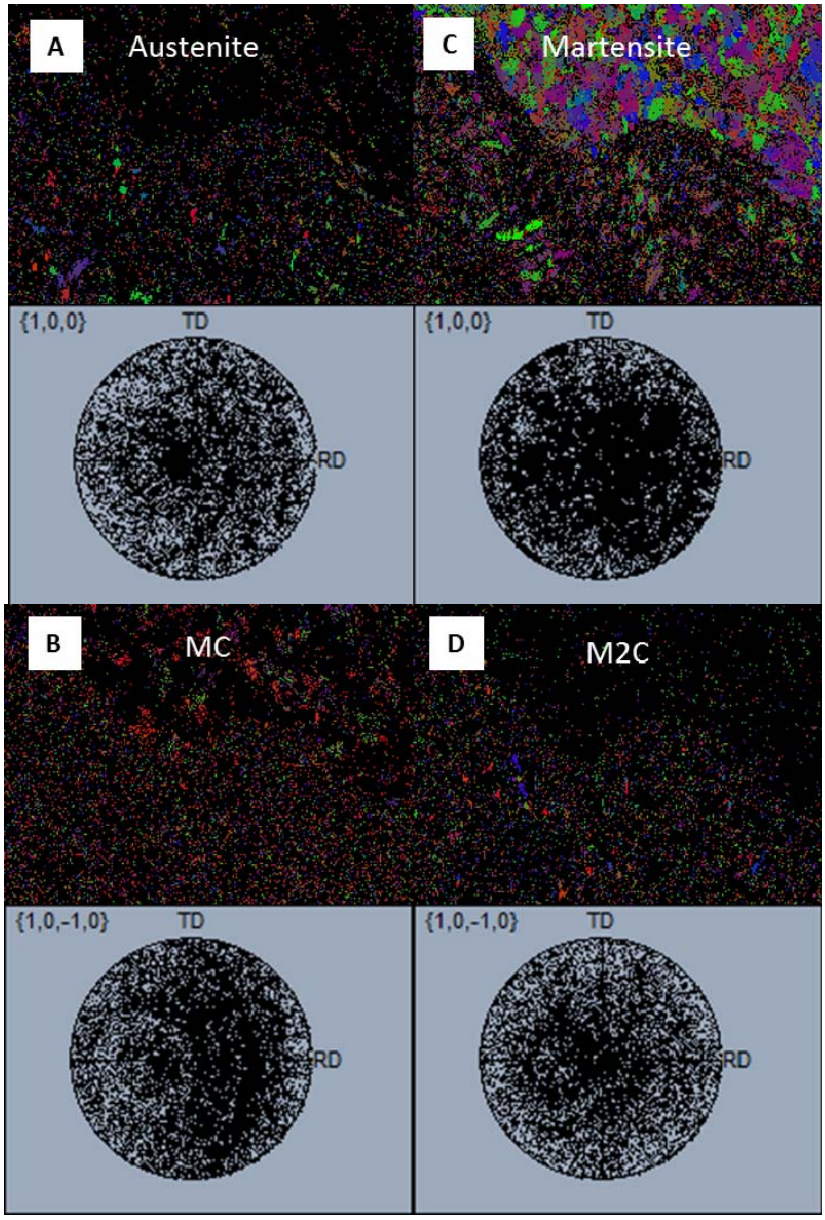

Figure 5. Pole figures of the present phases before tempering.

After tempering (figure 4D, E, F), martensite revenue and secondary carbide precipitation takes place, dendritic microstructure is eliminated and a more

gradual transition coating-substrate interface is observed. Although MC, M_2C and M_6C content (with M = W, Mo) augments another secondary carbides with major V-content precipitates and for this reason non-identified phases content augments too. However, contrary than expected, retained austenite content is not reduced. The explanation could be the peritectic reaction suppression at high temperature during cooling to form austenite from liquid and δ-ferrite due to very high cooling rate which produces a δ-ferrite retention. After tempering, δ-ferrite is eliminated and for this reason austenite content augments.

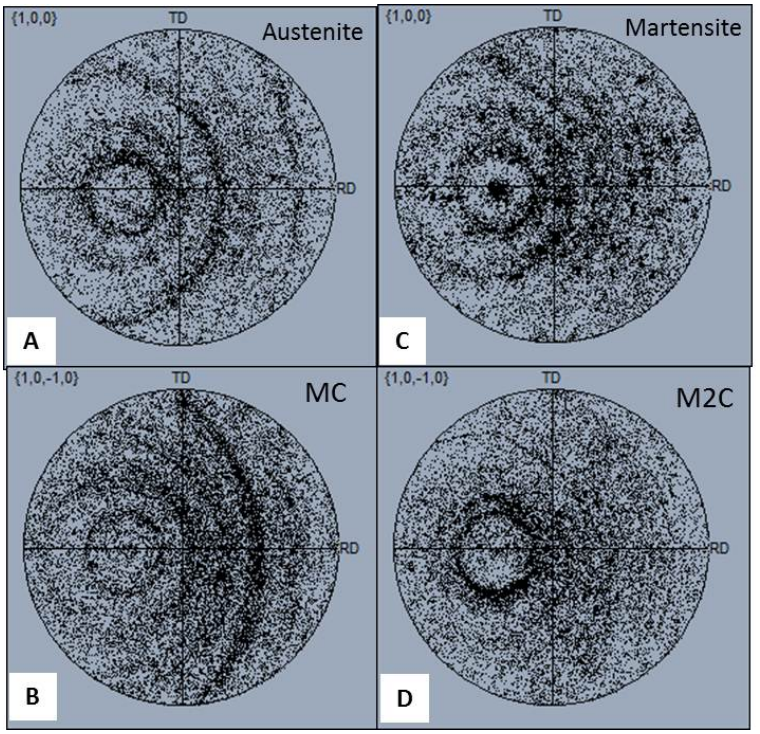

Figure 6. Pole figures of the present phases after tempering

Pole figure analysis of the present phases before heat treatment indicates no significative texture for martensite due to is mainly present in the substrate although martensite dendrites are nucleated following substrate crystallography (Fig 5B). However, eutectic transformation of carbides (mainly MC, M_2C) and austenite shows a particular solidification texture which depends on laser processing parameters and it is observed in pole figures with a circular pattern (Fig 5A, 5B and 5D).

After tempering, this solidification texture is more evident and clear, see figure 6. All the present phases follow the same circular pattern due to metastable phase reduction and thermal stress relieving.

3.4. Nanoindentation analysis of coatings

For every distance to the interface, a complete row of nanoindentation matrix, the average and standard deviation have been calculated to examine nanohardness evolution, see table 4. Nanohardness measurements in the center of the coating (cellular zone) and in the interface (dendritic zone) depicts the homogeneity in the coating and remarks the abrupt transition of hardness between coating and substrate after laser processing. No significant difference between lower dendritic and upper cellular zone hardness has been observed and its average value is about 9.6 GPa which is about enough for final application of the coating.

Table 4. Nanohardness measurements

		Rec 1		Rec 1Tempered		
	Row	Havg	Hsig	Havg	Hsig	Dist_inter (mm)
Center	1	9,576	0,651	11,946	0,54	500
	2	9,484	0,322	12,132	0,259	450
	3	9,522	0,545	11,556	0,492	400
	4	9,590	0,606	11,992	0,199	350
	5	9,902	0,744	11,850	0,358	300
Interface	1	9,596	0,463	12,080	0,316	100
	2	9,190	0,352	11,782	0,304	50
	3	5,105	0,168	6,402	0,128	0
	4	4,932	0,144	5,856	0,035	-50
	5	4,638	0,309	5,604	0,254	-100

After tempering, the average nanohardness increases above the expected level to arrive at 11.9 GPa due to the extremely fine microstructure comparing to cast HSS [8], see table 4. However is in the interface zone where the more beneficial effect takes place. As expected in EBSD analysis, the HAZ close to the interface augments its nanohardness although it is composed by tempered martensite due to secondary carbide precipitation inside. Thus, thermal stress

is relieved and microstructures has changed to another tougher than previous martensite without hardness loss.

4. Conclusions

The laser processing increases the complexity of the structure M2 high speed steel, due to the formation of metastable phases and ultra-fine grain structure. Using the combined approach based on electron microscopy, EBSD and Nanoindentation is possible to identify phases at local level.

The phase identification using EBSD is very complex, not only because of the similarity between different hexagonal phases (WC, W_2C, MoC, Mo_2C) but also to the V solution effect.

Ultrafine martensitic cellular structures are formed with grain boundary eutectic of austenite plus MC/M_2C carbides. In addition, carbon diffusion to the sub-interfacial HAZ provokes cracks after LC due to thermal stress.

Dendritic microstructure is eliminated and other complex carbides precipitate enhancing the interfacial mechanical properties after tempering.

A significant amount of MC/M_2C ultrafine hexagonal carbides (M = W, Mo) and retained austenite is still present and the final microstructure is different from the cast M2 tool steel.

It is important to continue the research into the identification of phases present by X-ray diffraction in order to confirm the presence of predefined phases and to introduce new ones to improve the identification by EBSD.

5. Bibliography

[1] Robert G, Krauss G, Kennedy R. Tool steels. Fifthed1998, Materials Park. ASM International.
[2] Mesquita R, Barbosa A, Mat Sci Eng A, 383 (2004) 87–95.
[3] Boccalini M, Correa AVO, Goldenstein H. Mat Sci Tech, 15 (1999) 621.
[4] Serna M, Rossi J, Materials Letters 63 (2009) 691–693.
[5] K.Y. Benyounis,O.M. Fakron ,J.H. Abboud, Mat Des, 30 (2009) 674–678.
[6] M. Godec, B. Batič, D. Mandrino, Mat Char, 61 (2010) 452–458.
[7] D.W. Hetzner, W. Van Geertruyden, Mat Char, 59 (2008) 825–841.
[8] M. Riabkina,E. Rabkin,P. Levin, Mat Sci Eng A, 302 (2001) 106–114.

6. Acknowledgements

Authors thank MINECO funding in special the Training of Research Staff program with the help BES-2009-013589 as well as the bilateral research project with Brazil PIB2010BZ-00448. This work was developed at the Materials Technology Unit of the Polytechnic University of Valencia associated to CSIC through the National Centre for Metallurgical Research (CENIM). Finally, thank the EU for the funding received through the FEDER help in the project UPOV08-3E-005 for the purchase of equipment and the Generalitat Valenciana for the help ACOMP/2012/094.

International Symposium on Plastic Deformation and Texture Analysis
Alcoy (Spain) 24-25 September 2012
149-159

Electron channelling contrast imaging under controlled diffraction conditions: a powerful technique for quantitative microstructural characterization of deformed materials.

I. Gutierrez-Urrutia

Max-Planck-Institut für Eisenforschung, Max-Planck Str. 1, D-40237 Düsseldorf, Germany

Abstract

We have reviewed the recently developed EBSD-based ECCI set up that allows imaging of dislocation and twin substructures with enhanced diffraction contrast. The approach makes use of the EBSD technique to obtain the tilting and rotation angles necessary to place the crystal matrix under optimum diffraction conditions. We discuss the critical microscope parameters to enhance ECCI images of deformation substructures. Examples of dislocation and twin substructures in deformed high-Mn steels are provided.

Resumen

En el presente trabajo se revisa el recientemente desarrollado EBSD basado ECCI set up que permite obtener imágenes de dislocaciones y subestructuras demaclas con un mejorado contraste de difracción. La estrategia utiliza la técnica de EBSD para obtener la inclinación y los ángulos de rotación necesarios para colocar la matriz cristalina en condiciones óptimas de difracción. Se discute los parámetros críticos del microscopio para mejorar las imágenes ECCI de deformación de subestructuras. Se proporcionan ejemplos de dislocaciones y subestructuras de maclas en aceros deformados de alto contenido en Mn.

Keywords: Electron channelling, EBSD, dislocation substructures, twin substructures, high-Mn steels.

Palabras clave: Canalización electrónica, EBSD, subestructuras de dislocación, subestructuras de maclas, aceros al manganeso.

1. Introduction

The analysis of dislocations, crystal defects and mechanical twins in metals with cubic crystal structure is commonly carried out by transmission electron microscopy (TEM). The high spatial and angular resolution of TEM allows assessing details of dislocation structures and mechanical twins, and determination of dislocation Burgers vectors. However, the main drawback in TEM is sample preparation where extremely thin samples are needed. The common methods for TEM sample preparation, electropolishing, ion milling or focused ion beam (FIB), require long time and may even modify the microstructure by introducing point defects (FIB) or relaxing internal stresses (bulk thinning prior to electropolishing). Furthermore, the resulting TEM sample has a limited observation area making it difficult to perform quantitative microstructural characterization required in many studies in materials science. While TEM has proven to be a very versatile tool for characterizing dislocation structures and crystal defects, the limitations outlined above have led to different approaches based on scanning electron microscopy (SEM) to perform the type of analysis available in TEM.

These approaches are based on the phenomena of electron channelling mechanism [1-5] leading to the electron channelling contrast imaging (ECCI) technique. ECCI makes use of the fact that the backscattered electron intensity is strongly dependent on the orientation of the crystal lattice planes with respect to the incident electron beam. This allows the observation of microstructural features with different crystal lattice orientations, such as grains, subgrains or twins. Further, as slight local distortions in the crystal lattice due to dislocations cause a modulation of the backscattered electron intensity, ECCI also allows the observation of dislocations. Since the early ECCI studies of dislocations in single crystals by Pitaval et al. and Morin et al. [6, 7], the ECCI technique has been applied to the observation of dislocation structures in metals deformed under fatigue [8, 9] or associated to cracks [10, 11], the analysis of dislocation Burgers vectors [12] and recently it has been even found to well provide information on features at the atomic scale of the crystalline surface such as atomic steps in thin-films [13, 14].

In spite of these studies, the actual implementation of ECCI as a SEM technique is limited. The main reason is the experimental conditions required for dislocation imaging. For quantitatively characterizing dislocation structures (for example, Burgers vector analysis) and imaging these structures with optimal contrast, it is required to conduct ECCI under well controlled diffraction conditions as dislocation imaging is obtained by orienting the crystal matrix exactly into Bragg condition for a selected set of diffracting lattice planes.

To date the only method utilised for performing ECCI of dislocations under controlled diffraction conditions is based on electron channelling patterns (ECP) [1-3, 5, 15]. An ECP records the changes in the backscattered electron intensity occurring as the beam is rocked through a range of incident angles relative to the crystal planes. The main drawback of this technique is the requirement of a large final aperture to allow the beam to cover a large angular regime leading to very large spatial resolution (above 2 μm, almost two orders of magnitude above the resolution of the electron backscattered diffraction technique, EBSD).

This shortcoming reduces its application to the imaging of dislocation structures in lightly deformed metals. This also explains the limited number of works that report on the use of ECCI for imaging dislocation structures. In this paper, we review the recent developed set-up for the ECCI technique under controlled diffraction conditions where the crystal orientation is obtained by means of EBSD. This set-up provides an efficient and fast operation mode to perform ECCI images of dislocations with enhanced dislocation and interface contrast in conventional field emission gun-scanning electron microscopes (FEG-SEM). Examples of the latest applications on the ECCI-EBSD based set up performed in our lab will be provided.

2. Experimental Method: novel ECCI-EBSD based set-up

Electron channelling contrast imaging (ECCI) of deformed microstructures was performed using a dual-beam Zeiss-Crossbeam instrument (Carl Zeiss SMT AG, Germany) consisting of a Gemini-type field emission gun (FEG) electron column and an focused ion beam device (Orsay Physics FIB). This instrument is equipped with an electron backscatter diffraction (EBSD) system (EDAX/TSL, Draper, UT, USA). Dislocation structures observed by ECCI were verified by transmission electron microscopy (TEM) using a Philips CM20 instrument. Thin

foils of areas previously analyzed by ECCI were prepared by ion milling by means of FIB.

The layout of the new set-up proposed for ECCI under controlled diffraction conditions is shown in Fig. 1 [16, 17]. The key contribution introduced here for performing ECCI is to use the EBSD technique instead of electron channelling patterns (ECP) for orienting the crystal into optimal diffraction conditions. This allows the imaging of deformed microstructures with the most favourable electron channelling contrast even in highly deformed materials because of the much higher spatial resolution of EBSD (35±5 nm) [18] compared to ECP (2 μm). The set-up is made up of two sample positions, Fig. 1(a). Namely, one for performing ECCI using a low-tilt configuration, where the sample is positioned perpendicular to the incident electron beam (ECCI position), and another one for performing EBSD measurements using a high-tilt configuration, where the sample is tilted 20º from the incident electron beam using a conventional EBSD geometry (EBSD position).

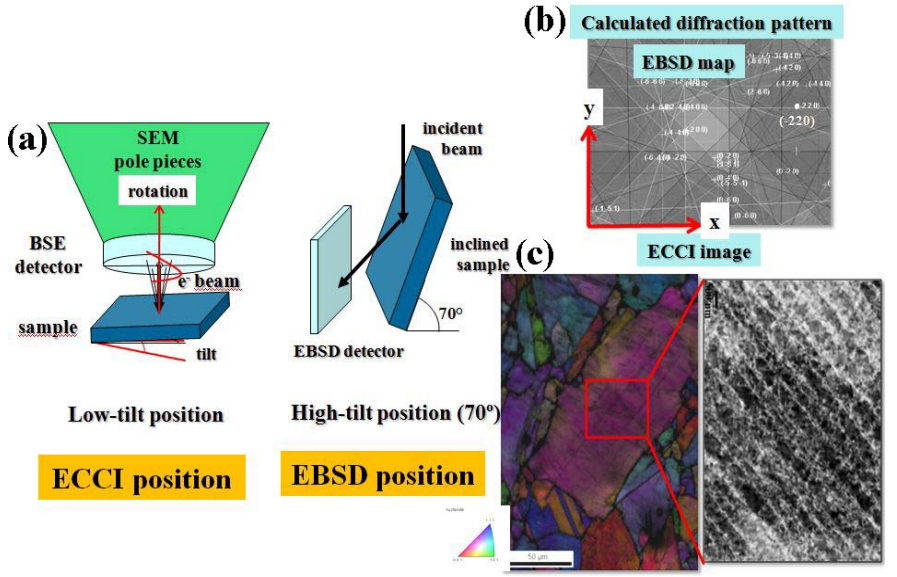

Fig. 1. Schematic illustration of EBSD-based set-up for ECCI in SEM under controlled diffraction conditions.

In this set-up ECCI under controlled diffraction conditions is performed as follows: The sample is turned into the ECCI position and the region of interest for ECCI is selected, Fig 1(a). Then the sample is tilted into the EBSD position

and an EBSD map of the selected area or an individual orientation measurement is performed. Based on the determined crystal orientation, diffraction patterns of the selected area at the ECCI position are calculated using a computer software [19] which provides the tilt and rotation angles required for orienting the crystal into optimal diffraction conditions, Fig. 1(b). Using this configuration a tilt angle range of -10º to +30º is obtained with a complete rotation of 360º. After tilting and rotating the sample to the right angles, ECCI image of dislocation substructures is performed with enhanced dislocation contrast, Fig. 1(c).

ECCI is performed using a low-tilt configuration similar to that used by Simkin et al. [20] because of the convenient position for performing crystal orientation experiments (tilting and rotating) and the enhanced electron channelling contrast. Furthermore, in the present configuration the lateral resolution is isotropic in contrast to a high-tilt configuration, like the EBSD position adapted by Trager-Cowan et al. [21] where the lateral resolution is different for the tilted and the horizontal direction.

The most critical experimental conditions in the ECCI technique are those for obtaining ECCI images of dislocations. In order to obtain an enhanced electron channelling contrast of dislocations operation conditions in SEM were optimised. In particular, the influence of the working distance and the accelerating voltage were analyzed. It was observed that the optimum contrast was achieved at working distance of around 5 mm and at accelerating voltage of 10-15 kV. The working distance is smaller than the values of 10 to 15 mm commonly used by ECCI researches. The reason for the enhanced contrast with decreasing working distance is that the amount of backscatter electrons collected by the detector is increased and, therefore, the backscattering intensity is increased.

The accelerating voltage providing the optimum contrast found here is also below the range of 20-30 kV typically used by ECCI researchers. There are two reasons for the improved contrast with decreasing acceleration voltage. First, with decreasing voltage the cross section for phonon scattering – which is responsible for the backscattering yield – is increased. As a consequence the bright parts in the image, i.e. dislocations, appear brighter while the dark parts keep their low intensity. A second reason for the improved contrast is the reduced interaction volume. In a smaller volume the lattice strain shows smaller variations, thus diffraction conditions and contrast are better defined. It is, therefore, favourable for obtaining optimal ECCI images of dislocations to

operate at working distances and accelerating voltages below the commonly used values as these operation conditions provide a much sharper electron channelling contrast. In the present study these conditions were working distance of 5 mm and accelerating voltage of 10-15 kV.

2.1. ECCI under controlled diffraction conditions: dislocation imaging

For optimum dislocation imaging is essential to perform ECCI under controlled diffraction conditions. This is achieved when the matrix crystal is oriented exactly in Bragg condition for a high intensity reflection. In this case electrons are more effectively channelled into the lattice and the backscattering yield is low, the matrix thus appears dark. At dislocations, the matrix lattice planes are slightly distorted and the Bragg condition is not fulfilled. The backscattering yield is enhanced and dislocations appear bright. The practice of creating and using controlled diffraction conditions following the ECCI procedure outlined above is illustrated and explained in Fig. 2.

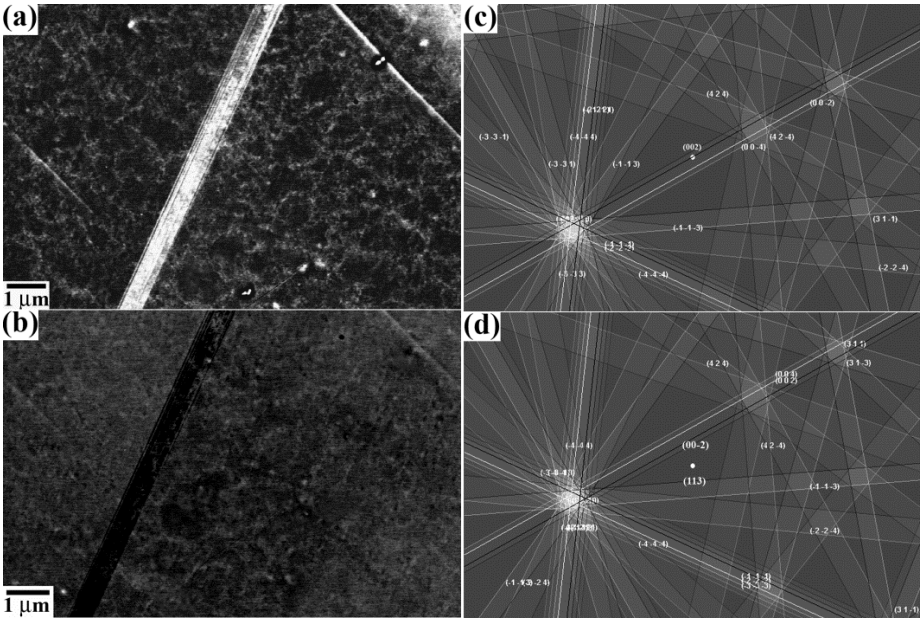

Fig. 2. ECCI images of the same sample region taken under different diffraction conditions with g=002: (a) deviation parameter s=0 (Bragg condition); (b) deviation parameter s<0. (c) and (d): simulated diffraction patterns of the corresponding ECCI images.

Fig. 2a and Fig. 2c show ECCI images of a bundle of mechanical twins and dislocations arrangements in a tensile deformed Fe-22Mn-0.6C TWIP steel in the same area but under different diffraction conditions. Diffraction conditions were selected for dislocation imaging under optimum contrast, Fig. 2a, and weak contrast, Fig. 2c. In the first case the crystal matrix was oriented exactly at the Bragg condition (deviation parameter s=0) using the high-intensity reflection (002) (simulated diffraction pattern in Fig. 2b) whereas in the second case the crystal matrix was oriented out of Bragg orientation with a negative deviation parameter s (simulated diffraction pattern in Fig. 2d).

It can be seen that in the correct diffraction condition dislocation arrangements are clearly observed whereas in unsuitable diffraction condition dislocations are hardly distinguished. Interestingly, the twins in the bundle are more clearly observed in the second diffraction condition, with twins clearly distinguished from dislocations, than in the first one. This is because in these tilting experiments the contrast of dislocations is not changed, these appear bright, whereas the contrast of twins is reverted from bright in the first diffraction condition to dark in the second one, and this contrast is darker than the contrast of the matrix. In fact, dislocations were observed in bright contrast in the complete tilting range (-10º to 30º). The origin of the bright contrast of dislocations arrangements in ECCI has been explained by Dudarev et al. [22] in terms of randomization of phase of transmitted and diffracted beams by the scattering of randomly distributed kinks on dislocation lines running nearly parallel to the incident beam. Fig. 2 demonstrates the importance of performing ECCI under controlled diffraction conditions for dislocation imaging into optimum contrast.

3. Application examples of ECCI under controlled diffraction conditions: dislocation cells and mechanical twins

ECCI has been successfully used in the quantitative characterization of complex deformed structures, namely, dislocation and twin substructures, in several steel grades [23-31]. Here, we present some examples of deformed structures imaged by ECCI. Fig. 3a shows an ECCI image of dislocation cells with an average size of about 1 μm in a tensile deformed sample of a Fe-Mn-C TWIP steel. This image was taken using the diffraction vector g= (-1-11) in Bragg condition. In order to confirm and interpret the dislocation structures observed by ECCI, a sample was first observed by ECCI under controlled diffraction conditions. The observed area was subsequently cut out using

focused ion beam (FIB), and prepared for TEM observations. Dislocation cells observed by ECCI in SEM and TEM in bright field are shown in Fig. 3a and Fig. 3b, respectively (from [16, 24]). These figures demonstrate that both microscopy techniques reveal exactly the same structure, i.e. dislocation cells of around 1 μm average diameter. The contribution of dislocation substructures such as cells to the strain hardening mechanisms of high-Mn steels has been discussed in detail in [24, 25, 29].

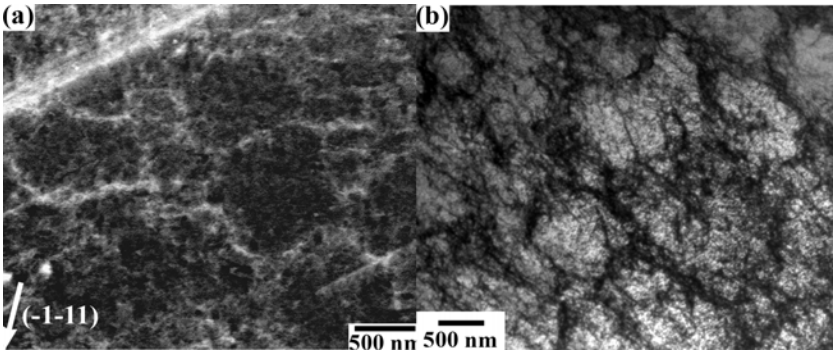

Figure 3: (a) Dislocation cells in a tensile deformed FeMnC TWIP steel observed by ECCI in SEM taken using g= (-1-11), (b) by TEM in bright-field. Images taken from [16, 24].

Fig. 4a shows an ECCI image, taken using the diffraction vector g= (1-11), of mechanical twins in a tensile deformed FeMnC TWIP steel. This figure reveals that extremely thin mechanical twins of 20-30 nm thickness can be clearly imaged by ECCI with enhanced interface contrast. Mechanical twins are identified in the following way. In case that mechanical twins are wide enough (more than 50 nm), they can be identified by EBSD measurements. Extremely thin mechanical twins that can not be indexed by EBSD can still be identified by a crystallographic trace analysis of the twin with tilting experiments in ECCI [16]. As TWIP steels are face cantered cubic metals, the trace analysis can not determine the twinning system but only the habit plane because for each habit plane there are three possible shear directions. Nevertheless, the shear direction can be determined from tilting experiments in ECCI since the contrast in these images allows selecting the corresponding diffraction pattern. Fig. 3a and Fig. 4a confirm that ECCI is a powerful technique for characterizing deformed structures containing dislocation cells and mechanical twins by SEM. This is a significant advance in microstructural characterization of deformed materials where these structures are typically observed by TEM. As ECCI is a

SEM technique it has the advantage over TEM that much larger areas can be analyzed, as shown in Fig. 4b. This figure shows in great detail different dislocation arrangements such as walls and cells, and mechanical twins contained in a large region of area 30x20 μm^2. The quantitative analysis of the evolution of these microstructural features upon straining provides a better understanding of plasticity related phenomena such as strain hardening [24-26, 29, 30].

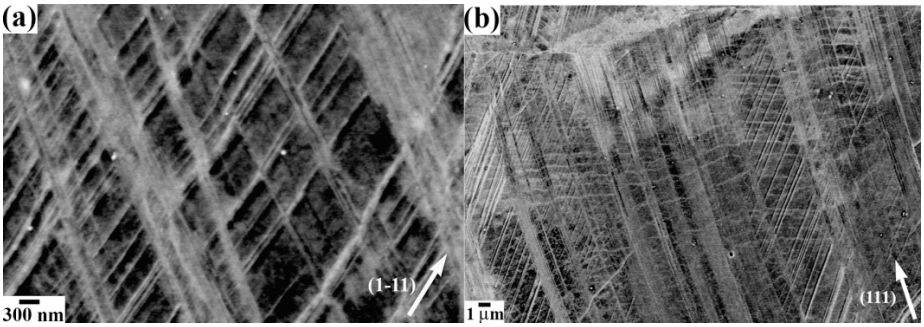

Figure 4: (a) ECCI image of mechanical twins taken using g= (1-11). (b) ECCI image taken using g= (111) showing in great detail different dislocation arrangements such as walls and cells, and mechanical twins contained in a large region of area 30x20 μm^2.

4. Conclusions

We have reviewed the recently EBSD-based ECCI set-up that allows performing

ECCI under controlled diffraction conditions by means of EBSD in conventional FEG-SEM systems. Dislocation cell structures and mechanical twins are imaged with enhanced dislocation and interface contrast by the ECCI technique. This is a significant advance in microstructural characterization of deformed materials where these structures are typically observed by TEM. The observations introduce the ECCI technique as a powerful tool for quantitative microstructural characterization of deformed materials.

5. References

[1] Schulson EM. J. Mater. Sci. 1977-R;12:1071.

[2] Joy DC, Newbury DE, Davidson DL. Rev. Phys. Appl. 1982-R;53:81.

[3] Wilkinson AJ, Hirsch PB. Micron 1997-R;28:279.

[4] Coates DG. Phil. Mag 1967;16:1179.

[5] Crimp MA. Microscopy Research Technique 2006-R;69:374.

[6] Morin P, Pitaval M, Besnard D, Fontaine G. Phil. Mag A 1979;40:511.

[7] Pitaval M, Morin P, Baudry J, Viaria E, Fontaine G. Scan. Electron. Microsc. 1977;1:439.

[8] Zhang ZF, Wang ZG. Prog. Mater. Sci. 2008;53:1025.

[9] Ahmed J, Roberts SG, Wilkinson AJ. Phil. Mag 2006;86:4965.

[10] Ng BC, Simkin BA, Crimp MA, Bieler TR. Intermetallics 2004;12:1317.

[11] Simkin BA, Ng BC, Bieler TR, Crimp MA, Mason DE. Intermetallics 2003;11:215.

[12] Crimp MA, Simkin BA, Ng BC. Phil. Mag. Lett. 2001;81:833.

[13] Picard YN, Twigg ME, Caldwell JD, C.R. Eddy J, Neudeck PG, Trunek AJ, Powell JA. Appl. Phys. Lett. 2007;90:234101.

[14] Picard YN, Twigg ME. J. Appl. Phys. 2008;104:124906.

[15] Yamamoto T. Phys. stat. sol. (a) 1977;44:137.

[16] Gutierrez-Urrutia I, Zaefferer S, Raabe D. Scripta Mater. 2009;61:737.

[17] Gutierrez-Urrutia I, Raabe D. Microsc. Microanal. 2012;18 (Suppl. 2):686.

[18] Zaefferer S. Ultramicroscopy 2007;107:254.

[19] Zaefferer S. J. Appl. Cryst. 2000;33:10.

[20] Simkin BA, Crimp MA. Ultramicroscopy 1999;77:65.

[21] Trager-Cowan C, Sweeney F, Trimby PW, Day AP, Gholinia A, Schmidt NH, Parbrook PJ, Wilkinson AJ, Watson IM. Phys. Rev. B 2007;75:085301.

[22] Dudarev SL, Ahmed J, Hirsch PB, Wilkinson AJ. Acta Cryst. 1999;A55:234.

[23] Gutierrez-Urrutia I, Zaefferer S, Raabe D. Mater. Sci. Eng. A 2010;527:3552.

[24] Gutierrez-Urrutia I, Raabe D. Acta Mater. 2011;59:6449.

[25] Gutierrez-Urrutia I, Raabe D. Mater. Sci. For. 2012;702-703:523.

[26] Gutierrez-Urrutia I, Raabe D. Scripta Mater. 2012;66:992.

[27] Eisenlohr A, Gutierrez-Urrutia I, Raabe D. Acta Mater. 2012;60:3994.

[28] Gutierrez-Urrutia I, Raabe D. Scripta Mater. 2012;66:343.

[29] Gutierrez-Urrutia I, Raabe D. Acta Mater. 2012 in press.

[30] Gutierrez-Urrutia I, Raabe D. Submitted to Scripta Mater.

[31] Steinmetz DR, Jäpel T, Wietbrock B, Eisenlohr P, Gutierrez-Urrutia I, Roters F, Raabe D. Submitted to Acta Mater.

6. Acknowledgments

The author would like to acknowledge the financial support by the German Research Foundation in the framework of the SFB 761 “steel ab initio” as well as the MPIE-TKES collaborative initiative. The author has been also benefited from helpful discussions with M. Crimp, D. Raabe and S. Zaefferer on the ECCI technique.

International Symposium on Plastic Deformation and Texture Analysis
Alcoy (Spain) 24-25 September 2012
161-173

Application of EBSD to investigation of creep deformation in high-temperature ferritic steels

V. A. Yardley[1], E. J. Payton[2], T. Matsuzaki[3], R. Sugiura[3], A. T. Yokobori Jr.[3], S. Tsurekawa[4]

[1]Institut für Werkstoffe, Ruhr-Universität Bochum, 44780 Bochum, Germany
[2]Bundesanstalt für Materialforschung und -prüfung, 12205 Berlin, Germany
[3]Tohoku University Graduate School of Engineering, Sendai 980-8579, Japan
[4]Kumamoto University Graduate School of Engineering, Kumamoto 860-8555, Japan

Abstract

Energy efficiency and environmental concerns have led to the need for materials able to withstand higher temperatures and stresses in industries such as power generation and aerospace. Understanding and prediction of materials behaviour under these exacting conditions is of great importance to ensure safe operation while avoiding costly premature replacement of components. Mechanical testing and examination of ruptured or interrupted test specimens using electron-optical techniques such as conventional scanning electron microscopy (SEM), electron backscatter diffraction (EBSD) and transmission electron microscopy (TEM) can provide us with useful information on high-temperature fracture and deformation mechanisms. One of the important materials classes used in power generation is the family of 9-12 wt. % Cr tempered martensite ferritic steels. The complex, hierarchical microstructure of these alloys poses particular and interesting challenges for EBSD examination. The present article summarises the analysis techniques that have been developed for the study of plastic deformation and fracture in this class of materials.

Resumen

La eficiencia energética y el medio ambiente han llevado a la necesidad de materiales capaces de soportar altas temperaturas y presiones en industrias tales como la generación de energía y la aeroespacial. La comprensión y

predicción del comportamiento de los materiales bajo estas condiciones rigurosas es de gran importancia para asegurar la segura operación evitando al mismo tiempo el costoso reemplazo prematuro de los componentes. Los ensayos mecánicos y el examen de especímenes rotos o interrumpidos utilizando técnicas ópticas y de electrones, tales como la microscopía electrónica de barrido convencional (SEM), difracción de electrones retrodispersados (EBSD) y microscopía electrónica de transmisión (TEM) nos puede proporcionar información útil sobre fractura a elevadas temperaturas y los mecanismos de deformación. Una de las clases de materiales que se utilizan en mayor medida en la generación de energía es la familia de aceros ferrítico-martensíticos, con un 9-12 % en peso de Cr, templados. La microestructura compleja y jerárquica de estas aleaciones plantea retos particulares e interesantes para el examen por EBSD. El presente trabajo resume las técnicas de análisis que se han desarrollado para el estudio de la deformación plástica y la fractura en esta clase de materiales.

Keywords: Ferritic steels, electron backscatter diffraction (EBSD), creep, plastic deformation, fracture

Palabras clave: Aceros ferríticos, difracción de electrones de retrodispersados (EBSD), fluencia, deformación plástica, fractura

1. Introduction

Ferritic steels with a tempered martensitic microstructure (tempered martensite ferritic steels, TMFS) are used extensively in steam power plant, where long-term resistance to creep and oxidation in the 550-600°C range at steam pressures of up to 300 bar is required [1–6]. As a result of the diffusionless transformation from austenite to martensite, the microstructure of these steels contains a high density of internal interfaces and dislocations. These, together with fine precipitates formed on controlled tempering, such as transition metal carbonitrides of the type MX, provide satisfactory mechanical properties in the service temperature range. Thanks to improvements in alloy design, it has been possible over the years to increase the operating temperature, and therefore efficiency, of thermal power plant [1,2,7]. Even in alloys specifically designed for high-temperature service, however, prolonged exposure to high temperature and stress leads to gradual microstructural coarsening and consequent degradation of the creep resistance. If unchecked, these processes can lead to unacceptable creep deformation or even to

rupture of components. In addition, the complex shapes of some plant components can cause stress concentration and an increased likelihood of creep cracking. Standard creep test specimen geometries therefore include bars for uniaxial tensile testing and specimens designed to study the growth of cracks, such as the compact tension C(T) geometry [8].

The martensitic microstructure in tempered martensite ferritic steels is produced by performing a solution heat-treatment in the austenite phase stability temperature range, and then cooling sufficiently rapidly to prevent diffusional transformations. The required cooling rate, and the temperature at which the martensitic transformation start, depend on the alloy composition. On transformation, each grain of austenite subdivides into an assemblage of fine martensite laths approximately 0.3-0.5 μm wide [9], each of which exhibits one of up to 24 distinct crystallographic orientations (variants) determined by the orientation relationship between martensite and austenite. In steels with relatively low carbon content, such as typical 9-12 wt. % Cr power-plant alloys, laths of the same variant tend to occur together in elongated assemblages termed blocks. Furthermore, blocks with parallel long axes are found together in larger units known as packets. This structure has been described in detail for carbon steels [10–14] and confirmed by recent studies to be essentially the same in 9-12 wt.% Cr heat-resistant steels [15,16]. After a standard industrial tempering treatment of typically two hours at around 923-973K, the crystallographic orientations of the ferrite micrograins formed are inherited essentially unchanged from those of the corresponding martensite. As a result, the microstructure contains a high density of both low- and high-angle grain boundaries of specific misorientations.

Mechanical behaviour of steels with martensitic microstructures has been shown to be dependent on the sizes of blocks and packets, which themselves increase monotonically with the prior austenite grain (PAG) size, in carbon steels [17,18]. In creep crack growth tests on 1Cr1Mo steels, the minimum creep rate decreased with increasing PAG size down to a minimum for PAG of around 50 μm, and then levelled off or even began to increase again at higher applied stresses [19]. In uniaxial creep of 3Ni1Cr steel, the fracture mode was found to change from ductile to brittle with increasing PAG size [20]. Similarly, in W-alloyed 9-12 wt. % Cr steels, samples with coarse PAG samples were found to crack in a more brittle manner than those of very similar chemical composition but finer PAG [21].

The evolution of the microstructure during high-temperature exposure and creep deformation has been extensively investigated using transmission electron microscopy. The size of the ferrite micrograins increases much more rapidly under uniaxial tensile creep conditions than under high temperature exposure alone [9,22–26]. Creep exposure increases the proportion of very low angle (~1°) grain boundaries [15,23–25,27]; in contrast, no such increase was observed after long-term heat exposure without applied stress [25]. The dislocation density in the initial martensitic state is very high [28]. Tempering reduces the dislocation density, and creep exposure causes a more pronounced decrease [23,28]. Taking these results together, it can be concluded that long-term high temperature exposure primarily causes micrograin coarsening and the annihilation of a certain fraction of the dislocations, while exposure to both high temperature and stress initiates a reorganisation of the dislocation substructure into new subgrains. On a larger length scale, EBSD observations have shown the formation of a strong {110} texture parallel to the tensile axis in the necked regions of uniaxial tensile creep specimens of 9 wt. % Cr steels [29]. The evolution of microstructure in more complex specimen geometries does not appear to have been investigated yet. In the present paper, EBSD will be used to investigate the microstructural sites at which damage occur and the evolution of the microstructure under creep crack growth test conditions.

2. Experimental and Analysis Methods

2.1. Specimens and creep testing

The analysis techniques available for investigating creep crack growth using EBSD will be illustrated using one specimen exhibiting typically creep-brittle behaviour and one specimen showing creep-ductile behaviour. Both specimens had the compact tension (1C(T)) geometry with side groove [8] and were tested using a lever-arm testing machine RT-30 (TOSHIN KOGYO). The brittle specimen (Specimen A) was taken from a 12 wt. % Cr rotor steel with a relatively large prior austenite grain size of ≈200 μm (as measured using the intercept method defined by ASTM [30]) tested at 923 K under a constant load of 311.8 MPa. Specimen B, showing ductile fracture, is a P92 (NF616) 9 wt. % Cr steel with a prior austenite grain size an order of magnitude smaller at ≈30 μm. In this case the constant load was also 311.8 MPa and the test was

carried out at 873K. The chemical compositions of the two specimens are given in Table 1 and Table 2 respectively.

Table 1: Composition of Sample A in mass %

C	Cr	Mo	W	Nb	V	Co
0.09	10.89	0.17	2.61	0.06	0.2	2.52
Ni	Si	Mn	Al	N	B	
0.5	0.03	0.49	0.003	0.02	0.011	

Table 2: Composition of Sample B in mass %

C	Cr	Mo	W	Nb	V	Co
0.09	8.72	0.45	1.87	0.06	0.21	-
Ni	Si	Mn	Al	N	B	
-	0.16	0.47	-	0.05	0.002	

The EBSD specimens were obtained by interrupting the creep tests in the secondary creep regime and sectioning the test specimens in the plane containing the tensile axis and the direction of crack growth, as shown in Figure 1(a). The area surrounding the crack tip was then cut out (Figure 1(b)) and mounted in electrically conducting resin. Where this resin did not completely fill the small hollows and sub-cracks in the cracked region, Araldite bond was inserted to help avoid mechanical damage during polishing. After conventional metallographic preparation, consisting of grinding to No. 4000 emery paper and a few minutes each of polishing with 1 µm and 0.3 µm alumina slurry, the specimens were polished with 0.05 µm colloidal silica suspension for approximately three hours. This treatment gives considerably better edge retention than electropolishing and is therefore preferable in cases where examination of cracks, pores and surfaces is important, such as the specimens examined here. Since particles of polishing media can easily become trapped in the rough surfaces of these specimens and then subsequently become dislodged, possibly causing surface scratches, ultrasonic cleaning was carried out between each polishing step. The metallographic specimen is shown in Figure 1(c). It has been found from experience that the most satisfactory EBSD patterns are obtained when the surface shows a slightly etched appearance resulting from to the chemical action of the

colloidal silica suspension. A mirror-like appearance indicates that more polishing is still required.

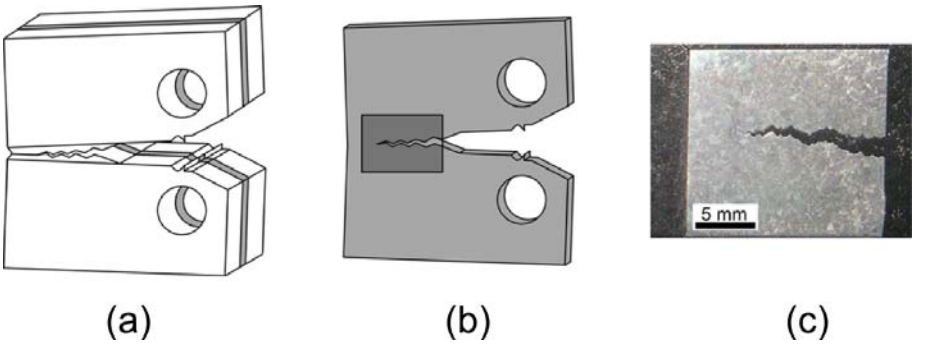

Figure 1: (a) Interrupted C(T) test specimen with location of vertical section shown in grey; (b) location of metallographic specimen shown in dark grey; (c) photograph of metallographic specimen.

2.2. EBSD observations

The EBSD data were acquired using a field emission gun SEMs (HITACHI S-4200) equipped with a TSL EBSD-OIM analysis system. An alpha-iron (BCC) crystal structure with a lattice parameter a=0.287 nm was assumed. The accelerating voltage used was 25 kV, and the majority of the maps were obtained using a magnification of 500x and step size of between 0.25 and 0.5 µm, although higher magnifications and smaller step sizes were also used in regions of especial interest.

In EBSD scans acquired from regions containing cracks and pores, these can give rise to spurious orientation data. However, these data appear to be approximately random, such that neighbouring analysis points in these regions usually have different orientations. As a result, the spurious points can be eliminated relatively easily using a partitioning function that regards points misoriented from one or more of their neighbours by less than a given angle as part of a cluster or “grain”, and removes points that belong to “grains” of fewer than a user-specified number of points.

Every effort was taken to obtain clear EBSD patterns to avoid the use of cleaning algorithms that may risk introducing artefacts into the dataset. However, for grain boundary studies, a single iteration of the “grain dilation” cleaning algorithm was used.

2.3. Crystallographic analysis methods

As has been known since the 1930s, there is a well-defined orientation relationship between austenite and the martensite formed from it [31–34]. This orientation relationship (OR) can be used to identify the structural units inherited from the martensitic transformation, such as packets and prior austenite grains, and to determine whether cracking, creep cavitation or other damage is associated preferentially with any of these sites. The true orientation relationship depends on the chemical composition of the alloy, particularly on the carbon content [10,11] (or more precisely, on the composition of the matrix at the time of martensitic transformation). Nonetheless, the similarity of the {001} pole figure of the tempered martensite to the ideal pole figures for the Kurdjumov-Sachs and Nishiyama-Wassermann OR, as illustrated, for example in Refs. [13] and [35] respectively, enable us to identify which parts of the tempered martensitic microstructure is associated to which prior austenite grains. Furthermore, this similarity allows us to estimate the orientations of the prior austenite grains and calculate the properties of the grain boundaries between them (Figure 2). Packets can also be identified, since experimentally each packet is found to correspond to a different {111} plane of austenite lying parallel to the (011) plane of martensite in the ideal orientations listed in Refs. [13] and [35].

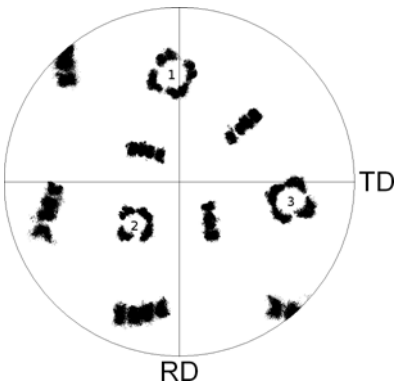

Figure 2: {001} pole figure for ferrite micrograins arising from a single prior austenite grain in tempered martensite ferritic steel. The {001} poles of the parent austenite are located at the points labeled 1, 2 and 3.

A more precise measurement of the orientation relationship permits us to identify block and packet boundaries in the microstructure and to follow how the distribution of such boundaries evolves with exposure to high

temperatures and creep stresses; the reader is referred to Ref. [36] for details of this technique. This enables us to determine to what extent the martensite-like microstructure is preserved at individual locations in the microstructure. This analysis was performed using MATLAB codes developed in-house using the MTEX crystallographic analysis toolbox (http://code.google.com/p/mtex/).

3. Results and discussion

3.1. Specimen A (12 wt. % Cr rotor steel, brittle creep)

A composite map made from around twenty individual EBSD scans taken from the vicinity of the crack is shown in the left-hand part of **Figure 3**. The prior austenite grain orientations and grain boundary properties, determined using the techniques outlined in Section 2.3, are illustrated using wireframes and lines respectively. Grey lines represent grain boundaries deemed to be "special" according to the Brandon criterion [37] (the only such boundaries identified here being low-angle, Σ3 or Σ9) and black lines represent all other types of grain boundaries (random boundaries). A greyscale EBSD image from the ferrite appears in the background to give an idea of the scale of the tempered martensitic microstructure. Cracks and cavities appear in black and the tip of the crack is marked. It is clear that some subsidiary cracks and cavities have already formed ahead of the tip and that the predominant site for cracking is along random prior austenite grain boundaries; where this is the case, the cracks are narrow and sharp, whereas when they traverse the prior austenite grains they are more rounded or jagged in appearance, indicating that a larger degree of plastic deformation was required for their formation. The right-hand side of **Figure 3** shows one of the grains with intragranular damage in more detail. The grain boundaries corresponding to misorientations between martensitic substructural units appear in white and those with other misorientations are shown in black. The distribution of boundaries in the top left of the grain more closely resembles that of a typical martensite, whereas in the vicinity of the damage, a large concentration of other boundaries can be found. Recent, as yet unpublished work by some of the present authors has shown that a decrease in the fraction of block boundaries and an increase in the fraction of boundaries unrelated to the original martensite microstructure correlates with macroscopically observable plastic deformation (necking) in uniaxial tensile creep specimens. There is therefore good reason to suppose that the microstructure observed here is indicative of localised plastic

deformation in an otherwise brittle specimen. This and other intragranular cracking appears to be associated in part with twin and packet boundaries although the damage also sometimes appears to pass through packets.

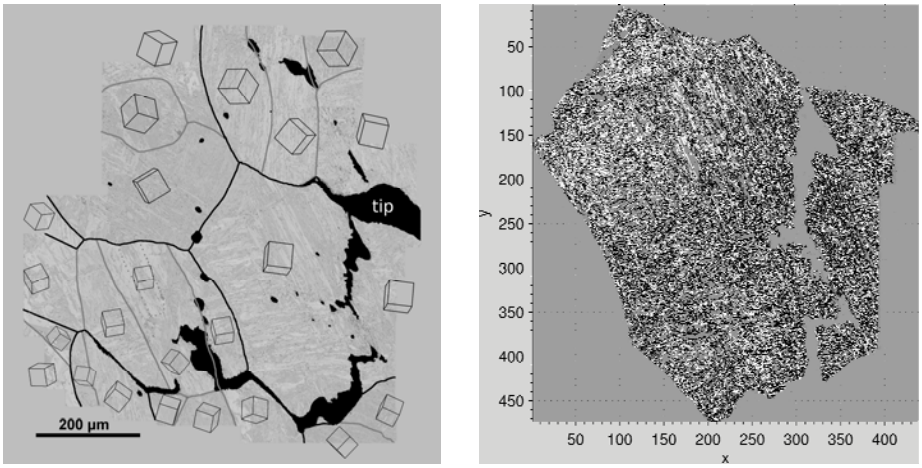

Figure 3: (Left) Map of the region around the crack tip. Random prior austenite grain boundaries are shown in black and "special" (here defined as low-angle, Σ3 or Σ9) grain boundaries in grey. The orientations of the prior austenite grains are represented by wire-frames. (Right) Map of the distribution of boundaries in the microstructure. Boundaries in white are those corresponding to martensitic block misorientations.

3.2. Specimen B (9 wt. % Cr boiler steel, ductile creep)

Optical micrographs show that this crack is made up of cavities, which are small and irregularly shaped ahead of the crack tip but become rounder and coalesce to form a continuous crack. The left part of Figure 4 shows an EBSD image quality map of a prior austenite grain in the cavity-containing region ahead of the crack tip in this specimen. From the crystallographic analysis methods discussed above, the prior austenite grain boundary and packet boundaries have been identified; these are marked in white and black, respectively. Most of the cavities are found on the PAG, particularly at triple junctions with packet boundaries, while others are located on packet boundaries only, or within packets. From the literature it is known that creep cavities nucleate readily on inclusions (e.g. oxides and sulphides) even at low strains [38,39]. Cavity propagation involves secondary nucleation on carbides at prior austenite grain and micrograin boundaries [39]; this occurs at higher

strains than the nucleation on inclusions [38, 40]. Results from Auger spectroscopy suggest that sulphur segregation to carbide/matrix interfaces assists in the nucleation of cavities [41]. High-temperature segregation and/or phases that are not dissolved during austenitisation may account for the preferential cavity formation at prior austenite grain boundaries. Also, coarse carbide formation occurs preferentially at triple junctions, followed by high-angle grain boundaries. The apparent stability of block boundaries against cavity formations is not as straightforward to account for, but it is also observed in regions between growing cavities, as shown in the right-hand side of Figure 4. Here, parallel blocks lie between the two large cavities but, rather than any cavitation along the block boundaries, rotation occurs within the blocks, as shown by the wireframes indicating local orientation.

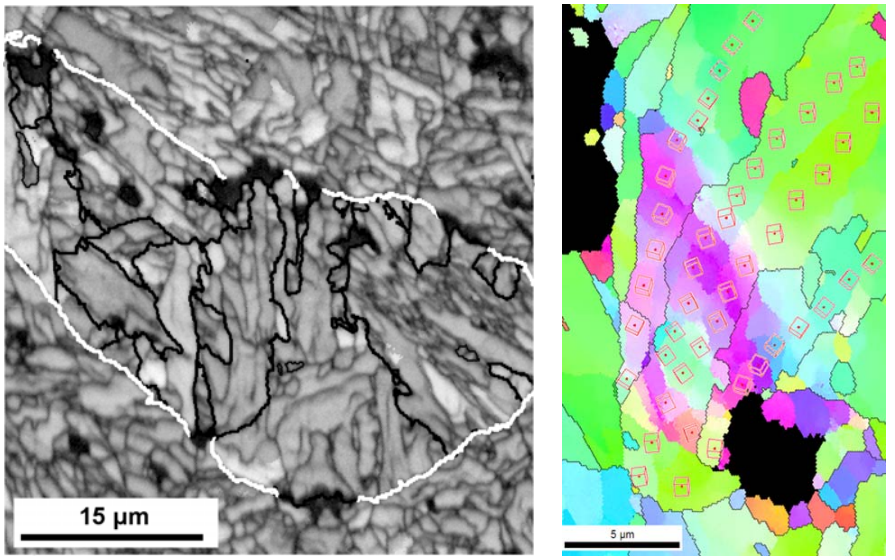

Figure 4: (Left) EBSD image quality map of the region ahead of the crack tip. Prior austenite grain boundaries are shown in white and packet boundaries in black (Right) Grain rotation within blocks lying between two medium-sized cavities.

Another instance of the same phenomenon has also been observed. In recent, unpublished work by some of the present authors, the former block boundaries were found to have changed to near-60˚ boundaries with a wide range of different rotation axes in the necked part of uniaxial tensile creep specimens. This configuration, which appears to be more stable under tension,

can be achieved by small rotations from the original block microstructure. However, further investigation is needed to determine more precisely the processes occurring here.

4. Conclusions

The two examples discussed here show how analysis methods making use of the unique crystallographic properties of tempered martensite ferritic steels can be applied to learn more about the cracking and deformation processes occurring. These techniques complement more established and generally applicable approaches such as measurement of the kernel average misorientation, pattern quality, grain misorientations, etc. as well as TEM measurements of micrograin coarsening and precipitate distribution evolution. Programs applying the EBSD-based techniques have been written using the MTEX toolbox for MATLAB and are still under active development.

5. Bibliography

1. Masuyama, F. *ISIJ International* **41(6)**, 612–625 (2001).
2. Klueh, R. L. & Harries, D. R. Chapter 2: Development of High (7-12%) Chromium Martensitic Steels. *High-Chromium Ferritic and Martensitic Steels for Nuclear Applications* 5–27 (2001).
3. Maruyama, K., Sawada, K. & Koike, J. *ISIJ International* **41(6)**, 641–653 (2001).
4. Fujita, T. *Tetsu-to-Hagane* **76(7)**, 1053–1059 (1990).
5. Ennis, P. J. & Czyrska-Filemonowicz, A. *Sādhanā* **28**, 709–730 (2003).
6. Abe, F. *Current Opinion in Solid State and Materials Science* **8**, 305–311.
7. Abe, F., presentation at Thermec 2011 (Quebec, Canada, August 2011).
8. ASTM ASTM E1457-07: Standard Test Method for Measurement of Creep Crack Growth Times in Metals, 2007.
9. Abe, F. *Proc. fourth international conference on recrystallisation and related phenomena* 289–294 (1999).
10. Maki, T., Tsuzaki, K. & Tamura, I. *Trans. ISIJ* **20**, 207–214 (1980).

11. Morito, S., Tanaka, H., Konishi, R., Furuhara, T. & Maki, T. *Acta mater.* **51**, 1789–1799 (2003).
12. Morito, S., Huang, X., Furuhara, T., Maki, T. & Hansen, N. *Acta mater.* **54**, 5323–5331 (2006).
13. Kitahara, H., Ueji, R., Tsuji, N. & Minamino, Y. *Acta mater.* **54**, 1279–1288 (2006).
14. Morito, S., Adachi, Y. & Ohba, T. *Materials Transactions* **50**, 1919–1923 (2009).
15. Sanchez-Hanton, J. J. & Thomson, R. C. *Mater. Sci. Eng. A* **460–461**, 261–267 (2007).
16. Yardley, V. A. *et al. Strength. Fract. Complex* **5**, 39–52 (2007).
17. Krauss, G. *Mat. Sci. Eng.* **A273-275**, 40–57 (1999).
18. Morito, S., Yoshida, H., Maki, T. & Huang, X. *Mater. Sci. Eng. A* **438-440**, 237–240 (2006).
19. Kimura, K. *et al. Scripta Metallurgica* **21**, 19–22 (1987).
20. Hong, S. H. & Yu, J. *Scripta Metallurgica* **23**, 1057–1062 (1989).
21. Sugiura, R. *et al. Materials Transactions* **48**, 2928–2936 (2007).
22. Abe, F. *Materials Science and Engineering A* **387-389**, 565–569 (2004).
23. Pesička, J., Dronhofer, A. & Eggeler, G. *Mater. Sci. Eng. A* **387-389**, 176–180 (2004).
24. Dronhofer, A., Pesička, J., Dlouhý, A. & Eggeler, G. *Z. Metallkd.* **94**, 511–520 (2003).
25. Aghajani, A., Somsen, C. & Eggeler, G. *Acta Materialia* **57**, 5093–5106 (2009).
26. Szabó, P. J. *Materials Science and Engineering A* **387–389**, 710–715 (2004).
27. Tak, K.-G., Schulz, U. & Eggeler, G. *Materials Science and Engineering: A* **510-511**, 121–129 (2009).
28. Pesicka, J., Kuzel, R., Dronhofer, A. & Eggeler, G. *Acta Materialia* **51**, 4847–4862 (2003).

29. Nakashima, H., Terada, D., Hayakawa, H. & Yoshida, F. *Heat-resistant metallic materials 123 committee members' research reports* **42**, 173–182
30. ASTM ASTM E112-96(2004)e2: Standard Test Methods for Determining Average Grain Size, 2004.
31. Kurdjumow, G. & Sachs, G. *Z. Physik* **64**, 325–343 (1930).
32. Nishiyama, Z. *Sci. Rep. Tohoku Imperial University* **23**, 637–664 (1934).
33. Wassermann, G. *Mitteilungen aus dem Kaiser Wilhelm Institut für Eisenforschung* **17**, 149–155 (1935).
34. Greninger, A. B. & Troiano, A. R. *Metals Transactions* **185**, 590–598 (1949).
35. Kitahara, H., Ueji, R., Ueda, M., Tsuji, N. & Minamino, Y. *Materials Characterization* **54**, 378–386 (2005).
36. Payton, E. J., Aghajani, A., Otto, F., Eggeler, G. & Yardley, V. A. *Scripta Materialia* 66 (2012) 1045–1048
37. Brandon, D. G. *Acta metall.* **14**, 1479 (1966).
38. Senior, B. A., Noble, F. W. & Eyre, B. L. *Acta Metallurgica* **36**, 1855–1862 (1988).
39. Gooch, D. J. *Metal Science* **16**, 79–89 (1982).
40. Senior, B. A., Noble, F. W. & Eyre, B. L. *Acta Metallurgica* **34**, 1321–1327 (1986).
41. Eggeler, G., Earthman, J. C., Nilsvang, N. & Ilschner, B. *Acta Metallurgica* **37**, 49–60 (1989).

6. Acknowledgements

The authors would like to thank the 129 committee of the Japan Society for the Promotion of Science (chairman: Prof. T. Yokobori) for support of parts of this work and provision of samples.

International Symposium on Plastic Deformation and Texture Analysis
Alcoy (Spain) 24-25 September 2012
175-185

Review on the EBSD characterization of hot worked microstructures in steels

D. Jorge-Badiola, A. Iza-Mendia
CEIT and Tecnun (University of Navarra), Manuel de Lardizabal 15, 20018 Donostia-San Sebastián, Basque Country, Spain

Abstract

The EBSD (Electron BackScatter Diffraction) has become an essential technique for analyzing the microstructural evolution of steels during hot working. Under industrial processing conditions steels undergo significant strains and, as a consequence, complex microstructural changes as static/dynamic recovery, static/dynamic recrystallization can occur. These all result in a plentiful amount of substructural states. In order to properly characterize these states, some different EBSD parameters/indicators have been proposed. However, these might not be capable to describe accurately the substructural evolution. Here, some of the up to date drawbacks and partially unsolved problems are addressed in that respect and some emerging strategies to face up all these questions are discussed.

Resumen

La técnica EBSD (Difracción de Electrones Retrodispersados) se ha convertido en una herramienta fundamental para el análisis de la evolución microestructural durante el conformado en caliente de los materiales metálicos. Bajo condiciones industriales usuales, los aceros, en particular, se ven sometidos a deformaciones y, como resultado de este proceso, se producen cambios microestructurales complejos como son la restauración éstatica/dinámica o la recristalización estática/dinámica. Todo esto da lugar a una gran cantidad de estados subestructurales. Con el fin de caracterizar estos estados, en la literatura se han propuesto diferentes parámetros/indicadores medidos mediante barridos de EBSD. No obstante, estos parámetros no son capaces de describir con precisión y de forma general la evolución subestructural. En este trabajo, se explica la problemática sobre este tema, y

se discuten algunas de las estrategias emergentes que podrían suponer un avance en la caracterización de estas microestructuras.

Keywords: EBSD, hot working, twin boundaries, Image Quality, misorientation.

Palabras clave: EBSD, conformado en caliente, limites de maclas, Imagen de Calidad, desorientación.

1. Introduction

Under hot working conditions, the steels undergo significant microstructural changes as a result of various physical phenomena. The application of strain at high temperatures involves the introduction of dislocations that rearrange during strain (dynamic recovery) and eventually if enough strain is applied, new grains with lower dislocation density inside can be formed (dynamic recrystallization, DRX). Afterwards, during the time between deformation passes, other softening processes as static recovery and static (metadynamic) recrystallization SRX (MDRX) can take place. These all phenomena result in complex microstructures [1].

The use of the EBSD to characterize these complex microstructures has extended fast due to the remarkable development of the technique during last decade and the progressively more user friendly softwares to collect and analyze data. These advances make possible to scan extensive areas in a short time and provide both qualitative and quantitatively meaningful information. Many works have taken advantage of these facilities and they have reported detailed EBSD characterization of hot worked austenitic steels based on different methodologies [2-6]. However, any kind of extension of these methods, out of the experimental range reported in those works, becomes complicated, widely limiting their general applicability.

The main aim of this work is to explain those difficulties found in the characterization of the different substructural states in hot worked steels compared to cold worked substructures, and to provide some strategies that could avoid some unsolved problems in that respect.

2. EBSD microstructural characterization

After performing an EBSD scan on a determined area of the material, different microstructural features can be analyzed: on the one hand, the development of substructure inside grains by means of local-global ingrain misorientations

and/or changes in the image quality (IQ**)** of the Kikuchi patterns [7]. On the other hand, the scans allow analyzing the variation of the grain boundary character as a consequence of the thermomechanical processing. The latter point will be analyzed first.

2.1 Evolution of the grain boundary character

In austenitic stainless steels (ASS), the most prominent feature according to the grain boundary character distribution is the high amount of CSL boundaries. In particular, the amount of $\Sigma 3$ boundaries can represent a significant proportion of grain boundaries, being as large as 35-45% after conventional processing (not grain boundary engineered material) for various austenitic stainless steels [8,9]. The amount of $\Sigma 3$ boundaries has shown to be sensitive to the applied amount of strain under both monotonic and strain reversal conditions at high temperature [2,3], Figure 1.a, and in the strain hardening/dynamic recovery strain region, a correlation has been obtained as reported elsewhere [10] for hot worked 304 stainless steel. The $\Sigma 3$ fraction has been also observed to be roughly independent of the annealing conditions in fully statically recrystallized 304H austenitic stainless steel after cold working [8]. On the contrary, the results on dynamically recrystallized ASS [4] clearly show a decreasing tendency to form twin boundaries in the steady state as Z grows, Figure 1.b. An interesting work by Mandal et al. [5] have gone further and shown there is a linear relationship between the amount of $\Sigma 3$/coherent twin boundaries (in length), and the area fraction of dynamically recrystallized grains in a Ti-modified austenitic stainless steel, Figure 2.

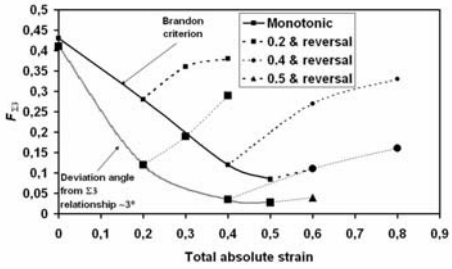

$$F_{\Sigma 3} = 0.43 - 0.66\varepsilon^{0.88} \quad (1)$$

a)

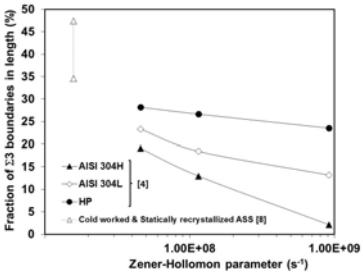

b)

Figure 1 Variation of $\Sigma 3$ boundaries fraction with strain [3,10] a), with Zener-Hollomon parameter Z in the steady state b) [4].

In case the SREX behaves as DREX with holding time, this type of procedure could provide an easy and fast way of determining the statically recrystallized fraction by simply measuring the fraction of Σ3. Nevertheless, more experimental work is required to back up this hypothesis.

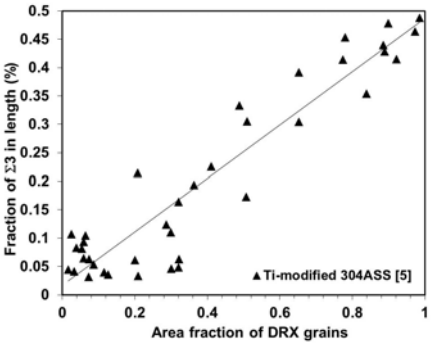

Figure 2 Change in the Σ3 with the area fraction of dynamically recrystallized (DRX) grains [5].

2.2. Ingrain EBSD parametrization

Several intragranular EBSD parameters have shown the capability of describing the micro/substructural evolution during cold/hot working processes. In this section, the potentialities and drawbacks of these parameters are briefly drawn when applied to hot worked steels.

IQ parameter

The IQ parameter is a metric describing the quality of the Kikuchi pattern [11]. This parameter has been largely used as a strain indicator [11] since it is sensitive to the density of defects in the region of analysis. However, this parameter is also affected by various variables such as: phase density, crystal structure, grain orientation, grain boundary location and/or experimental conditions (beam energy/spot size)/setup conventional SEM/FEG SEM [12].

The sensitivity of this parameter to the static recovery processes [13] and the measurability of the statically recrystallized fraction by means of a methodology based on the average IQ parameter [14] have been demonstrated in cold rolled materials, specifically, in ferritic steels. This success relies on several facts, namely, the amount of applied strain (large strains) and the ability of the material to develop a clear subgrain structure

during annealing as the result of the static recovery in some particular orientations (fibers).

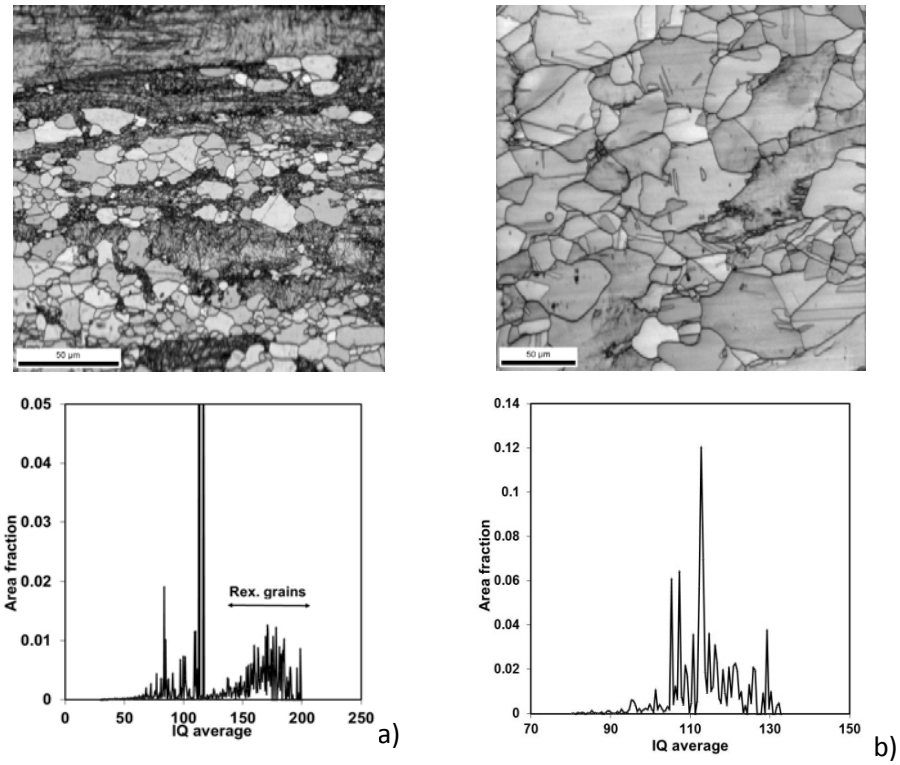

Figure 3 Image quality maps and normalized IQ distributions. a) Partially recrystallized cold worked ELC ferritic steel [15] and b) partially recrystallized hot worked TWIP steel [16].

In particular, the IQ based method detailed in [14] takes advantage of the existence of a bimodal distribution of grains accounting for whether the grain is recrystallized (high IQ values) or deformed (low IQ values), Figure 3.a. This method makes it feasible, after deconvoluting the IQ distribution, to determine the recrystallized fraction. Unfortunately, this is no longer valid for the most of the hot worked microstructures. For instance, the IQ distribution of partially recrystallized hot worked TWIP steel (ε=0.36 annealed at 1000ºC during 6.5s) cannot be described as a superposition of two distinctly different distributions, as can be seen in Figure 3.b.

Another point to be addressed is the effect of the grain size on the average IQ value. Indeed, this is a critical point at the earliest stages (nucleation) of the recrystallization or when fine grained materials are considered since new recrystallized grains or fine grains have low IQ average values due to the significant weight of points at grain boundaries. Hence, freshly nucleated grains or small grains and deformed grains can yield similar average IQ values, Figure 4.a. This handicap is partially overcome if FEG-SEM is used to perform the scans, because the beam conditions (spot size) specially vary the IQ values around grain boundaries, Figure 4.b.

Accordingly, the IQ based methods appears to be somewhat controversial due to the multiple affecting factors that cannot be avoided in hot worked (austenitic) microstructures. This results in a reduced applicability of the image quality as a micro/substructural characterizing parameter [7,17].

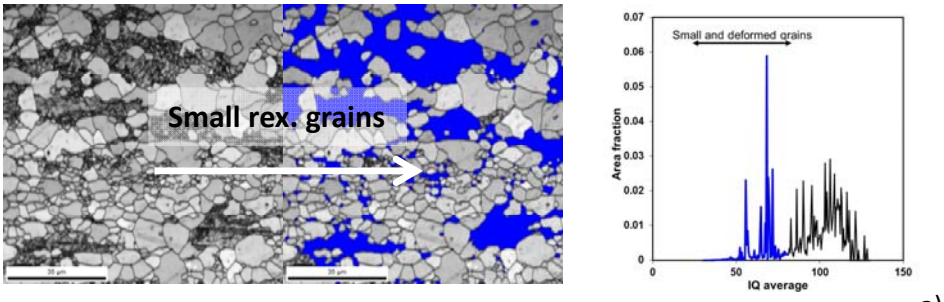

a)

FEG-SEM Conventional SEM b)

Figure 4 a) Small grains and IQ average distribution [15]. b) Effect of the SEM type on the width of low IQ values around (white segments) grain boundaries (20kV, step size 0.1µm). The width of the low IQ bands is delimited by the arrows.

Misorientation based parameters

Local misorientation parameters

The substructural development as a result of strain is observed to generate local curvature which manifests as local changes in orientation. These changes in local orientation have been usually characterized by means of the GAM (Grain Average Misorientation) or the kernel parameter defined as the average misorientation between any point and its surrounding points (1^{st} neighboring points: GAM and n^{th} neighboring points: kernel). Each grain has its own GAM value, whereas kernel parameter can be determined for each point or the whole grain (averaged).

These local parameters substantially change as the amount of strain varies in hot deformed austenitic stainless steels, even under strain path changes, if recrystallization phenomenon is hindered [3], Figure 5.a. Recrystallized grains are known to develop very low ingrain local misorientations. Therefore, low values of the GAM or kernel are expected for recrystallized grains [18]. Taking this observation into account, Mirzadeh et al. [6] have reported a noticeable correlation between average GAM parameter and DRX fraction, Figure 5.b.

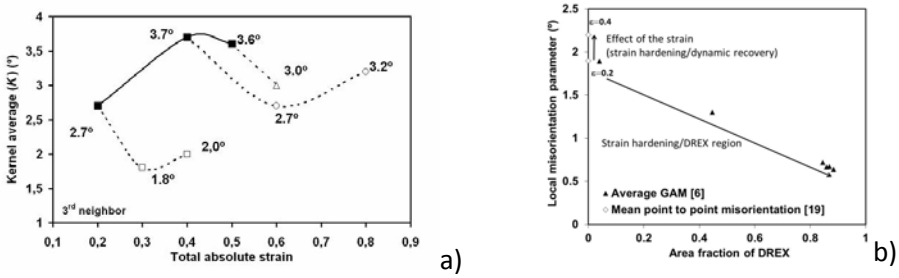

Figure 5 Evolution of a) the kernel parameter with strain path (bold (empty) symbols: monotonic strain (strain reversal)) [3] and b) the average GAM with the DRX fraction [6] and strain [19].

Nevertheless, when considering misorientations measured after processing Kikuchi patterns by Hough transform, the noise inherent to this method makes indiscernible low deformed grains from recrystallized grains. In fact, the noise in the measurement of the misorientation inside a strain free monocrystal has been stated to be at approximately 0.5º-1º [20]. This could be the case where low strains involve the onset of the static/dynamic recrystallization at very high annealing temperatures. One possibility to solve this problem is the application

of the High Resolution-EBSD by both cross correlation and pattern simulation methods [21,22]. This kind of EBSD methodologies gives rise to a higher degree of sensitivity to eventual local orientation changes. However, these procedures are currently time-consuming and they require powerful computers because each Kikuchi pattern of the scan needs to be recorded and post-processed in some detail.

Another drawback of the GAM or kernel parameters is their lower and upper threshold angle and step size dependence [7,23]. A new method proposed by Kamaya [24] appears to be a good solution to the step size dependence and to the low local misorientations developed under some thermomechanical processes. In that work, the local misorientation gradient G_L is defined as the slope of a local misorientation parameter, M_{ave}, measured for progressively smaller spatial distances. This parameter, G_L, is claimed to be independent of the step size and the accuracy of the orientation measurements. Further analysis of this method is required to assess its capability to characterize complex microstructure.

Global misorientation parameters

The global misorientation parameters as grain orientation spread (GOS) has been stated to be correlated with the amount of strain [2] and the optimum parameter to discern recrystallized from deformed grains [17] in hot worked low SFE metals. The development of long range misorientations inside the grains has been reported to increase monotonically as a consequence of the strain both for low and medium strains wherein no dynamic recrystallization occurs [3,25], Figure 6.

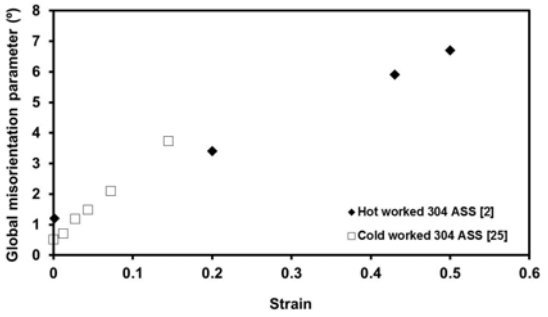

Figure 6 Evolution of different global misorientation parameters with the strain [2,25]

The main advantage of applying this parameter is its almost negligible dependence on the scan step size and the selected experimental options/environment [19, 25]. However, this parameter, as GAM or kernel do, needs a cut-off angle to distinguish recrystallized from deformed grains. The value of this threshold angle should be imposed to be above the actual angular resolution. Another source of concern in applying GOS parameter is the low ability of small grains to develop long range misorientations, even below noise threshold, and the dependence of these parameters in the grain size [25,26]. This last is shown in Figure 7.

Regarding the static recovery, good results have been reported for cold worked IF steels [27] when measuring misorientation evolution with annealing time in some fibers. Instead, the authors have not found any data that relate EBSD local-global misorientation parameters evolution with the static recovery after high temperature deformation. Due to the local character of the recovery processes, the global intragranular parameters do not seem a priori to be sensitive enough to those physical phenomena. Ongoing work is being performed at the present to evaluate the sensibility of local misorientation parameters to recovery at high temperatures in TWIP steels [16].

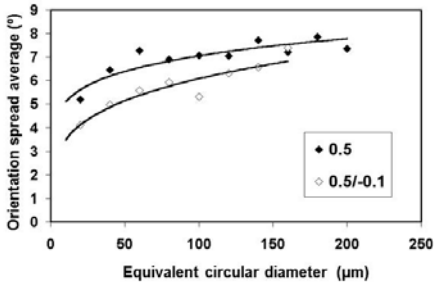

Figure 7 Variation of the orientation spread average parameter as a function of the grain sizes for two strain path [19].

3. Conclusions

Present work shows that there are many emerging tools and strategies to characterize via EBSD the complex microstructures involved in hot working processing. Up to date strategies have relied on a unique parameter to fully characterize the microstructural state. The analysis carried out seems to point out the necessity of more elaborated procedures. These procedures should combine several parameter/tools at the same time or in row to achieve a more

in detail characterization of the microstructure under study. Recrystallization nucleation and static recovery appears to need even more sophisticated strategies.

4. Bibliography

[1] H. J. McQueen, E. Evangelista Metall. Sci. Tech. 28-1 (2010) 12-21.

[2] D. Jorge-Badiola, A. Iza-Mendia, I. Gutiérrez Mat. Sci. Eng. A 394 (2005) 445-454.

[3] D. Jorge-Badiola, A. Iza-Mendia, I. Gutiérrez J. Microsc. 235 (2009) 36-49.

[4] M. El Wahabi, L. Gavard, J.M. Cabrera, J.M. Prado, F. Montheillet Mat. Sci. Eng. A 393 (2005) 83-90.

[5] S. Mandal, A.K. Bhaduri, V. Subramanya Sarma Metal. Mater. Trans. A 43 (2012) 2056-2068.

[6] H. Mirzadeh, J.M. Cabrera, A. Najafizadeh, P.R. Calvillo Mat. Sci. Eng. A 538 (2012) 236-245.

[7] S. Dziaszyk, E.J. Payton, F. Friedel, V. Marx, G. Eggeler Mat. Sci. Eng. A 527 (2010) 7854-7864.

[8] A. Yunquera Ph.D. thesis in course. TECNUN (University of Navarra).

[9] P.Lin, G. Palumbo, K.T. Aust Scr. Mater. 36 (1997) 1145-1149.

[10] D. Jorge-Badiola, J.L. Lanzagorta, I. Gutiérrez Metal. Mater. Trans. A 42 (2011) 2633-2642.

[11] S. I. Wright, M.M. Nowell Microsc. Microanal. 12 (2006) 72-84.

[12] S.D. Sitzman, G. Nolze, M.M. Nowell Microsc. Microanal. 16 (2010) 698-699.

[13] A. Martínez-de-Gerenu, F. Arizti, M. Díaz-Fuentes, I. Gutiérrez Acta Mater. 52 (2004) 3657-3664.

[14] J. Tarasiuk, P. Gerber, B. Bacroix Acta Mater. 50 (2002) 1467-177.

[15] M. Oyarzábal Ph.D. thesis (2007) TECNUN (University of Navarra)

[16] L. LLanos Ph.D. thesis in course. TECNUN (University of Navarra).

[17] S. Mitsche, P. Poelt, C. Sommitsch J. Microsc. 227 (2007) 267-274.

[18] G. Wu, D. Juul-Jensen Mater. Character. 59 (2008) 794-800.

[19] D. Jorge-Badiola Ph.D. thesis (2005) TECNUN (University of Navarra)

[20] A. J. Wilkinson Scr. Mater. 44 (2001) 2379-2385.

[21] A. J. Wilkinson, G. Meaden, D.J. Dingley Mat. Sci. Tech. 22 (2006) 1271-1278.

[22] J. Kacher, C. Landon, B.L. Adams, D. Fullwood Ultramicroscopy 109 (2009) 1148-1156.

[23] D. Jorge-Badiola, A. Iza-Mendia, I. Gutiérrez J. Microsc. 228 (2007) 373-383.

[24] M. Kamaya Ultramicroscopy 111 (2011) 1189-1199.

[25] M. Kamaya, A.J. Wilkinson, J.M. Titchmarsh J. Nuc. Eng. Dsg. 235 (2005) 713-725.

[26] N. Allain-Bonasso, F. Wagner, S. Berbenni, D.P. Field Mat. Sci. Eng. A 548 (2012) 56-63.

[27] R. Khatirkar, B. Vadavadagi, S.K. Shekhawat, A. Haldar, I. Samajdar ISIJ Int. 52 (2012) 884-893.

International Symposium on Plastic Deformation and Texture Analysis
Alcoy (Spain) 24-25 September 2012
187-197

Application of the EBSD in the study of stress induced martensitic transformation in shape memory alloys

García F. N.[1], Amigo V.[2], Cortés J.[1], Sánchez-Arévalo F. M.[3], González J. G.[3], Flores H.[4]

[1]Centro Tecnológico Aragón, FES Aragón, UNAM, México
[2]Universitat Politècnica de València, Instituto de Tecnología de Materiales
[3]Instituto de Investigaciones en Materiales, UNAM, México
[4]División de Materiales Avanzados, San Luis Potosí, México.

Abstract

EBSD measurements were conducted to study the stress induced martensitic transformation in a shape memory material. For this study two samples single crystal and polycrystalline of Cu-Al-Be were tested in tension. The crystal orientations of both samples were determined by EBSD technique. This work shows the remarkable contribution of EBDS to validate mathematical model for stress induced martensitic transformation. This idea suggested that it is possible to study the grain interaction in any shape memory material if the crystal orientation is known and a validated mathematical model is used.

Resumen

Se realizan mediciones difracción de electrones retrodispersados (EBSD) para estudiar la tensión inducida por la transformación martensítica en un material con memoria de forma. Para este estudio se ensayan a tracción dos muestras de monocristal y material policristalino de Cu-Al-Be. Las orientaciones cristalinas de ambas muestras se determinan mediante la técnica de EBSD. Este trabajo muestra la notable contribución de EBSD para validar el modelo matemático para la transformación martensítica inducida por tensión. Esta idea sugiere que es posible estudiar la interacción entre granos en cualquier material de memoria de forma si se conoce la orientación de los cristales y se utiliza un modelo matemático validado.

Keywords: Shape memory materials; EBSD; Stress induced martensitic transformation; grain interaction.

Palabras clave: Materiales con memoria de forma, EBSD, transformación martensítica inducida por tensión, interacción entre granos.

1. INTRODUCTION

The shape memory alloys (SMA´s) have been studied for many years since shape memory effects were found in Au-Cd in 1950[]. The main interest on SMA´s is due to their exotic behavior which ordinary metals and alloys don't exhibit. One of the main advantages of shape memory materials is that they present a potential for applications as "smart material" or also as new functional materials[]. The above mentioned alloys allows to develop more simple and better designs than conventional materials. In general the SMA´s present associated effects such as single shape memory effect and superelastic effect. This effects appear because of martensitic transformation existence. It can be indced for: Cooling, Stress , combination of both and magnetic field[]. Nowaday it have been made good advances in the study of SMA´s in spite of their mechanical behavior is Nonlinear, anisotropic, temperature dependent and hysteretic[]. Many studies have been published so far; they have worked in the development of models to mimic the complex thermomechanical behavior of shape memory materials [].

Recently it have been used the superelastic effect to study the mechanical behavior in different load arrangement relating the crystalline orientation with the growth of martensitic variants under stress [3].

For example in figure 1 the plane stress transformational diagrams for typical crystalline directions of the Cu-Al-Be beta phase is showed. In general these diagrams present different variants with the same possibility to appear in accordance with the current state of stress; however, in this case the simple tension and compression cases are shown. Here it is shown that several variants can appear because the Schmid Factor is equal for each variant; furthermore they have the same chance to grow up in the crystal. It is important to say that each variant present different mark on the observation.

It is clear that strong dependence with the orientation exists and the variants formed in the surface of the sample is strong dependently of the crystallographic orientation. For this reason is important known the crystallographic orientation in each sample study. However it is necessary a mathematical model with a relationship between martensitic variant formed and the crystallographic orientation.

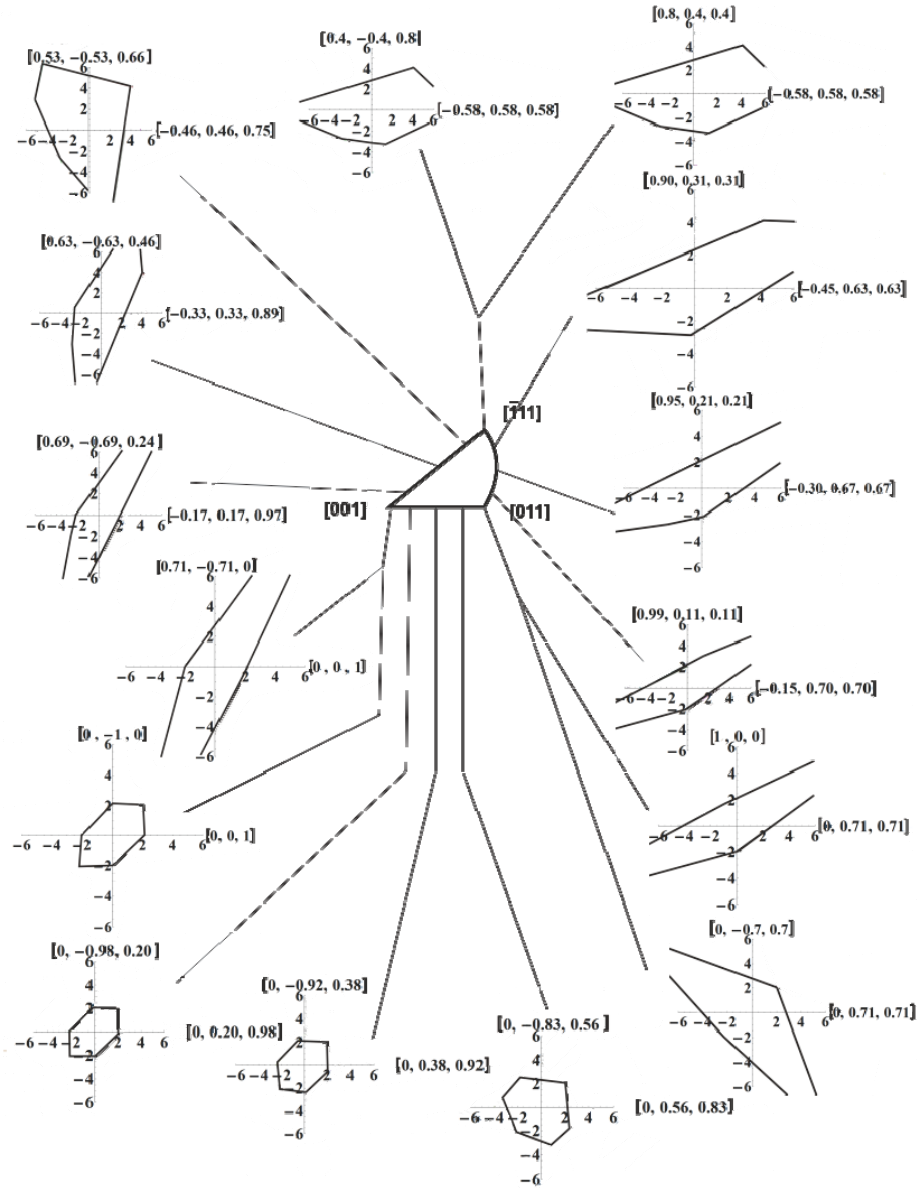

Figure 1. Plane stress transformational diagrams for typical crystalline directions of the Cu-Al-Be beta phase associated to different crystalline orientations represented in a stereographic projection.

In this way J. Cortes developed a mathematical model to simulate the stress induced martensitic transformation in single crystals[3]. The input data in this model are: crystallographic orientation, load arrangement, test temperature, transformational temperature, stress ratio and transformation system. And the output data are: stress transformation diagrams, martensitic variant identification, displacement field and pattern distortion on the sample surface. The equations 1 summarized this mathematical model as the transformation part (ε_{Tr}) of the Tensor strain field:

$$\varepsilon_{Tr} = \frac{1}{2}\left[grad\left(u\left(x_O, y_O, z_O\right)\right) + grad^T\left(u\left(x_O, y_O, z_O\right)\right)\right] \tag{1}$$

compound by a displacement field defined in a transformation basis, a kinetic function and a set of basis change rules. Displacement field in the transformation system $u\left(x_T, y_T, z_T\right)$ and their transformation to observation system $u\left(x_0, y_0, z_0\right)$:

$$u\left(x_T, y_T, z_T\right) = \begin{pmatrix} \delta fhw\left(y_T\right) \\ 0 \end{pmatrix} \tag{1a}$$

$$w\left(y_T\right) = \frac{fh + \sqrt{r_0^2 + {y_T}^2} - \sqrt{r_0^2 + \left(y_T - fh\right)^2}}{2\,fh} \tag{1b}$$

$$u\left(x_O, y_O, z_O\right) = A_{XT \to XO} u\left(x_T, y_T, z_T\right) \tag{1c}$$

$$\left(x_T, y_T, z_T\right)^T = A_{XO \to XT}\left(x_O, y_O, z_O\right)^T$$

Kinetic function (local volumetric fraction transformed) ($0 \le f \le 1$) :

$$f = \frac{e^{\frac{(\sigma - \sigma_0)}{\delta\sigma}}}{1 + e^{\frac{(\sigma - \sigma_0)}{\delta\sigma}}} \tag{1d}$$

Where:

$$\sigma_0 = \frac{\sigma_C + \sigma f}{2} \qquad \sigma_C = \frac{\partial \sigma_C}{\partial M_S}\left(T - M_S\right)$$

$$\sigma_f = \frac{\partial \sigma_C}{\partial M_S}\left(T - M_f\right) \qquad \delta\sigma = \frac{\sigma_f - \sigma_C}{2\ln(9)}$$

Transformation basis rules definition as function of crystalline orientation; Rolling plane/Rolling Direction (hkl)/[uvw] and transformation elements; Shear Direction/Habit Plane $[d1d_2d_3]/(p_1p_2p_3)$:

$$A_{XT\to X} = \sum_{i=1}^{3}\left\{e_{Ti}\right\}_X \otimes e_{Ti} = \begin{pmatrix} d_1 & p_1 & b_1 \\ d_2 & p_2 & b_2 \\ d_1 & p_3 & b_3 \end{pmatrix} \qquad A_{X\to XT} = \left[A_{XT\to X}\right]^{-1} = \sum_{i=1}^{3}\left\{e_i\right\}_{XT} \otimes e_i$$

$$A_{XO\to X} = \sum_{i=1}^{3}\left\{e_{Oi}\right\}_X \otimes e_{Oi} = \begin{pmatrix} u & c_1 & h \\ v & c_2 & k \\ w & c_3 & l \end{pmatrix} \qquad A_{X\to XO} = \left[A_{XO\to X}\right]^{-1} = \sum_{i=1}^{3}\left\{e_i\right\}_{XO} \otimes e_i$$

$$A_{XT\to XO} = A_{X\to XO}A_{XT\to X}$$

The main issue of our work is to prove that combining J. Cortés's mathematical model and EBDS measurements makes possible to study the grain interaction in SMA's. However it is clear that for this study, the crystal orientation in shape memory materials samples is required. An essential part of the recent works have been focused on microstructural-crystallographic measurements by advanced techniques[2]. One of the most advanced techniques to crystallographic measurements, in recent years, is the Electron Backscatter Diffraction (EBSD); It is allows us to measure crystal orientations easier and faster than others [].

2. EXPERIMENTAL DETAILS

2.1 Materials

Two kinds of samples of Cu-Al-Be shape memory alloy were used in this work; single and polycrystalline samples. The single crystal (M2) of Cu-Al-Be Shape Memory Alloy with transformation temperature near to -90°C. A polycrystalline sample (BB2) with composition near to Cu-12%Al-0.5%Be.

All the samples were betatized according to Flores et al. [].

2.2 Crystallographic orientation measurements

The crystallographic orientation measurements were done with EBSD technique using a scanning electron microspore JEOL model JSM 6300 with Electron Backscatter Diffraction figure 2.

Figure 2. SEM JSM-6300 with EBSD UPV.

The sample preparation was done without electropolishing in order to avoid multiple planes in the reduce central section of the tensile sample. The INCA software was used to analyze the obtained kikuchi patterns from EBDS measurements. The crystallographic parameters and crystalline structure were programmed in the software because the Cu-Al-Be did not exist in the data base.

2.3. Tension test

Single tension tests were carried out in a typical tension device with constant a strain rate equal to 0.2 mm/min. The equipment has a load cell of 2 kN and it was possible to mount the tensile device under the optical microscope (LEICA MZ APO). The OM was connected with a PC to register videos or images of the sample surface undergoing stress induced martensitic transformation Figure 3.

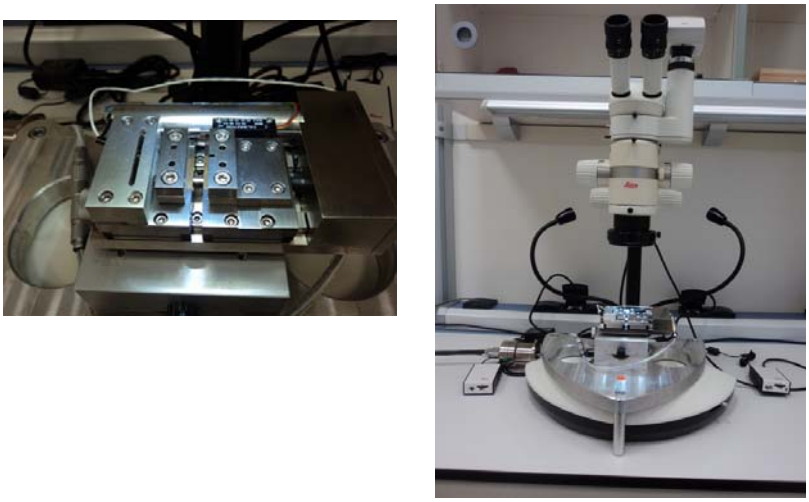

Figure 3. Tensile device Deben-Gatan microtest UPV.

3. RESULTS AND DISCUSSION

3.1. Mathematical model validation

First by simplify the Cortés' model was applied to our single crystal sample M2. The Figure 7a shows the micrograph corresponding to the single crystal M1 subjected to simple tension. Here we can observe the bright lines associated to the growth of martensitic variant in the material due to the applied load. The Figure 7b shows the martensitic variant with the highest Schimd factor, this variant was identified as V23. The calculated martensitic variant was superimposed to Figure 7a; it is clear that the theoretical calculation, done with the Cortes´s mathematical model, was in good agreement with the experimental results showed in Figure 4. This result validates Cortes´s mathematical model.

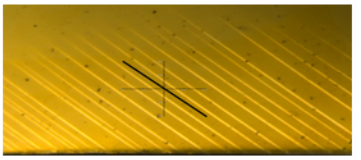

Variant	23
F.S	0.49

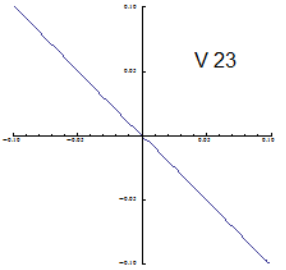

RD = <0.97 -0.03 -0.22>

SN = {0.22 -0.05 0.97}

a) b)

Figure 4. Mechanical behavior presented by Single crystal M1 and the theoretichal calculation. a) Micrographic of Stress induced martensitic transfomation b) Variant calculated with maximun schmid factor.

3.2. Polycristal

The crystalline orientations in of several grains were measure by EBSD technique in polycrystalline sample. In Figure 5 it is presented only a region of the polycrystalline sample.

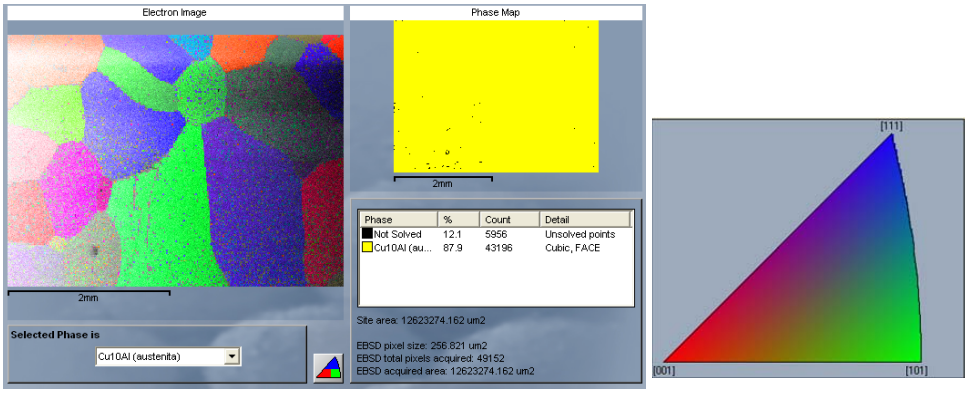

a) b)

Figure 5. a) One region analyzed with INCA software b) Key Colors.

3.3. Stress induced martensitic transformation in polycrystalline sample

The martensitic transformation in triple point in sample polycrystalline is showed in figure 6. The angle of each martensitic variant formed is showed too.

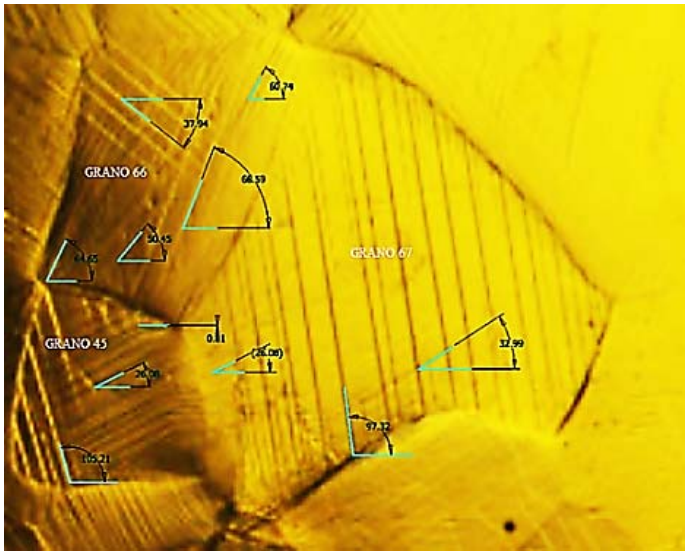

Figure 6. Graphics and micrographic of grain interaction in triple point in sample polycrystalline.

Contrary to the previous case (single crystal) in this case there are several variant formed in each grain. However in each grain only 24 variant can be formed. Used the Corte´s Model it is possible obtain these possible martensitic variants in the observation system. In figure 7 the 24 variants for one grain are showed.

These variants can be superimposed in each grain and to compare them with the formed variants. This allows to select the coincident variants and to discuss the reason of their appearance.

Additionally the plane stress transformational diagrams can be obtained. In figure 8 the plane stress transformation diagram for one grain is showed.

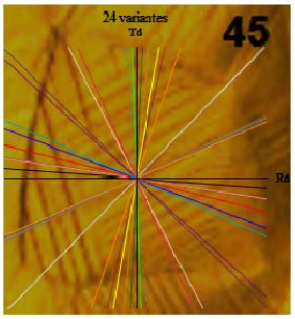

Variant	1	2	3	4	5	6	7	8	9	10	11	12
Color												

Variant	13	14	15	16	17	18	19	20	21	22	23	24
Color												

Figure 7. The 24 martensitic variants superimposed in grain 45.

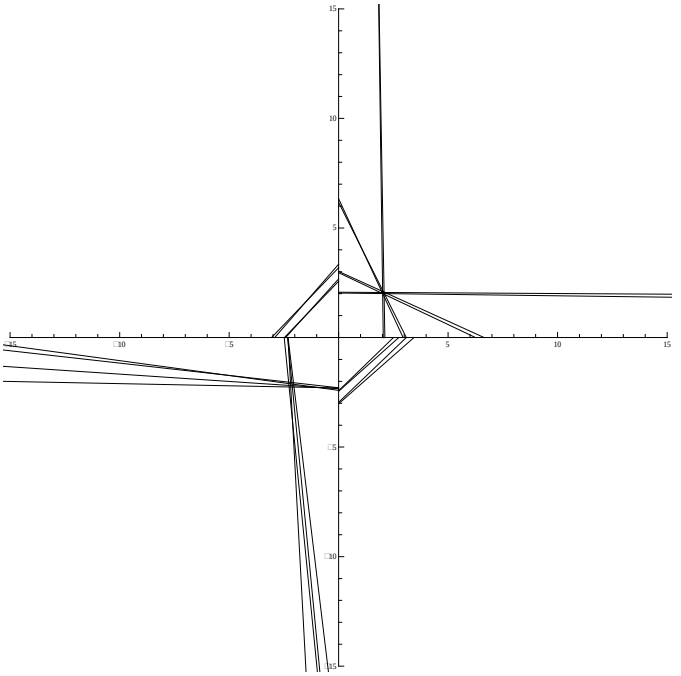

Figure 8. Plane stress transformation diagram for one grain.

It is important because this diagram is unique for each martensitic variant formed. With these diagrams it is possible to know the state of stress in each case.

Considering that in a single crystal was formed a single variant (V23), it seems logical to consider that the growth of more than one variant in a grain becomes in evidence of a grain interaction.

It is clear that a similar study can be made grain to grain in the sample and even with the methodology mentioned in this work and Cortes's Model the interactions will be quantified. However this methodology is not possible to apply it if the crystalline orientation is ignored. For this reason the EBSD is very important in this study.

4. CONCLUSION

Therefore, our conclusions are:

The Cortes's model was validated because the comparison with experimental result in a single crystal present good agreement in uniaxial tensile.

With a low cost an analysis of several grains can be used for certain estimation of the mechanical behavior because the velocity EBSD is faster than before.

The methodology present suggested that is possible study the grain interaction in any shape memory materials if the crystal orientation is known and it is used the mathematical model validated.

It is recommended to make a deep study with reported results and other shape memory alloys.

5. REFERENCES

[1] Sammis, C.G. y Ashby, M.F., *Acta Metall*., 34, 511-526 (1986).

[2] Landres, J.D., "The role of fracture mechanics in the study of fracture mechanisms", en Fracture: Interactions of Microstructure, Mechanisms and Mechanics (Ed. Wells, J. M. Y Landres, J. D.) pp. 1-28, The Metallurgical Society of AIME, Warrendale, Pennsylvania.

[3] Smith, J.L. and Jones, B.M., *Advances in Formatting*, 14:3 23-26 (1999).

6. ACKNOWLEDGEMENTS

The authors would like to thank the program PAPIIT-UNAM project: IN111310 and UPV for the financial support of this study. We are grateful to Manuel Josep Planes Insausti and and José Luis as well as all personal of microscopy laboratory of UPV for their technical support. Finally thank to Rodrigo Lechuga Taboada and Miguel Angel Romero Barrientos for the support in this work.

International Symposium on Plastic Deformation and Texture Analysis
Alcoy (Spain) September 24th and 25th
199-209

The structural state of severely deformed materials analysed with a transmission electron microscope

E.R. Rauch, M. Véron

Science et Ingénierie des Matériaux et des Procédés, Université de Grenoble/CNRS, Grenoble INP–UJF, 38402 Saint-Martin d'Hères, France

Abstract

The grain and cell structure of severely deformed materials are hard to characterize even when observed with a transmission electron microscope (TEM). In particular, the bright field images are misleading. Consequently, measuring grain or cell size in view of modelling their effect on the plastic behaviour is not straightforward. An experimental approach that permits the structural evolution of severely deformed materials to be inferred is proposed. Misorientations are measured with a dedicated TEM tool that automatically analyses the electron diffraction patterns.

Resumen

La estructura de los granos y celdas de materiales severamente deformados son difíciles de caracterizar, incluso cuando se observa con un microscopio electrónico de transmisión (TEM). En particular, las imágenes de campo claro son engañosas. Por consiguiente, la medición del tamaño de los granos o de las celdillas, en vista de modelar su efecto sobre el comportamiento plástico, no es sencilla. Se porpone un enfoque experimental que permite obtener la evolución estructural de materiales severamente deformados. Las desorientaciones se miden con una herramienta en el microscopio electrónico retransmisión que analiza automáticamente los patrones de difracción de electrones que se obtienen.

Keywords: Severe Plastic Deformation, Orientation maps, TEM, diffraction patterns, Grain size

Palabras clave: Deformación plástica severa, mapas deorientación, TEM, patrones de difracción, tamaño de grano.

1. Introduction

Severe plastic deformations are known to modify drastically the mechanical properties of metals. The benefits either at medium to high temperatures (superplasticity) or at room temperature (improved yield stress) are well established and are usually interpreted as the direct effect of grain refinement through respectively enhanced grain boundary sliding or Hall-Petch effect [1]. Dedicated processes like Equal Channel Angular Extrusion or High Pressure Torsion tests [2] are now commonly used to promote intragranular misorientations that in turn are expected to lead to the grain refinement. The final grain size is an essential parameter for these materials. However, for severely deformed alloys, measuring this quantity is not a straightforward task. Indeed, optical microscopy has not the adequate spatial resolution and electron microscopes suffer from specific limitations. In particular, the efficiency of Electron Back-Scattered Diffraction attachments (EBSD) on Scanning Electron Microscopes is known to decline with increasing strain. The relationship between increasing plastic deformation and decreasing pattern (or image) quality (IQ) measured with EBSD attachments has been considered in the past [3] to quantify strain using the values of IQ.

Besides, as will be stressed below, the contrast in bright field images obtained with transmission electron microscopes (TEM) is too complex to enable a proper identification of grain boundaries. Consequently, the above mentioned mechanical consequences of grain refinement are frequently discussed with rather imprecise data and poor descriptions of the structural state. This leads to some difficulties in terms of process optimization and modelling efforts.

The objective of the present work is to describe an experimental approach that gives a better insight in the structural state of severely deformed materials. A dedicated TEM tool was developed to measure misorientations in deformed metallic samples. This TEM attachment is described in section 2. In section 3, the limitations and errors related to the usage of direct bright field observations for severely deformed metals are illustrated with the help of the mentioned tool.

2. Automated Crystallographic Orientation Mapping with a Transmission Electron Microscope (ACOM/TEM)

The tool that was developed for the present purpose may be considered as an EBSD type accessory adapted to TEMs [4]. In both approaches the electron beam is scanned over the area of interest with a given step size and thousands of electron diffraction patterns are recorded and analysed with appropriate software. The main difference, apart from the use of a transmission instead of a reflection microscope, stands in the fact that spot patterns (i.e.: Bragg diffraction peaks) are preferred to Kikuchi lines to derive the local orientation from the TEM diffraction patterns. Indeed, the positions of Kikuchi (or pseudo-Kikuchi) lines are very sensitive to the crystal orientation and consequently if the irradiated volume contains small misorientations, the lines are smoothed out and hard to extract from the background noise. This is why EBSD tools indexing capability declines with increasing strain. In the contrary, it is the intensity of the spots rather than their location that is modified by small orientation changes, so that despite the distortions related to dislocations existing in the volume crossed by the electron beam, the Bragg peaks remain well defined and easy to recognize.

A further particularity of the present tool is that the spot patterns are identify with image correlation techniques. This means that, firstly, the spot patterns for every set of Euler's angles within the ranges limited by the crystal symmetry are calculated with devoted software and stored in a database. Then, all the theoretical patterns are compared to the acquired one through template matching and the closest one is selected. The Euler's angles being known for the template, the orientation of the crystal is deduced. The angular resolution is related to the angular step used to generate the database. Further details on the technique are given elsewhere [4,5]. The important point for the present work is that the procedure is efficient even if the crystal contains a very large dislocation density. Moreover, in case of superimposed patterns, as at grain boundaries, the identification procedure is able to extract the dominant one.

The indexing capability of the tool is further improved using electron precession [6]. The resulting package, known as ASTAR [7], may be adapted to nearly all transmission electron microscopes. A typical orientation map obtained with the tool is given in figure 1. It concerns a deformed copper sample. Grain and twin boundaries are easily recognized thanks to the

orientation related code colour. The process delivers additional information like identification reliability (Fig1.b) and the matching index (Fig 1.c). Note that structural details are nicely highlighted on all of these maps. In particular, the indexing reliability (Fig. 1.b), whose value decreases if more than one crystal orientations are extracted from the diffraction pattern, gives a picture of the structure that turns out to be for far better than the usual bright field image. This fact is explained in the following section.

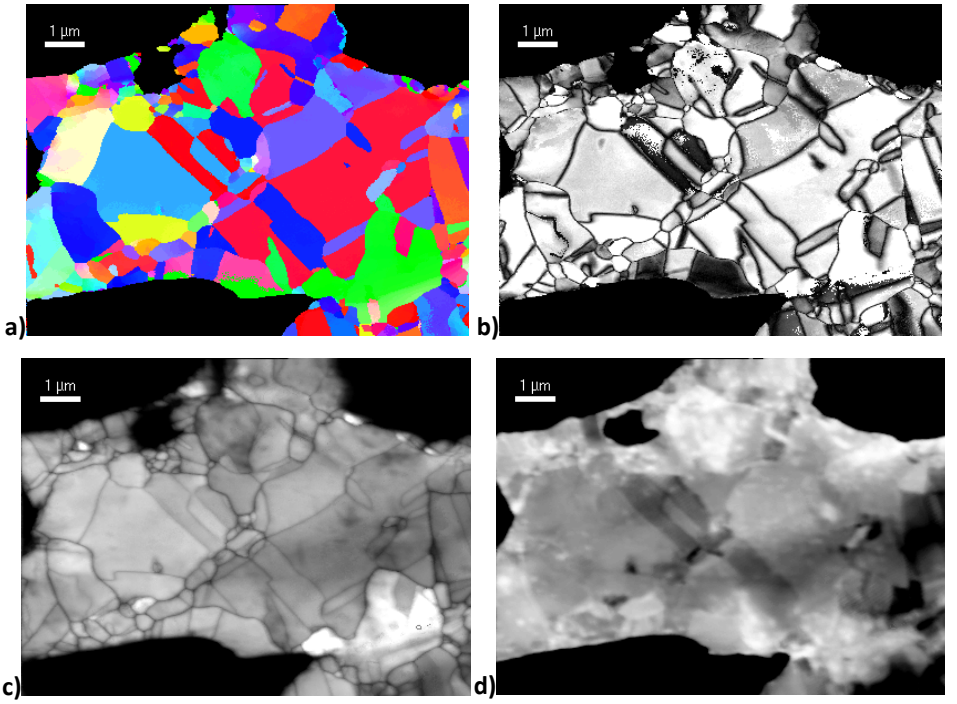

Figure 1. Deformed copper characterised with ASTAR. Crystal orientation (a) is identified through template matching. The process provides simultaneously (b) reliabilities, (c) matching indexes values, as well as (d) a virtual bright field image.

3. The limitation of bright field images for deformed materials

Bright field images are standard results extracted from TEM observations. They are easy to obtain and appropriate to highlight structural details such as staking fault, individual dislocation, twins etc. The image contrast turns out to be very sensitive to fine details. The question arises if such a sensitivity is still adapted when the densities of the observed features is very high. The two

following examples illustrate the limitations of TEM observations in bright field mode

3.1. Bright field contrast and misorientations related to a cell structure

The information contained in bright field images may be directly compared to the orientation maps obtained with the dedicated TEM attachment.

The example shown in figure 2 concerns a regular cell structural state related to austenitic 304 L steel cyclically deformed at 300°C. The sample was cycled to rupture (N=12100) with a total fatigue strain amplitude per cycle of 0.5%. The bright field image (Fig 2.a) reveals a well-developed cell substructure with boundaries that contain most of the dislocations. The 8.8 x 8.2 µm² area was scanned by steps of 28 nm and belongs entirely to a unique grain whose normal orientation is close to [203]. The colour contrast in the orientation map (Fig. 2.b) is enhance by scaling the red, green and blue intensities with three directions (respectively: [102], [506], [516]) that delimit a reduced range of orientations. Figure 2.c is a so-called virtual bright field image obtained by selecting the transmitted beam of each collected diffraction pattern with a virtual aperture and plotting its intensity fluctuation while the area is scanned (see [8] for details). This procedure permits the scanned area to be recognized unambiguously while the TEM was operating in diffraction mode (i.e.: in a blind mode).

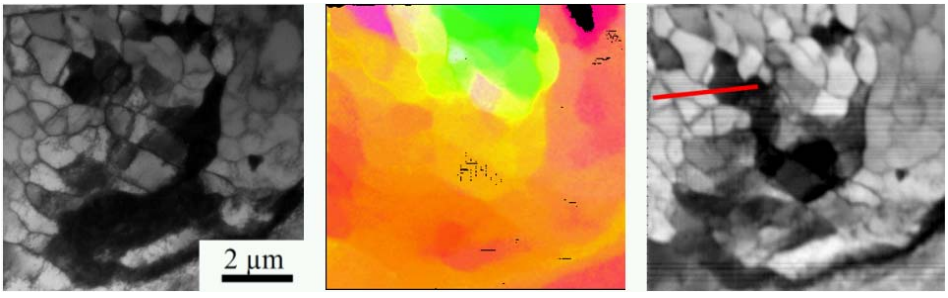

a) b) c)

Figure 2. TEM characterisation of a 304L steel cyclically deformed at 300°C, a) bright field micrograph, b) orientation map and c) virtual bright field image.

The most striking feature appearing in the micrograph is the black and white contrast which reveals misorientations from one cell to the other. The misorientations related to the short line drawn in figure 1.c are computed from the Euler's angles and plotted in Fig. 3. They are calculated with respect to a

reference point taken in the middle of the second cell crossed by the line and used as the origin for the position in Fig. 3. Besides, the intensity level (i.e.: the contrast) is extracted from the virtual bright field image for every pixel and added in figure 3 that, consequently, depicts the relationship between misorientation and contrast. The line is crossing four cells, the two first being bright while the two last have low intensities. Essentially it may be noticed that there is no definite correlation between brightness changes and misorientation. In particular the two first cells exhibit a 3° misorientation for nearly the same brightness. This is not surprising and will appear, for example, when two cells differ by a rotation around the normal axis. The point that it is wished to be emphasized by this example is that black to white contrast appears for very small orientation changes: the intensity is decreasing drastically between the second (white) and the third (black) cells that are only one degree apart. It is this high sensitivity that makes TEM images so useful for viewing features like dislocations, irradiation damages or strain fields around coherent precipitates. It will be stressed below that for heavily deformed metals it is a disadvantage. The present results remind us that a bright field image alone does not enable the misorientations between cells to be estimated, even roughly. Besides, it is worth mentioning that the angular resolution of the ACOM/TEM attachment may be directly deduced from the fluctuation of the estimated misorientation within a given cell in Fig. 2 and turns out to be of the order of 0.2°.

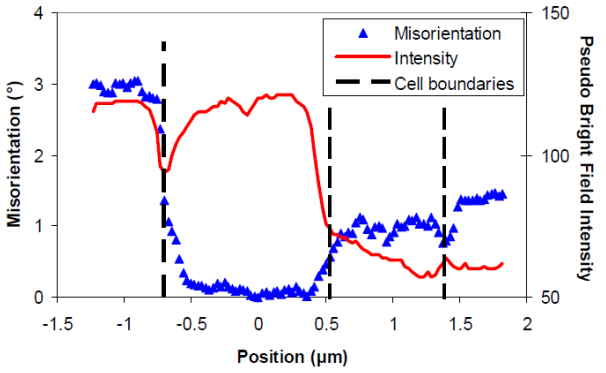

Figure 3. The virtual bright field intensity and misorientations calculated with respect to the point set at the origin of the abscissa for the lines drawn in Fig. 2.c.

3.2. Grain sizes in severely deformed metals

Some examples of the complex contrasts related to very large strains are shown in figure 4. The micrographs concern 7075 aluminium alloys subjected to three, six or eight extrusions through an ECAE die. The channels form a 90° angle so that the equivalent strain increases by an amount of 1.15 at each path. The two first TEM pictures appear similar with nearly equiaxed black areas whose size may reach 1 µm. The last example exhibits apparently a much finer structure. The orientation maps, that cover 4.2 x 4.5 µm² areas in all cases, show an entirely different trend (Fig. 5). In these maps, the standard code color used to define the normal direction is used, i.e.: red for [001], green for [101] and blue for [111]. Except for the grain shape and orientation, the maps are comparable for the two largest strains (Fig. 5.b and 5.c) while the structure obtained for the lowest strain (Fig. 5.a) is substantially dissimilar.

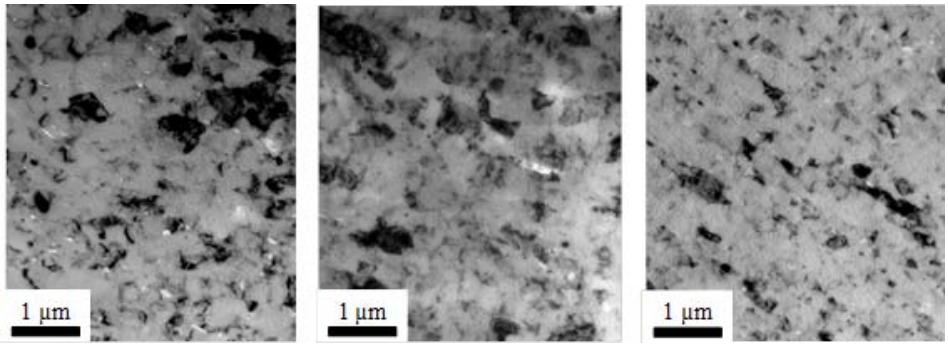

a) b) c)

Figure 4. Bright field images of a) an AA7075 extruded 3 times at 130°C, a) a Zr and Sc added AA7075 extruded 6 times at 120°C, a) an AA7075 extruded 8 times at 130°C.

Indeed, with grain boundaries being defined as locations where misorientations are higher than a threshold value (15° for the lines highlighted on the figures), around 80 grains may be identify in Fig. 4.b as well as in Fig. 4.c while there are only few of them in Fig. 4.a, with one covering alone 70% of the total area. An estimate of the grain sizes with these boundaries through the intercept method, would give around 0.4 µm for both 6 and 8 extrusions. By contrast, a proper estimate cannot be obtained for the less strained sample because most of the grains are not completely contained in the map. This means that grains sizes may differ by an order of magnitude while the micrographs would remain similar (e.g.: Fig. 4.a and Fig. 4.b) and, conversely,

the same grain size may be related to quite different structural aspects as in Fig. 4.b and 4.c.

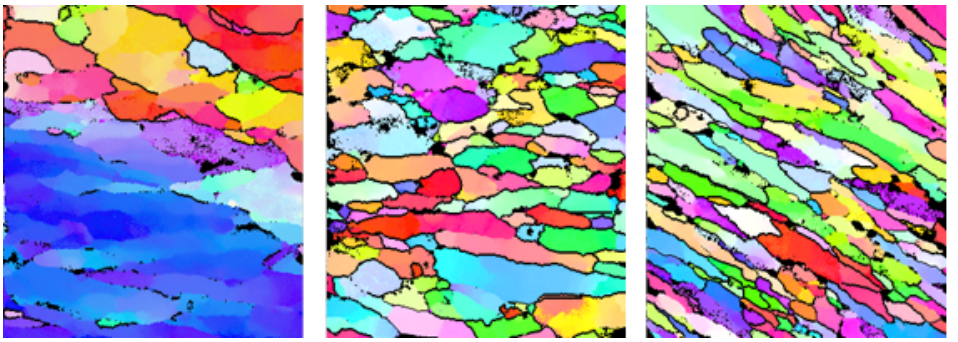

a) b) c)

Figure 5. Orientation maps corresponding to Fig 4.a to 4.c. Mis-indexed pixels as well as location where misorientations exceed 15° appear in black.

This absence of correlation is the result of the strong contrast sensitivity to the Bragg diffracting conditions that was discussed in the previous section. In fact, the TEM bright field technique is too sensitive for imaging structures that contains numerous sources of distorsions like dislocations, boundaries or merely internal stresses. Therefore, bright field images alone do not allow a proper analysis of severely deformed materials and in particular of their grain size.

4. Grains sizes deduced from orientation maps

The colour gradients appearing on maps related to severely deformed materials reveal the disturbed nature of the crystal. The misorientations are far from being confined to grain boundaries and are distributed all over the area. Such deformation state is better characterized with the help of the misorientation distribution function $F(\theta)$. The latter corresponds to the number of times a given misorientation angle is detected on the map. The misorientation distributions related to figure 5.a and 5.b. are plotted in figure 6.

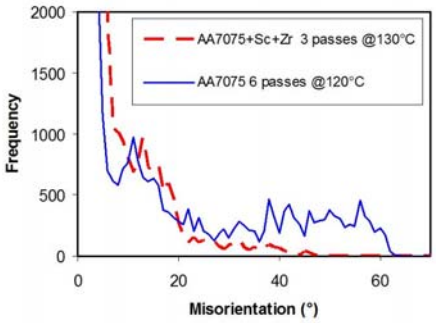

Figure 6. The misorientation angle distribution F(θ) calculated with the data extracted from Fig. 5.a and 5.b. Note that these are absolute, not relative values.

The two states differ essentially from a quantitatively point of view: the tail of the frequency curve extends over larger misorientations when the strain level is increased. The grain refinement related to severe plastic deformation is contained in the tail extension. Indeed, the grain size D may be obtained by summing the number of pixels related to misorientations higher than the grain boundary threshold value through:

$$\frac{1}{D} = \frac{1}{2\mathrm{N}.\Delta \mathrm{x}} \sum_{\theta=15}^{63} \mathrm{F}(\theta) \qquad (1)$$

with F(θ) being the misorientation angle distribution calculated over the whole map in both x and y directions, N is the total number of pixels and Δx the step size. The equation is nothing else than the intercept method applied to every horizontal and vertical lines of the orientation map. Equation (1) leads to estimates of grain sizes that equal 0.5 µm for figure 5.b (and figure 5.c) and 4 µm for figure 5.a. As mention previously the last value underestimates the real grain size because most of the grains are not entirely included in the map.

The distribution F(θ) is frequently used to characterize severely deformed metals. Indeed, it is common to split the distribution into low angle grain boundaries (LAGB) and high angle grain boundaries (HAGB) and to compute data related to each group (e.g.: [7,8]). However, it is clear that considering uniquely the grain and cell sizes for severely deformed materials appears as a drastic reduction of the information contained in the orientation map and cannot suffice to describe this kind of structural state. Indeed, it is worth mentioning that the grains are ill-defined, i.e.: frequently their boundaries do not close up. Consequently, there are numerous couple of adjacent points that have grain boundary type misorientations (> 15°) but that may be continuously

connected through paths that never cross a grain boundary. This leads to the discontinuities that are observed for the grain boundaries highlighted in the orientation maps (e.g.: Fig. 5a). Consequently, a 'grain' may extend over significant areas and contains numerous fragments of boundaries. This means that even when cell and grain boundaries may be separated, like with the present tool, it is still not evident to compute a grain size. More precisely, the size will depend on how the grain is defined and computed: for a non-closed grain, the intercept method leads to a far smaller value than, for example, the square root of the 'grain' area.

From the preceding remarks, it appears that the structural state of severely deformed materials is peculiar and the related mechanical properties may hardly be interpreted by merely extrapolating to smaller grain sizes the constitutive laws used for standard materials. In particular, none of the classical interpretations of the Hall-Petch law is expected to work without adaptation in the present case.

5. Bibliography

[1] R.Z. Valiev, T.G. Langdon, Prog. Mater. Sci. 51 (2006) 881–981

[2] R.Z. Valiev, R.K. Islamgaliev, I.V. Alexandrov, Prog. Mater. Sci. 45 (2000) 103–189

[3] E.M. Lehockey, Y. Lin and O.E. Lepik,. In: A.J. Schwarts et al., Editors, Electron Backscatter Diffraction in Materials Science, Kluwer Academic/Plenum Publishers (2000), pp. 247–264.

[4] E. F. Rauch, L. Dupuy, Arch. Metall. Mater. 50 (2005) 87–99.

[5] E. F. Rauch, A. Duft, Mater. Sci. Forum, 495–497 (2005) 197–202.

[6] E. F. Rauch, J. Portillo, S. Nicolopoulos, D. Bultreys, S. Rouvimov, P.Moeck Zeitschrift für Kristallographie: (2010) Vol. 225, pp. 103-109

[7] www.nanomegas.com, NanoMEGAS-CNRS Patent pending technique.

[8] E. F. Rauch, M. Veron, J. Mater. Sci. Eng. Tech. 36 (2005) 552–556.

[9] A. Gholinia, F. J. Humphreys, P.B. Prangnell, Acta Mater. 50 (2002) 4461–4476

[10] P.B. Prangnell, J.R. Bowen, A. Gholinia. In: Dinesen AR, et al., editors. Proceedings of the 22nd Riso International Symposium on Materials

Science, Science of Metastable and Nanocrystalline Alloys, Roskilde, Denmark, September; 2001. p. 105.

6. Acknowledgements

The financial support of the Materials and Processing Techniques Division of the French Ministry of Research (RNMP) through the Ultrafine Grained Steels Project (AGUF) is gratefully acknowledged. Parts of the illustrations used in the present paper were extracted from additional collaborative works. Are acknowledged Prof. N. Llorca-Isern from the University of Barcelona (Fig. 1), A. Garcia and L. Legras (EDF R&D - Renardière, Moret sur Loing France: Fig. 2.a), J.M. García-Infanta and Prof. F. Carreño (National Center of Metallurgical Research CENIM - Madrid, Spain: Figs. 4.a and 4.c) as well as K. Turba (Charles University - Prague, Czech Republic: Fig. 4.b).

Authors and Contributors

INTERNATIONAL SYMPOSIUM ON PLASTIC DEFORMATION AND TEXTURE ANALYSIS

Editor:
Vicente Amigó, Institute of Materials Technology, Universitat Politècnica de València

This book contains the communications presented at the symposium, which we divide into two parts. The first one dedicated to plastic deformation of metallic and ceramic materials. The second one focused on texture analysis.

This second part is mainly intended to recent research in Electron Diffraction Backscatered (EBSD) and some of its applications. Finally other related developments in the field of X-ray diffraction are discussed.

All this with the help of leading researchers in the field, who display in sequence the latest developments and applications in texture analysis.

Este libro recoge las presentaciones realizadas en el simposio, que dividimos en dos partes. Una primera dedicada a la deformación plástica de los materiales, metálicos y cerámicos. La segunda dedicada al análisis de las texturas.

Esta segunda parte se destina principalmente a las recientes investigaciones en Electron Backscatered Diffraction (EBSD) y algunas de sus aplicaciones. Finalmente se analiza otros desarrollos en el campo de la difracción.

Todo ello mediante el concurso de importantes investigadores en el campo que presentan de forma ordenada los últimos avances y aplicaciones en el análisis de texturas.